UC San Diego
UC San Diego Electronic Theses and Dissertations

Title
Instabilities, Turbulence and Mixing from Internal Waves at bottom topography

Permalink
https://escholarship.org/uc/item/8937h9x6

Author
Chalamalla, Vamsi Krishna

Publication Date
2015

Peer reviewed|Thesis/dissertation

eScholarship.org Powered by the California Digital Library
University of California

UNIVERSITY OF CALIFORNIA, SAN DIEGO

Instabilities, Turbulence and Mixing from Internal Waves at bottom topography

A dissertation submitted in partial satisfaction of the
requirements for the degree
Doctor of Philosophy

in

Engineering Sciences (Mechanical Engineering)

by

Vamsi Krishna Chalamalla

Committee in charge:

Professor Sutanu Sarkar, Chair
Professor Jennifer MacKinnon
Professor Eugene R. Pawlak
Professor Antonio L. Sanchez
Professor William R. Young

2015

Copyright
Vamsi Krishna Chalamalla, 2015
All rights reserved.

The dissertation of Vamsi Krishna Chalamalla is approved, and it is acceptable in quality and form for publication on microfilm and electronically:

Chair

University of California, San Diego

2015

DEDICATION

To my brother Anup

TABLE OF CONTENTS

Signature Page iii

Dedication iv

Table of Contents v

List of Symbols vii

List of Figures viii

List of Tables xii

Acknowledgements xiv

Vita xv

Abstract of the Dissertation xvi

Chapter 1 **Introduction** 1
- 1.1 Internal Waves 1
- 1.2 Mixing due to breaking internal waves 3

Chapter 2 **Turbulence during internal wave reflection on critical and near-critical slopes** 7
- 2.1 Introduction 7
- 2.2 Formulation of the problem 10
  - 2.2.1 Governing equations 10
  - 2.2.2 Wave forcing 13
  - 2.2.3 Boundary conditions 14
  - 2.2.4 Numerical method 14
  - 2.2.5 Turbulence diagnostics 17
- 2.3 Laminar regime 17
  - 2.3.1 Velocity field 18
  - 2.3.2 Frequency spectra 19
- 2.4 Turbulent regime 21
  - 2.4.1 Development of turbulence in near-critical cases 21
  - 2.4.2 Comparison of turbulence between critical and near-critical cases 25
- 2.5 Mean Kinetic Energy 30
- 2.6 Parametric dependence of turbulence statistics 32
- 2.7 Conclusions 35
- 2.8 Acknowledgements 38

Chapter 3 **PSI in the case of internal wave reflected from an uniform slope** . . . 39
3.1 Introduction . . . 39
3.2 Formulation of the problem . . . 43
3.3 Results . . . 48
3.3.1 Evolution of subharmonic waves . . . 49
3.4 Energetics . . . 59
3.5 Discussion and conclusions . . . 63
3.6 Appendix: Calculation of theoretical growth rates . . . 66
3.7 Acknowledgements . . . 68

Chapter 4 **Mixing, dissipation rate, and their overturn-based estimates in a near-bottom turbulent flow driven by internal tides.** . . . 69
4.1 Introduction . . . 69
4.2 Formulation . . . 73
4.2.1 Governing equations . . . 76
4.2.2 Boundary conditions . . . 77
4.2.3 Numerical method . . . 77
4.2.4 Turbulence diagnostics . . . 78
4.3 Turbulence Budgets . . . 79
4.4 Available Potential Energy . . . 84
4.5 Thorpe Scales . . . 90
4.5.1 Evolution of Thorpe length scales . . . 91
4.5.2 Turbulent dissipation rate inferred from Thorpe scales . . . 94
4.6 Mixing Efficiency . . . 100
4.7 Diffusivity . . . 101
4.8 Conclusions . . . 102
4.9 Acknowledgements . . . 105

Chapter 5 **Multi-scale modeling of internal tide generation** . . . 106
5.1 Introduction . . . 106
5.2 SOMAR-LES . . . 106
5.2.1 One-way Coupled Model . . . 108
5.3 Tidal flow past model Kaena ridge . . . 110
5.4 Acknowledgements . . . 119

Chapter 6 **Summary and Future Work** . . . 120

Appendix A **SOMAR Algorithm** . . . 127

References . . . 130

LIST OF SYMBOLS

$\mathbf{u}$	Velocity in cartesian coordinate system
U_0, U_∞	Free stream velocity
u_τ	Friction velocity
τ_w	Wall shear stress
ρ	Total density
ρ^*	Deviation of from the background density
ρ^b	Background density
ρ_0	Reference density
ν	Molecular viscosity
κ	Thermal diffusivity
β	Slope angle
θ	Potential temperature
Ri_g	Gradient Richardson number
B	Buoyancy number
Re_S	Reynolds number
Re	Stokes Reynolds number
Ex	Excursion number
γ	Steepness parameter
δ_S	Stokes layer thickness
Fr	Froude number
Pr	Prandtl number
$\langle \cdot \rangle$	Reynolds average
$\overline{(\cdot)}$	Filtered quantity
g	Acceleration due to gravity
Ω	Wave frequency
α	Wave characteristic angle
N	Buoyancy frequency

LIST OF FIGURES

Figure 2.1: Schematic of the problem of internal wave reflection at a slope. $\mathbf{C}_g$ and $\mathbf{C}_p$ are group and phase velocity vectors 11
Figure 2.2: Contour plots in $x_s - z_s$ plane of the along-slope velocity at quasi-steady state for a constant slope angle ($\beta = 10°$) and different wave amplitudes: (a) no wave, $Fr = 0$, (b) $Fr = 0.0028$, (c) Fr =0.029. 18
Figure 2.3: Profiles of along slope reflected component velocity $u_{s,ref}$ as a function of wall normal distance taken at $x_s = 1\,m$ for case 3 at different time instances 19
Figure 2.4: Off-critical case FR3 at $Fr = 0.029$ and slope angle of 10°: Power spectra of (a) Along-slope velocity, and (b) Slope-normal velocity , at two different heights $z_s = 0.005$ m and $z_s = 0.17$ m. The solid vertical line represents the frequency when $\omega = N_\infty$. 20
Figure 2.5: Critical case with $Fr = 0.029$ and slope angle of 15°: Power spectra of (a) Along-slope velocity, and (b) Slope-normal velocity, at two different heights $z_s = 0.005$ m and $z_s = 0.17$ m. The solid vertical line represents the frequency when $\omega = N_\infty$. . . 20
Figure 2.6: The development of intensified velocity and patches of turbulence during near-critical reflection is illustrated by spatial x-z cuts at t = 10T for case FR4S10 with $Fr = 0.074$ and offcriticality of 5°. 22
Figure 2.7: Turbulence statistics in a $x-z$ plane are shown for case FR6S10 with $Fr = 0.148$ and near-critical slope angle of 10°. Half the streamwise domain corresponding to a single wavelength is shown. 23
Figure 2.8: Time evolution of turbulent kinetic energy and available potential energy, averaged in slope-normal direction, and measured at mid-slope contrasted between critical and near critical cases. Dashed red color line represents along-slope velocity. 26
Figure 2.9: Spatial contours of turbulent kinetic energy at a quasi-steady state: (a) Case FR6S15, with critical slope angle $\beta = 15°$ and $Fr = 0.148$, is shown at $t = 9.1T$, (b) Case FR6S5 with near-critical slope angle, $\beta = 5°$ and $Fr = 0.148$, ... 28
Figure 2.10: Comparison of terms in the TKE budget between critical and near-critical cases. Time evolution of production, dissipation and buoyancy flux averaged along slope-normal direction at mid-slope. 29
Figure 2.11: Cycle-averaged turbulent statistics at a mid-slope location and spatially averaged over a 0.25 m high boundary region are plotted as a function of off-criticality (degrees) in slope angle: . . 33

Figure 2.12: Turbulent statistics (cycle-averaged and spatially averaged over a 0.25 high boundary region at midslope) as a function of Froude number for a slope angle $\beta = 10°$: 34

Figure 3.1: Schematic of the problem showing a uniform slope of angle β and an incident wave that propagates at an angle α to the horizontal. The reflected wave is also shown for three different scenarios of incident wave angle 44
Figure 3.2: Cross-beam horizontal velocity profile is shown for cases SUP1b (top-hat beam) and SUP2a (Gaussian beam). The forcing parameters are chosen such that the beam width remains the same for Gaussian and top-hat beam profiles. 47
Figure 3.3: Case SUP1e. Contours of horizontal velocity u (m/s) at various time instances show the evolution of PSI. The incident beam travels from the upper left towards the slope. 50
Figure 3.4: Case SUP1e. Frequency spectra of the horizontal velocity: (a) location 1 (left propagating subharmonic wave), (b) location 2 (incident wave), (c) location 3 (reflected wave), and (d) location 4 (right propagating subharmonic wave). (Locations in figure 3.3(c)) 51
Figure 3.5: Kinetic energy spectra for case SUP1e compared among various locations: (a) location 1 (left propagating subharmonic wave), (b) location 2 (incident wave), (c) location 3 (reflected wave), (d) location 4 (right propagating subharmonic wave), ... 52
Figure 3.6: A wave undergoing critical reflection cannot undergo PSI. Panel (a) shows the four quadrants possible for the group velocity vector, $\mathbf{c}_g$, of internal waves that propagate outward from the origin. The corresponding wave number vector, $\mathbf{k}$, ... 55
Figure 3.7: Contours of horizontal velocity u (m/s) for cases SUP1b (left), SUP3 (middle) and SUP4 (right) at time t = 51 T. Incident wave Froude number $Fr_i = 0.03$ is same for all three cases. Case SUP3 has twice the beam width of case SUP1b. 57
Figure 3.8: Contour of horizontal velocity u (m/s) for case F1 at time t = 46 T. A freely propagating wave with the same characteristics as the reflected wave of case SUP3 undergoes PSI as shown in this snapshot. 58
Figure 3.9: Contours of horizontal velocity u, (m/s) for large scale simulations: case SUP7 (upper row) and SUB8 (lower row) at times t = 11.75 T and t = 24T. 58
Figure 3.10: Cycle evolution of area-averaged subharmonic energy (kinetic + potential) for (a) top-hat beam (cases SUP1c-1f), (b) Gaussian beam (cases SUP2c-2f). 60

Figure 3.11: Subharmonic energy growth rates as a function of reflected beam amplitude (Froude number) compared between present simulations and theory of Karimi & Akylas (2014) for a series with top-hat beam profile (series SUP1a-1f). 61
Figure 3.12: Comparison of subharmonic energy growth rates computed from the simulations between top-hat (cases SUP1b-1f) and Gaussian beams (cases SUP2b-2f). 62

Figure 4.1: Schematic of the problem showing the oscillating along-slope velocity profile with width l_b and amplitude U_b.Slope makes an angle β w.r.t the horizontal. The slope-normal coordinate z_s is related to the vertical coordinate 75
Figure 4.2: Density snapshots at various phases during the large convective overturning event from case 2. Top row shows the depth averaged streamwise velocity $\langle u_s \rangle$ (m/s) at various phases during the LCOE. The solid circle 80
Figure 4.3: Cycle evolution (DNS, case 1): (a) TKE budget showing transient term dK/dt, turbulent production P, turbulent dissipation rate ε and turbulent buoyancy flux B; (b) Density variance budget showing transient term $d\langle \rho'^2 \rangle/dt$, ... 82
Figure 4.4: Cycle evolution (LES, case 2) of terms in the (a) TKE budget: transient term dK/dt, turbulent production P, turbulent dissipation rate ε and turbulent buoyancy flux B. (b)Density variance budget: transient term $d\langle \rho'^2 \rangle/dt$, ... 83
Figure 4.5: Density profiles at various time instances are shown for case 1: (a) $\phi = -0.5\pi$ (t=0), (b) $\phi = -0.3\pi$, (c) $\phi = -0.15\pi$, (d) $\phi = 0.03\pi$. The solid line represents the one-dimensional density profile obtained from the three-dimensional density field . . . 86
Figure 4.6: Density profiles at various phases shown for case 2: (a) $\phi = -0.5\pi$ (t=0), (b) $\phi = -0.3\pi$, (c) $\phi = -0.15\pi$, (d) $\phi = 0.03\pi$. The solid line represents the one-dimensional density profile obtained from the three-dimensional density field 87
Figure 4.7: Evolution of APE, buoyancy flux, and diapycnal flux (Φ_d). The upper panel corresponds to case 1 and the lower panel to case 2. The dashed line is the depth-averaged streamwise velocity $\langle u_s \rangle$ (m/s). APE has units of kgm^2s^{-2} whereas 89
Figure 4.8: Distribution of density overturns along the slope-normal direction is shown at four time instances in case 1 (DNS). Mean density profile is used to detect overturns and compute L_T. Time instances chosen are: 92
Figure 4.9: Distribution of density overturns in case 2 (LES). Mean density profile is used to detect overturns and compute L_T. Time instances chosen are: 93

Figure 4.10: Comparison of the phase evolution of Thorpe and Ozmidov scales. Both quantities are multi-valued functions of phase. **Top row**: Panels (a) and (b) show results calculated using the mean density profile for the DNS and LES cases, ... 95
Figure 4.11: The depth-averaged value of turbulent dissipation rate inferred from the Thorpe scales, $\langle \varepsilon_T \rangle_z$, is compared with the actual turbulent dissipation rate in the simulation, $\langle \varepsilon_S \rangle_z$. Both quantities are single-valued functions of phase. **Top row**: 97
Figure 4.12: Evolution of instantaneous mixing efficiency $\eta(t)$ as defined by equation (4.28): (a) case 1 (DNS), (b) case 2 (LES). 100

Figure 5.1: Schematic of SOMAR-LES simulation. Outer box represent SOMAR computational domain. The red colored rectangular box closer to the ridge represent the LES computational domain. 107
Figure 5.2: Schematic showing the time stepping in SOMAR-LES algorithm. 109
Figure 5.3: Horizontal velocity field of tidal flow past Kaena ridge at time (a) $t \approx 1.85T$, (b) $t \approx 2.0T$, (c) $t \approx 2.12T$. 112
Figure 5.4: Horizontal velocity field of tidal flow past model Kaena ridge in a 100 times scaled down domain: (a) $t \approx 1.25T$, (b) $t \approx 1.75T$. 114
Figure 5.5: Left panel show horizontal velocity field averaged in the spanwise direction at different time instances. Similarly, right panel shows vertical rms velocity field at different time instances . . 115
Figure 5.6: Left panel show horizontal velocity field averaged in the spanwise direction at different time instances. Similarly, right panel shows vertical rms velocity field at different time instances . . 115
Figure 5.7: Left panel show horizontal velocity field averaged in the spanwise direction at different time instances. Similarly, right panel shows vertical rms velocity field at different time instances . . 116
Figure 5.8: Density contours at time $t \approx 1.12T$ for (a) case 1, (b) case 2. . 117

LIST OF TABLES

Table 2.1: Parameters of the first series of simulations to study the effect of Froude number, Fr, by varying the wave amplitude. The slope is 5° shallower than the internal wave propagation angle of 15°. The along-slope domain size of $l_{xs} = 2\lambda_{xs} = 2\,m$ 15
Table 2.2: Series A with the amplitude of the incoming wave fixed at $Fr = 0.074$. The role of off-criticality is explored by changing the slope angle. The wave propagation angle is $\alpha = 15°$. FR4S10 has the Froude number of case FR4 (Table 2.1) 16
Table 2.3: Series B with the amplitude of the incoming wave fixed at $Fr = 0.148$. The role of off-criticality is explored by changing the slope angle. The wave propagation angle is $\alpha = 15°$. FR6S10 has the Froude number of case FR6 (Table 2.1) 16
Table 2.4: Ratio of integrated production, mean dissipation, mean buoyancy to the input energy flux, $\mathbb{I}$. The energy input is transferred to turbulent kinetic energy through $\mathbb{P}$, to mean potential energy through $-\mathbb{B}$, and dissipated by 31
Table 2.5: Wall shear stress normalized with incoming wave along slope amplitude,averaged over 10 cycles at a mid-slope location. . . 33

Table 3.1: Properties of the imposed incident wave (subscript i) and the resultant reflected wave (subscript r). The beam amplitude, u_i, is varied in series SUP1 (top-hat beam) and series SUP2 (Gaussian beam). All other cases have top-hat beam profiles. 46
Table 3.2: Domain size and grid parameters for the simulated cases. All dimensions are in meters. 47
Table 3.3: Case SUP1e. Horizontal and vertical wave numbers (m^{-1}) of the left and right subharmonic waves add up to the corresponding values of the incident wave. 54

Table 4.1: Parameters of the simulated cases. Each case has background stratification $N_\infty = 1.6 \times 10^{-3}$ rad/s, frequency $\Omega = 1.407 \times 10^{-4}$ rad/s, and slope angle $\beta = 5°$. The Reynolds number is based on the amplitude of the bottom velocity, U_b, ... 78
Table 4.2: Key results for Case1 (DNS) having bottom flow with peak velocity $U_b = 0.0125$ m/s and width $l_b = 6$ m. First row corresponds to results obtained by averaging over the large convective overturning event (LCOE) that spans 102
Table 4.3: Key results for Case 2 (LES) having bottom flow with peak velocity $U_b = 0.125$ m/s and width $l_b = 60$ m. Quantities defined as in Table 2. 102

Table 5.1: Dimensional parameters for simulations of model Kaena ridge. The kinematic viscosity $\nu = 10^{-5}$ m^2/s for cases 1,2 and 3 and $\nu = 2 \times 10^{-5}$ m^2/s for case 4. Prandtl number $Pr = 7$ for all cases. 113
Table 5.2: Non-dimensional parameters for simulations of Kaena ridge. . . 113
Table 5.3: Grid parameters 113

ACKNOWLEDGEMENTS

I would like to thank my advisor Prof. Sutanu Sarkar for his guidance and support throughout my Ph.D. Also, thanks to all my thesis committee members for their help and suggestions on my thesis work. I am also thankful to all my previous and current lab mates, especially Dr. Gayen for his guidance during the initial stages of my Ph.D. Finally, I would like to thank Prof. Scotti and Dr. Santilli for providing the code SOMAR and for their valuable suggestions during the development of SOMAR-LES model. I am grateful for the financial support provided through the National Science Foundation (NSF) grants OCE-0825705 and OCE-1459774 (program officer Dr. E Itsweire), and the Office of Naval Research (ONR) grant N00014-09-1028 (program officer Dr. T. Paluszkiewicz).

The contents of Chapter 2 are published in *Journal of Fluid Mechanics*. V. K. Chalamalla, B. Gayen, A. Scotti & S. Sarkar (2013), Turbulence during the reflection of internal gravity waves at critical and near-critical slopes., *Journal of Fluid Mechanics*, *729*, 47–68.

The contents of Chapter 3 has recently been accepted for publication in *Journal of Fluid Mechanics*. V. K. Chalamalla, & S. Sarkar (2015) PSI in the case of internal wave beam reflection at an uniform slope., *Journal of Fluid Mechanics* (*in press*).

The contents of Chapter 4 are published in *Journal of Physical Oceanography*. V. K. Chalamalla, & S. Sarkar (2015) Mixing, dissipation rate, and their overturn-based estimates in a near-bottom turbulent flow driven by internal tides., *Journal of Physical Oceanography*, *45*, 1969–1987.

The contents of Chapter 5 are in the process of preparation for publication in *Ocean Modeling*. V. K. Chalamalla, E. Santilli, A. Scotti & S. Sarkar (2015), SOMAR-LES, a coupled ocean-turbulence model, and its application to Kaena Ridge, (in preparation for Ocean Modeling).

VITA

2008	B. Tech. in Mechanical Engineering, Indian Institute of Technology, Guwahati, India
2011	M. S. in Engineering Sciences (Mechanical Engineering), University of California, San Diego, USA
2015	Ph. D. in Engineering Sciences (Mechanical Engineering), University of California, San Diego, USA

PUBLICATIONS

First author journal publications

V. K. Chalamalla, E. Santilli, A. Scotti & S. Sarkar (2015), SOMAR-LES, a coupled ocean-turbulence model, and its application to Kaena Ridge, (in preparation for Ocean Modeling).

V. K. Chalamalla, & S. Sarkar (2015) PSI in the case of internal wave beam reflection at an uniform slope., *Journal of Fluid Mechanics* (*in press*).

V. K. Chalamalla, & S. Sarkar (2015) Mixing, dissipation rate, and their overturn-based estimates in a near-bottom turbulent flow driven by internal tides., *Journal of Physical Oceanography*, *45*, 1969–1987.

V. K. Chalamalla, B. Gayen, A. Scotti & S. Sarkar (2013), Turbulence during the reflection of internal gravity waves at critical and near-critical slopes., *Journal of Fluid Mechanics*, *729*, 47–68.

ABSTRACT OF THE DISSERTATION

Instabilities, Turbulence and Mixing from Internal Waves at bottom topography

by

Vamsi Krishna Chalamalla

Doctor of Philosophy in Engineering Sciences (Mechanical Engineering)

University of California, San Diego, 2015

Professor Sutanu Sarkar, Chair

This study of nonlinear processes and turbulence associated with internal gravity waves has three phases. In the first phase, the reflection problem is studied with simulations involving laboratory-scale slopes whose inclination varies between critical (resonant case with slope angle equal to wave propagation angle) and somewhat off-critical values. We start with three-dimensional direct numerical simulation (DNS) and find strong nonlinearity in the response if the off-criticality is not too large: harmonics in the radiated wave field and cyclical near-bottom turbulence. Subharmonic frequencies are found slightly away from the interaction region in some cases, prompting a followup study with two-dimensional simulations where the underlying mechanism is identified as parametric subharmonic instabil-

ity (PSI) of the reflected wave beam: the sum of the frequencies and the sum of the wave numbers of the daughter subharmonic waves equal the corresponding quantities for the reflected wave. This is the first demonstration that the reflected wave formed when a small-amplitude linear wave is incident on a slope becomes sufficiently nonlinear so as to suffer PSI.

In the second phase, DNS and large eddy simulation (LES) are employed to study the turbulent dissipation and mixing brought about by convective overturns in a stratified, oscillatory bottom layer underneath internal waves. The phasing of turbulence, the onset and breakdown of convective overturns, and the pathway to irreversible mixing are quantified. L_T decreases during the convective instability while L_O increases, which implies that L_T is not linearly related to L_O. Thus, the instantaneous Thorpe-inferred dissipation rates are quite different from the actual values. However, the ratio of their cycle-averaged values is found to be O(1).

In the third phase, a novel modeling technique called SOMAR-LES has been developed wherein a three-dimensional, body-conforming Large Eddy Simulation (LES) model that resolves turbulence scales is coupled with the large-sale Stratified Ocean Model with Adaptive Refinement (SOMAR) to accurately represent small scale turbulence as well as its effect on flow evolution at large scale. Numerical simulations are performed with coupled SOMAR-LES to examine the flow at model Kaena ridge, a steep supercritical generation site.

Chapter 1

Introduction

1.1 Internal Waves

Internal waves are gravity waves that are formed due to disturbances in a vertically stratified fluid. These waves are ubiquitous in the interior of the ocean, and can transport energy over very long distances away from their generation site. The dispersion relation for internal waves in a uniformly stratified, rotating medium can be obtained from the linearized inviscid Navier Stokes equations assuming incompressibility (reasonable assumption for oceanic flows where the Mach number is $<< 1$). The density of the fluid is given by $\rho = \rho_0 + \bar{\rho}(z) + \rho^*(x, y, z, t)$, where ρ_0 is the reference density which is a constant, $\bar{\rho}(z)$ is the background component which varies only in the vertical direction and ρ^* is the density deviation from the background. The background density and the density deviation are assumed to be much smaller than the reference density (Boussinesq approximation) $\rho^*(x, y, z, t) << \bar{\rho}(z) << \rho_0$ which further simplifies the equations as given below:

$$\frac{\partial u}{\partial x} + \frac{\partial v}{\partial y} + \frac{\partial w}{\partial z} = 0, \tag{1.1a}$$

$$\frac{\partial u}{\partial t} - fv = -\frac{\partial p^*}{\partial x}, \tag{1.1b}$$

$$\frac{\partial v}{\partial t} + fu = -\frac{\partial p^*}{\partial y}, \tag{1.1c}$$

$$\frac{\partial w}{\partial t} = -\frac{\partial p^*}{\partial z} - \frac{g\rho^*}{\rho_0}, \tag{1.1d}$$

$$\frac{\partial \rho^*}{\partial t} = -w\frac{d\rho^b}{dz}. \tag{1.1e}$$

Here, $d\rho^b/dz$ is the background density gradient which is assumed to be constant for simplicity.

Simplifying the above equations leads to the following equation in w:

$$\left(\frac{\partial^2}{\partial x^2} + \frac{\partial^2}{\partial y^2} + \frac{\partial^2}{\partial z^2}\right)\frac{\partial w^2}{\partial t^2} + N_\infty^2 \nabla_h^2 w + f^2\frac{\partial w^2}{\partial z^2} = 0. \tag{1.2}$$

Here $N_\infty^2 = -\frac{g}{\rho_0} d\rho^b/dz$ is the background buoyancy frequency and f is the Coriolis parameter. Assuming a solution of the form $e^{i(kx+ly+mz-\Omega t)}$ and substituting in the equation above, we obtain the dispersion relation for internal waves given by:

$$\Omega^2 = \frac{(k^2+l^2)N_\infty^2 + f^2m^2}{k^2+l^2+m^2}. \tag{1.3}$$

Here k,l and m are the wave numbers in x(streamwise), y(spanwise) and z(vertical) directions respectively. The phase velocity of the internal gravity wave is given by $\mathbf{C_p} = \Omega\bar{\mathbf{K}}/|K|^2$, where $\bar{\mathbf{K}}$ is the wave number vector whose magnitude is given by$|K| = \sqrt{(k^2+l^2+m^2)}$. The group velocity $\mathbf{C_g} = \partial\Omega/\partial k\hat{i} + \partial\Omega/\partial l\hat{j} + \partial\Omega/\partial m\hat{k}$, where $\hat{i}, \hat{j}, \hat{k}$ represent unit vectors in x, y and z directions respectively. After some simple algebra, it can be shown that the phase velocity and group velocity vectors are orthogonal to each other implying that the phase propagation is perpendicular to the direction of energy propagation.

1.2 Mixing due to breaking internal waves

Internal waves exist in the interior of the ocean in many forms such as internal solitons, lee waves, trapped waves, high-mode wave beams and low-mode waves. One important mechanism of internal wave generation in the ocean is associated with tides. When the oscillating barotropic tide encounters an obstacle, fluid parcels are displaced vertically in oscillatory motion, which in a stratified fluid, results in propagating internal waves, the so-called internal tides. The bottom displacement of the internal tides may be much larger than surface manifestation of the barotropic tide. Data from several observational, analytical, numerical and experimental studies estimate the global energy conversion into internal tides to be around 1 TW. The wave field is found to contain several modes such as short wavelength high mode waves which are suscpetiple to breaking near the generation site and long wavelength low mode waves which generally travel long distances from the generation site and dissipate energy at remote locations due to several mechanisms such as wave-wave interactions, reflection from sloping topographies (Nash *et al.*, 2004; Eriksen, 1998) and interaction with mesoscale eddy field (Rainville & Pinkel, 2006).

The energy conversion from barotropic to baroclinic internal tides depends on several parameters such as (1) Excursion number $Ex = U_0/(\Omega l)$, which is the ratio of the excursion length $(2U_0/\Omega)$ of a fluid particle to the length scale of the topography $(2l)$, (2) Steepness or criticality parameter $\gamma = \frac{dh}{dx}/s$, where s is the slope of internal wave characteristic defined by $s = \sqrt{\frac{\Omega^2-f^2}{N^2-\Omega^2}}$, (3) Slope criticality fraction l_{cr}/l. The Hawaiian ridge is an important generation site where the generated high-mode internal tides undergo wave steepening and dissipate energy near the topography. The flow parameters near the Hawaiian ridge corresponds to a small Excursion number $Ex = 0.01$ and supercritical topography with a steepness parameter $\gamma = 4$. However, there are certain regions on the topography with $\gamma = 1$ (critical slope). Several observational and numerical studies were performed to understand the turbulence mechanisms and to quantify the fraction of tidal energy dissipated locally. Field measurements near the south flank of the Kaena ridge (Aucan *et al.*, 2006) found two different mechanisms of turbulence, one during the strong downslope flow and another due to convective overturns during the flow reversal from down to up slope flow. Another field study near the ridge crest (Klymak *et al.*, 2008) found two different zones of turbulence: (i) near the slope with dissipation 2 orders of magnitude larger than open-ocean values and possibly due to the breaking of high-mode internal tides, and (ii) in the upper water column with dissipation that matches typical open ocean estimates the barotropic forcing. The numerical study by (Legg & Klymak, 2008) found isopycnal steepening and enhanced dissipation near the ridge crest similar to the observations, however the dissipation from the numerical model was smaller than the observed dissipation, possibly due to the high viscous damping in the numerical model.

Some large-scale ocean models have employed the hydrostatic approximation to reduce computational cost, but this leads to inaccuracies in capturing the evolution of high-frequency internal waves due to dispersion errors. Some other models which use the non-hydrostatic approximation have been limited to two-dimensional domains. There are several numerical studies using existing large scale ocean models to estimate the fraction of baroclinic energy 'q' that is dissipated near the internal tide generation region. These studies often used large values for viscocity $\approx 10^{-2}$ to 10^{-1} m^2/s, (Legg & Klymak, 2008; Legg & Huijts, 2006; Legg & Adcroft, 2003) to maintain numerical stability. In a numerical study of flow at a cross-section of the double-ridge system of Luzon Strait,(Buijsman *et al.*, 2012) found 17% of the internal tide energy is dissipated locally near the generation site. This study uses MIT GCM with an overturn-based parameterization (Klymak & Legg, 2010) that estimates dissipation rate from overturning length scales. Another numerical study using the POM(Princeton Ocean Model) (Carter *et al.*, 2008) found 19% of local dissipation at the Hawaiian Ridge.

Although significant progress has been made in understanding the generation, propagation and reflection of internal tides at bottom topographies, there is large uncertainty in estimating the dissipation due to the difficulty in directly measuring dissipation from the breaking of overturns spanning couple of hundred meters. The existence of various spatial scales ranging from O(km) to O(cm) and various temporal scales ranging from days to hours and minutes, makes it difficult to resolve all the scales of flow either experimentally or numerically. To accurately quantify dissipation, the effect of small scale processes (shear, convective and parametric subharmonic instabilities) on the large scale flow evolution needs to be represented.

In the first phase of this study, we used a combination of direct numerical simulations (DNS) and two dimensional simulations to study nonlinear processes during internal wave reflection on critical and near critical slopes. In the second phase, direct numerical simulation (DNS) and large eddy simulation (LES) are employed to study the mixing due to convective overturns in a stratified, oscillatory bottom layer underneath internal tides. Simulations in the first and second phases of this study were performed in an idealized setting (small length scales compared to oceanic scales), due to the computational constraints posed by the existing modeling techniques. The primary focus was to capture qualitative features of turbulence mechanisms involved in the generation and reflection of internal waves. A unified model which can bridge the large scale ocean models and small scale turbulence resolving models is required to accurately quantify dissipation. In the third phase, a novel modeling technique called SOMAR-LES has been developed wherein a three-dimensional, body-conforming Large Eddy Simulation (LES) model that resolves turbulence scales is coupled with a large-scale model (Santilli & Scotti, 2015), Stratified Ocean Model with Adaptive Refinement (SOMAR), to accurately represent small scale turbulence as well as its effect on flow evolution at large scale. Numerical simulations are performed with SOMAR-LES to examine flow at the Hawaiian ridge. Several complexities encountered in the realistic oceanic flows such as earth's rotation and non-uniform vertical stratification are considered in this study. The results obtained from the coupled model will be compared against previous observations and results from previous numerical experiments. One major advantage of this coupled model over previous numerical models is that, we do not specify high viscosity in order to stabilize the model. More details of this multi-scale modeling technique is presented in chapter 5 of this dissertation.

This dissertation is organized as follows. Chapter 2 presents direct numerical simulations of internal wave reflection at an uniform slope. Critical and near-critical slopes have been considered to characterize turbulence and explore the differences between critical and near-critical reflection. Chapter 3 presents two-dimensional simulations of internal wave beam reflection with a focus on parametric subharmonic instability (PSI). The wide swath of parameter space considered in this study allowed us to evaluate the effect of wave amplitude, width and shape of wave envelope, and off-criticality in slope angle. We also compare the numerical results with a recent theoretical study. In chapter 4, dissipation and mixing brought about by convective overturns in a stratified, oscillatory bottom layer underneath internal tides is discussed. Accuracy of the method of estimating dissipation rate using Thorpe (overturn) scale is examined by comparing the dissipation rate obtained from numerical data with overturn-based estimates. Chapter 5 presents results from a novel multiscale modeling technique, wherein a three-dimensional, body-conforming Large Eddy Simulation (LES) model that resolves turbulence scales is coupled with a large-scale model, Stratified Ocean Model with Adaptive Refinement (SOMAR).

Chapter 2

Turbulence during internal wave reflection on critical and near-critical slopes

This chapter discusses the first phase of the dissertation. Direct numerical simulations are performed to characterize turbulence during the reflection of internal gravity waves on critical and near-critical sloping bottom. It is hoped that the results will also be of help in interpreting field data, and in particular to determine the phasing of turbulence during internal wave reflection on sloping topographies.

2.1 Introduction

Quantification of oceanic mixing rates is crucial for the correct modeling of the Meridional Overturning Circulation (Vallis, 2000; Park & Bryan, 2000; Wunsch & Ferrari, 2004). Interestingly, the latter is sensitive not only to the magnitude of mixing, but also to its spatial distribution (Saenko, 2005). Several field measurements were presented in recent years which reveal increased mixing and dissipation rates near the boundaries. High levels of dissipation (and by inference, mixing) in bottom layers that can extend to a few 100 meters above the bottom are found near topographic boundaries (Eriksen, 1998; Moum *et al.*, 2002; Nash *et al.*, 2004; Munk & Wunsch, 1998; St. Laurent & Garrett, 2002; Aucan *et al.*, 2006), often associated to tidal frequencies. The barotropic tidal velocity is mild and the barotropic tidal boundary layer is too thin to explain these observations. It is thought that internal tides (internal waves generated at bottom topography by the oscillatory tide) are responsible for the enhanced dissipation. This is due to the peculiar dispersion relationship satisfied by internal waves (Phillips, 1977). The latter constrains the angle α between the horizontal direction and the group velocity vector to satisfy, in the nonrotating case,

$$\sin \alpha = \frac{\Omega}{N_\infty}, \tag{2.1}$$

where Ω is the frequency of the wave (conserved during reflection) and N_∞ the value of the Brünt-Väisälä frequency (buoyancy frequency, assumed constant). A similar relationship exists in the rotating case. As a consequence, when a plane wave reflects off a sloping bottom, the component of the wavenumber of the reflected wave in the direction normal to the group velocity increases by a factor $\sim |\alpha - \beta|^{-1}$, where β is the slope angle of the boundary. When β is close to α (the critical angle), this can lead to high levels of shear and increases the energy density of the reflected wave, leading to the well known break down of the theory in the frequency domain when $\beta = \alpha$ (Dauxois & Young, 1999; Scotti, 2011). Whether coincidentally, or because of a feedback mechanism (Cacchione *et al.*, 2002), the slope β of most continental slopes is close to the critical angle for the semidiurnal internal tide. Thus, critical or near critical reflection is a potentially widespread phenomena that needs to be properly understood in order to quantify its contribution to the global mixing within the ocean. It is worth noting that critical slopes have also been implicated as hot spots of turbulence in generation regions Gayen & Sarkar (2010b, 2011*a*); Bluteau *et al.* (2011).

Theoretically, internal waves have been treated most frequently in the frequency domain (Phillips, 1977; Wunsch, 1968; Thorpe, 1987; Tabaei *et al.*, 2005). However, such approach leads to divergent behavior in the physical quantities at criticality. However, Dauxois & Young (1999) and recently Scotti (2011) have shown that in the time domain a laminar solution can be constructed even at criticality, neglecting nonlinear terms. The latter was used to infer the possible pathways for turbulence to develop. The solution obtained by Scotti (herein referred to as S11) shows that both predominantly shear-driven as well as convective-driven instabilities can be found. The former are mostly found near the boundary. Since the S11 solution is inviscid, its validity in the immediate proximity of the boundary is questionable. However, convectively unstable regions are predicted in patches originating away from the boundary, reminiscent of what was observed in laboratory experiments (DeSilva *et al.*, 1997).

Two-dimensional numerical experiments were performed by Javam *et al.* (1999) to study the non-linear processes induced by internal wave reflection. Higher harmonics were observed near the boundary and attributed by the authors to non-linear interactions between incident and reflected waves. Overturning was seen close to the wall at critical frequency and the region of overturning departed from the wall as the off-criticality increases. Recently, two-dimensional numerical experiments as well as laboratory experiments were performed by Rodenborn *et al.* (2011) to study the reflection of internal wave beams at various slope angles and wave amplitudes. Except for very weak incoming waves, the highest amplitude of the reflected internal wave beam at the second harmonic frequency occured when the slope angle was significantly shallower than the critical angle. This study suggests that reflection at near-critical slopes may also play an important role in turbulence and mixing. A three-dimensional computational model for internal wave reflection was developed by Slinn & Riley (1998*a*) and numerical simulations (DNS and LES using a hyperviscosity) were performed by Slinn & Riley (1998*b*) for cases with critical slope angle. Cyclical turbulence with periodic density overturns was found when the Reynolds number based on wavelength and peak velocity of the incident wave exceeded 1500. Examination of the local value of Richardson number suggested that both shear and convective instabilities could occur.

Previous studies have clearly shed some light on the nonlinear reflection processes that occur when the slope is critical. However, there seems to be no clarity regarding the mechanism of transition to turbulence, whether initiated by convective or shear instabilities. The importance of off-criticality is still obscure i.e whether it is the critical reflection or near off-critical reflections which plays the major role in mixing over the slopes. Also, the effect of slope angle and incoming wave strength on the reflection process needs better understanding. In view of these outstanding questions, we have performed a DNS study where the slope angle is systematically changed for various incoming wave Froude numbers and the numerical data is examined to identify the instabilities that lead to turbulence, to characterize the phasing of turbulence in the quasi-steady state, and to ascertain differences between critical and off-critical reflection as a function of incoming wave amplitude.

The paper is organized as follows: Section 2 describes the formulation of the problem, boundary and initial conditions. Sections 3 presents results for laminar cases that are compared with analytical solution. Section 4 discusses the mechanism and phasing of turbulence events. Section 5 describes the parametric dependance of turbulent kinetic energy and dissipation. The paper concludes with a summary of the results of the present numerical experiments.

2.2 Formulation of the problem

2.2.1 Governing equations

Direct numerical simulation is used to solve the Navier-Stokes equations, under the Boussinesq approximation in a non rotating environment. The Navier-Stokes equations for dimensional variables (denoted by subscript d) are written as

$$\nabla \cdot \mathbf{u}_d = 0, \tag{2.2a}$$

$$\frac{D\mathbf{u}_d}{Dt_d} = -\frac{1}{\rho_0}\nabla p_d^* - \frac{g\rho_d^*}{\rho_0}\hat{\mathbf{k}} + \nu\nabla^2\mathbf{u}_d, \tag{2.2b}$$

$$\frac{D\rho_d}{Dt_d} = \kappa\nabla^2\rho_d\,. \tag{2.2c}$$

Here, p_d^* denotes deviation from the background hydrostatic pressure and ρ_d^* denotes the deviation from the linear background state, $\rho_d^b(z_d)$. The quantities u_d, v_d, w_d denote streamwise, spanwise and vertical velocity, respectively. The evo-

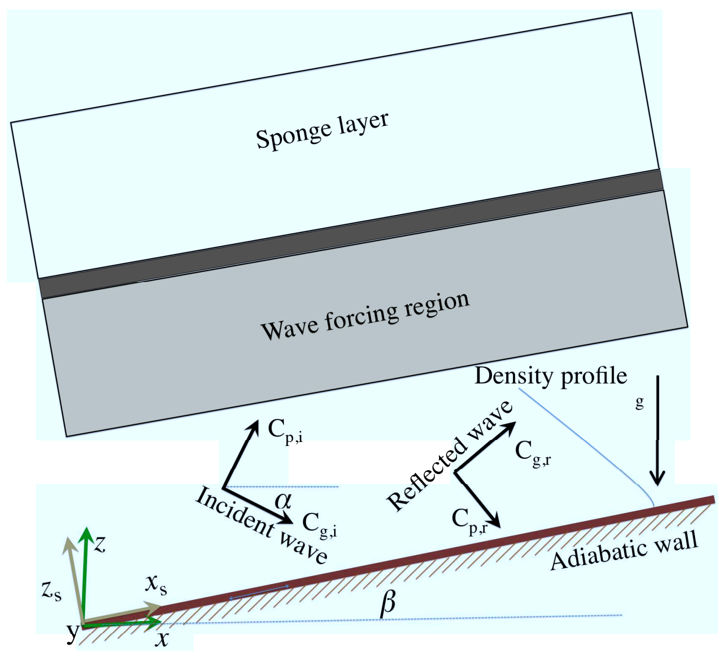

Figure 2.1: Schematic of the problem of internal wave reflection at a slope. $\mathbf{C}_g$ and $\mathbf{C}_p$ are group and phase velocity vectors respectively. The slope makes an angle β with respect to the horizontal and the angle that the phase lines make with the horizontal is denoted by α. The density profile shown is referenced to the slope normal axis z_s. The coordinate, z_s, is related to the vertical coordinate z by $z = x_s \sin\beta + z_s \cos\beta$.

lution equation for ρ_d^*, the deviation density, is written as

$$\frac{D\rho_d^*}{Dt_d} = \kappa \nabla^2 \rho_d^* - w_d \frac{d\rho_d^b}{dz_d}\,. \tag{2.3}$$

The dimensional parameters in the problem are the amplitude of the incident wave velocity in the x-direction U_0, frequency Ω, x-direction wave number k_d, background density gradient $d\rho_d^b/dz_d$, gravity g and the fluid properties: molecular viscosity, ν, thermal diffusivity, κ, reference density, ρ_0. The variables in the problem are nondimensionalized as follows:

$$\left.\begin{array}{c} t = t_d\Omega,\ \mathbf{x} = (x,y,z) = \dfrac{(x_d, y_d, z_d)}{1/k},\ p^* = \dfrac{p_d^*}{\rho_0 U_0 \Omega / k_d}, \\ \mathbf{u} = (u,v,w) = \dfrac{(u_d, v_d, w_d)}{U_0}, \quad \rho^* = \dfrac{\rho_d^*}{\rho_0 U_0 \Omega / g}. \end{array}\right\} \tag{2.4}$$

The resulting non-dimensional form of the governing equations is:

$$\nabla \cdot \mathbf{u} = 0, \tag{2.5a}$$

$$\frac{\partial \mathbf{u}}{\partial t} + Fr(\mathbf{u}\cdot\nabla)\mathbf{u} = -\nabla p^* - \rho^* \mathbf{k} + \frac{Fr}{Re}\nabla^2 \mathbf{u}, \tag{2.5b}$$

$$\frac{\partial \rho^*}{\partial t} + Fr(\mathbf{u}\cdot\nabla)\rho^* = Fr Re^{-1} Pr^{-1} \nabla^2 \rho^* + \frac{{N_\infty}^2}{\Omega^2} w. \tag{2.5c}$$

The non-dimensional parameters that govern the flow are the Reynolds number Re, Froude number Fr, ${N_\infty}^2/\Omega^2$ and Prandtl number Pr, defined as follows:

$$Re = \frac{U_0}{\nu k_d}, \quad Fr = \frac{U_0 k_d}{\Omega}, \quad \frac{{N_\infty}^2}{\Omega^2} = -\frac{g}{\rho_0 \Omega^2}\frac{d\rho_d^b}{dz_d}, \quad Pr = \frac{\nu}{\kappa}. \tag{2.6}$$

The Froude number $Fr = U_0 k_d/\Omega$ as defined here measures the distance of wave self-advection relative to the wavelength and thus the nonlinearity of the incoming wave. Note that $Fr/\sqrt{\frac{{N_\infty}^2}{\Omega^2}} = U_0 k_d / N_\infty$ can be taken as a measure of the nonlinearity of the highest frequency internal wave in the system.

The dimensional form of the governing equations in the reference axis system $[x_s, y_s, z_s]$ rotated by an angle β in x-z plane is given by,

$$\begin{aligned}
\nabla \cdot \mathbf{u}_s &= 0, &\text{(2.7a)}\\
\frac{D\mathbf{u}_s}{Dt} &= -\frac{1}{\rho_0}\nabla p^* - \frac{g\rho^*}{\rho_0}(\sin\beta\mathbf{i} + \cos\beta\mathbf{k}) + \nu\nabla^2\mathbf{u}_s, &\text{(2.7b)}\\
\frac{D\rho^*}{Dt} &= \kappa\nabla^2\rho^* - \frac{d\rho^b}{dz}(u_s\sin\beta + w_s\cos\beta). &\text{(2.7c)}
\end{aligned}$$

Here, u_s, v_s, w_s are along-slope , spanwise and slope-normal velocities respectively in a rotated coordinate system. Subscript d for dimensional variables is dropped for convenience. Equations 2.6(a)-(c) will be solved numerically, details of the numerical method are discussed in the following section.

2.2.2 Wave forcing

Volumetric body forcing (Slinn & Riley (1998*b*)) is employed to generate incident waves that propagate towards the slope from above and subsequently reflect as shown in figure 2.1. The cases to be considered are at critical slope angle and somewhat off-critical. Volume forcing has been implemented here by adding forcing functions (F_u,F_w,-$\frac{d\rho^b}{dz}F_\rho$)to the right-hand side of the u_s,w_s and ρ equations in the rotated coordinate system as follows:

$$\begin{gathered}
F_u = -\frac{A_0 m_s}{k_s}F(z_s)\cos(k_s x_s + m_s z_s - \omega t) - \frac{A_0}{k_s}F'(z_s)\sin(k_s x_s + m_s z_s - \omega t),\\
F_w = A_0 F(z_s) cos(k_s x_s + m_s z_s - \omega t),\\
F_\rho = -\frac{A_0\cos(\beta)}{\omega}F(z_s)\sin(k_s x_s + m_s z_s - \omega t) + \frac{A_0 m_s\sin(\beta)}{\omega k_s}F(z_s)\\
\sin(k_s x_s + m_s z_s - \omega t) - \frac{A_0\sin(\beta)}{\omega k_s}F'(z_s) cos(k_s x_s + m_s z_s - \omega t).
\end{gathered} \tag{2.8}$$

Here, $F(z_s)$ is the localization function given by $F(z_s) = \exp[-b(z_s - z_{s0})^2]$, the parameter z_{s0} is the center of the forcing region, $b = 50\ m^{-2}$. A_0 is chosen to impose a given value of Fr. At low Fr with domain height of 2 m, the forcing region is centered at $z_{s0} = 1.1$ m and is between $z_s = 0.85$ m and $z_s = 1.35$ m. At high Fr with domain height of 4 m, the forcing region is centered at $z_{s0} = 1.8$ m and is between $z_s = 0.1.55$ m and $z_s = 2.05$ m. In order to prevent the spurious accumulation of energy near the forcing region in the near-critical cases with higher Froude number ($Fr = 0.11$ and 0.148), a high-order filter is applied to the velocity field (u_s, v_s, w_s) in the slope-normal direction. Filtering is limited to a region between $z_s = 1.5$ m and $2.5m$ that is far away from the turbulent near-boundary region. A fourth-order compact filter with the filter width parameter $\alpha = 0.48$ (Lele, 1992) is chosen so that only the highest wavenumbers are affected.

2.2.3 Boundary conditions

No slip boundary conditions has been imposed at the bottom boundary for u_s,v_s,w_s.

The total density can be written as summation of background density, incident and reflected components of deviation densities:

$$\rho = \rho_0 - z_s \cos\beta - x_s \sin\beta + \rho^*. \tag{2.9}$$

Zero mass flux boundary condition is imposed at the sloping bottom resulting in the density deviation at the sloping boundary given by

$$\frac{\partial \rho^*}{\partial z_s} = \cos\beta. \tag{2.10}$$

2.2.4 Numerical method

The simulations use a mixed spectral/finite difference algorithm. Derivatives in the streamwise and spanwise directions are treated with a pseudo-spectral method and derivatives in the vertical direction are computed with second-order finite differences. A staggered grid is used in the wall-normal direction. A low-storage third-order Runge-Kutta-Wray method is used for time stepping, and viscous terms are treated implicitly with the Crank-Nicolson method. The code has been parallelized using the message passing interface (MPI). Periodicity is imposed in the x_s and y_s directions. The top boundary is an artificial boundary corresponding to the truncation of the domain in the vertical direction. Rayleigh damping or

Table 2.1: Parameters of the first series of simulations to study the effect of Froude number, Fr, by varying the wave amplitude. The slope is 5° shallower than the internal wave propagation angle of 15°. The along-slope domain size of $l_{xs} = 2\lambda_{xs} = 2\,m$ permits 2 wave lengths and the spanwise length is $l_{ys} = 0.25\,m$. For cases FR1-FR4, the domain height is $l_{zs} = 2.0\,m$ and, for cases FR5 and FR6, $l_{zs} = 4.0\,m$. Multiply Re by 2π to obtain Reynolds number based on horizontal wavelength,λ, instead of the horizontal wave number, k. In all these simulations, the ratio Fr/Re is kept constant which is $\approx 10^{-4}$.

Case	$U_0\,ms^{-1}$	Fr	Re	α	β	Remark
FR1	0.0	0.0	0	15°	10°	Laminar
FR2	1.0E-4	0.003	26	15°	10°	Laminar
FR3	1.1E-3	0.029	286	15°	10°	Laminar
FR4	2.8E-3	0.074	750	15°	10°	Turbulent
FR5	4.3E-3	0.110	1114	15°	10°	Turbulent
FR6	5.7E-3	0.148	1484	15°	10°	Turbulent

a sponge layer is used to minimize spurious reflections from the artificial boundary into the computational domain. The velocity and scalar fields are relaxed towards the background state in the sponge region by adding damping functions -$\sigma(z_s)\,[(u_s, v_s, w_s)]$ and $-\sigma(z_s)\,[\rho^*]$ to the right hand side of the momentum and scalar equations, respectively. The sponge region lies between $z_s = 1.5$ m and 2 m in the low Fr cases with domain height of 2 m, and between $z_s = 2.5$ m and 4 m at the higher $Fr = 0.148$ cases with domain height of 4 m. The value of $\sigma(z_s)$ increases exponentially from zero at the bottom boundary of the sponge to a maximum value of $\sigma(z_s)\Delta t \sim \mathcal{O}(0.1)$. The pressure boundary conditions are $p^* = 0$ at the bottom wall (due to staggered grid) and $\partial p^*/\partial z_s = 0$ at the top of computational domain. Variable time stepping with a fixed CFL number of 1.2 is used. All the simulations are well resolved with $\Delta x^+ \leq 20$, $\Delta y^+ \leq 10$, $\Delta z^+ \leq 2$ in terms of the viscous wall unit ν/u_τ. Here, $u_\tau = \sqrt{\frac{\tau_w}{\rho}}$, with τ_w denoting the shear stress at the wall defined as follows:

$$\tau_w = \mu\sqrt{\left(\frac{du_s}{dz_s}\right)^2_{z_s=0} + \left(\frac{dv_s}{dz_s}\right)^2_{z_s=0}}. \tag{2.11}$$

In all the simulated cases, the wave has the same horizontal wave number

Table 2.2: Series A with the amplitude of the incoming wave fixed at $Fr = 0.074$. The role of off-criticality is explored by changing the slope angle. The wave propagation angle is $\alpha = 15°$. FR4S10 has the Froude number of case FR4 (Table 2.1) and a slope angle of 10°, similarly for other cases. The domain size is $l_{xs} = 2\lambda_{xs}\, m$, $l_{ys} = 0.25\, m$, $l_{zs} = 2.0\, m$. The Grid size is $N_x = 256$, $N_y = 64$, $N_z = 221$.

$Case$	$Fr = U_0k/\Omega$	β	Remark
FR4S15	0.074	15°	Transition
FR4S10	0.074	10°	Turbulent
FR4S5	0.074	5°	Transition

Table 2.3: Series B with the amplitude of the incoming wave fixed at $Fr = 0.148$. The role of off-criticality is explored by changing the slope angle. The wave propagation angle is $\alpha = 15°$. FR6S10 has the Froude number of case FR6 (Table 2.1) and slope angle of 10°, similarly for other cases. The domain size is $l_{xs} = 2\lambda_{xs}\, m$, $l_{ys} = 0.25\, m$, $l_{zs} = 4.0\, m$. The Grid size is $N_x = 512$, $N_y = 128$, $N_z = 449$.

$Case$	$Fr = U_0k/\Omega$	β	Remark
FR6S15	0.148	15°	Turbulent
FR6S10	0.148	10°	Turbulent
FR6S5	0.148	5°	Turbulent

$k = 3.84m^{-1}$, frequency $\Omega = 0.15s^{-1}$ corresponding to a time period of $T = 41.9s$, and internal wave angle $\alpha = 15°$. The background stratification is $N_\infty = 0.5795s^{-1}$ and kinematic viscosity is $\nu = 10^{-6}m^2/s$. The corresponding non-dimensional parameters are ${N_\infty}^2/\Omega^2 = 14.928$ and Prandtl number $Pr = 1.0$.

Three series of simulations are performed. Table 2.1 shows parameters for a series of simulations at a constant value of a near-critical slope angle ($\beta = 10°$), wave angle of $\alpha = 15°$, and six values of incoming Froude number, Fr. The set of simulations, series A with parameters listed in table 2.2, was performed to explore the effect of off-criticality at a fixed low value of $Fr = 0.074$ by changing the slope angle. Series B with parameters listed in table 2.3 is analogous to series A but at a higher $Fr = 0.148$.

2.2.5 Turbulence diagnostics

Any fluctuating quantity in the flow field is defined by subtracting the spanwise average from the instantaneous value.

$$A' = A - \langle A \rangle_y, \tag{2.12}$$

$$\langle A \rangle_y = \frac{1}{l_y} \int_0^{l_y} A \, dy. \tag{2.13}$$

Detailed analysis of the TKE budget is important to understand the mechanisms underlying the phasing of turbulence. The evolution of TKE is governed by the following equation:

$$\frac{dK}{dt} = P - \epsilon + B - \frac{\partial T_i'}{\partial x_j}, \tag{2.14}$$

where $K = 1/2\langle u_i' u_i' \rangle_y$, $P = -\langle u_i' u_j' \rangle_y \langle S_{ij} \rangle_y$, $\epsilon = \nu \langle \frac{\partial u_i'}{\partial x_j} \frac{\partial u_i'}{\partial x_j} \rangle_y$, $B = \frac{g_i}{\rho_0} \langle \rho^{*\prime} u_i' \rangle_y = -\frac{g}{\rho_0} \langle \rho^{*\prime} w' \rangle_y$, $T_i' = \frac{1}{\rho_0} \langle p^{*\prime} u_j' \rangle_y - 2\nu \langle u_i' s_{ij}' \rangle_y + \frac{1}{2} \langle u_i' u_i' u_j' \rangle_y$. Here, K denotes turbulent kinetic energy, P is production, ϵ is turbulent dissipation rate, B is buoyancy flux with w' denoting the vertical velocity, $\frac{\partial T_i'}{\partial x_j}$ is the transport of turbulent kinetic energy with $s_{ij}' = \frac{1}{2}(\frac{\partial u_i'}{\partial x_j} + \frac{\partial u_j'}{\partial x_i})$.

Averaging over slope-normal coordinate and over several cycles is employed to quantify turbulent statistics used to compare results at different Fr and slope angles. These averages are calculated as follows,

$$\langle A \rangle_{zt} = \frac{1}{z_1 t_1} \int_0^{z_1} \int_{t_1}^{t_2} A \, dt \, dz_s, \tag{2.15}$$

where $z_1 = 0.25m$, t_1 and t_2 are chosen such that the averaging includes a minimum of 4 cycles in the quasi-steady state.

2.3 Laminar regime

The wave amplitude intensifies during reflection from a near-critical slope. However, when the incoming wave amplitude is small and the corresponding value

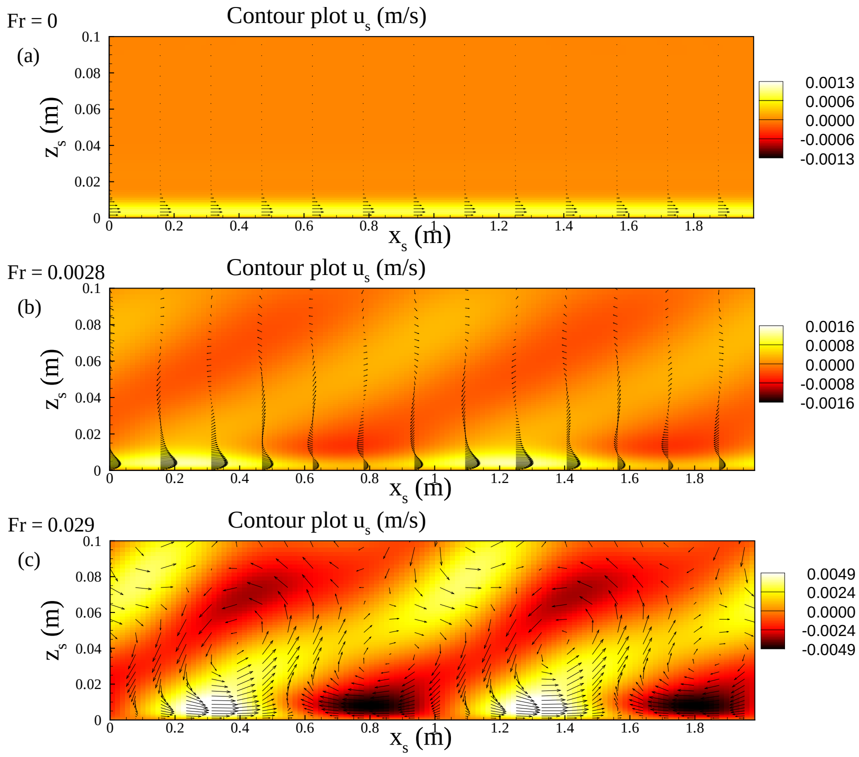

Figure 2.2: Contour plots in $x_s - z_s$ plane of the along-slope velocity at quasi-steady state for a constant slope angle ($\beta = 10°$) and different wave amplitudes: (a) no wave, $Fr = 0$, (b) $Fr = 0.0028$, (c) Fr =0.029. Velocity vectors are also shown. Note that the z_s axis corresponds to a smaller distance relative to the x_s axis. The ratio Fr/Re is constant ($\approx 10^{-4}$) in all these cases, even when there is no wave (i.e Fr=0).

of $Fr << 1$, the flow field associated with the reflected wave remains laminar. The effect of Fr in the laminar flow regime is discussed here.

2.3.1 Velocity field

Figure 2.2 shows the contour plots of along-slope instantaneous velocity field for cases FR1, FR2 and FR3 of table 2.1. Figure 2.2(a) corresponds to $Fr = 0$ with no forcing. The zero mass flux boundary condition at the inclined wall creates a slope-wise density gradient resulting in a thin boundary layer (Phillips (1970), Wunsch (1970)) with a steady upslope flow, $u_s(z_s)$, that is established by a balance between viscous and buoyancy forces. The Phillips-Wunsch solution is realized in the absence of wave forcing as illustrated by figure 2.2(a). Figure 2.2 (b)-(c) show

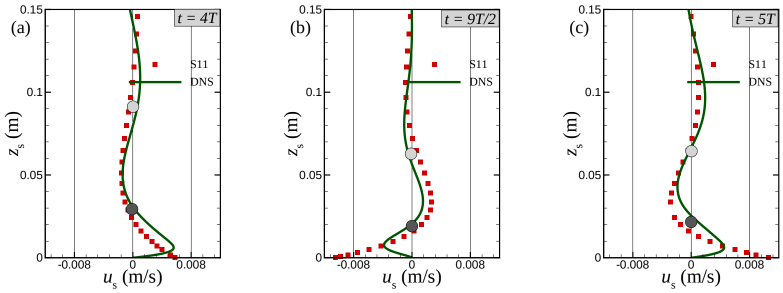

Figure 2.3: Profiles of along slope reflected component velocity $u_{s,ref}$ as a function of wall normal distance taken at $x_s = 1\ m$ for case 3 at different time instances with a time gap of half wave period . Corresponding profiles of theoretical solution by AS are also shown in the figure

a reflected wave of along-slope wavelength 1 m that propagates at 15° angle to the horizontal corresponding to an angle of 5° relative to the boundary. With increasing wave forcing, the unidirectional boundary velocity field of the Phillips-Wunsch solution is dominated by the oscillatory wave response.

Numerical results for case FR3 are compared with the analytical solution obtained using linear inviscid theory by S11. Figures 2.3(a)-(c) shows the profiles of along-slope velocity. As time progresses, the velocity intensifies until it reaches a steady state after approximately 5 cycles. The vertical wavelength of the velocity decreases during the transient, as can be observed from the shortening distance between successive zero velocity points in figure 2.3. Numerical results and the analytical solution are in good quantitative agreement in the region outside the boundary layer. Within the boundary layer, since viscous effects are prominent, the inviscid analytical solution deviates from DNS. In the inviscid analytical solution, the maximum along-slope velocity is at the bottom boundary, whereas it is maximum away from the wall in the DNS.

2.3.2 Frequency spectra

The distribution of energy among different frequencies is discussed in this section. Figure 2.4 shows the power spectrum of along-slope and slope-normal velocity for case FR3, a case with off-criticality of 5° and $Fr = 0.029$, at two locations. The spectra are evaluated over a period of 6 cycles.The spectra exhibit

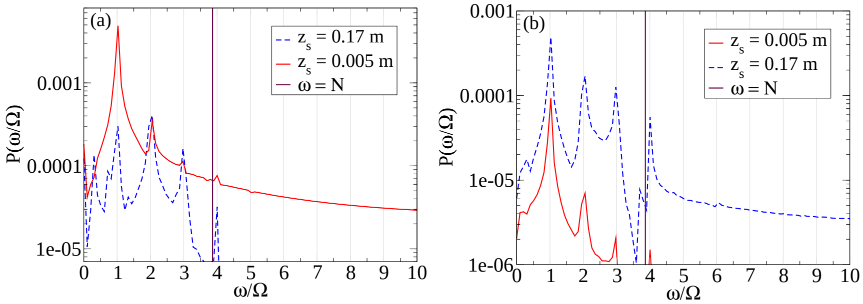

Figure 2.4: Off-critical case FR3 at $Fr = 0.029$ and slope angle of 10°: Power spectra of (a) Along-slope velocity, and (b) Slope-normal velocity , at two different heights $z_s = 0.005$ m and $z_s = 0.17$ m. The solid vertical line represents the frequency when $\omega = N_\infty$.

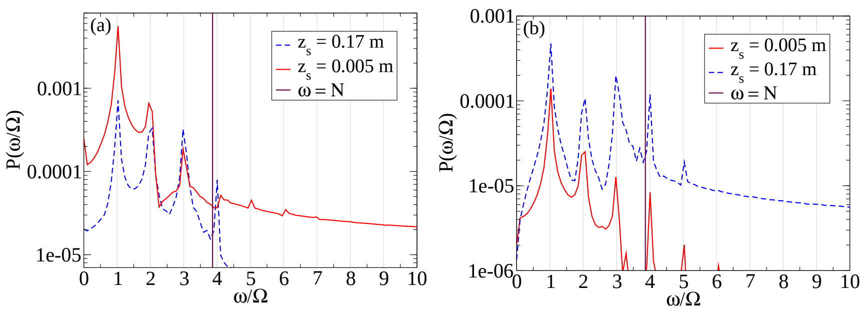

Figure 2.5: Critical case with $Fr = 0.029$ and slope angle of 15°: Power spectra of (a) Along-slope velocity, and (b) Slope-normal velocity, at two different heights $z_s = 0.005$ m and $z_s = 0.17$ m. The solid vertical line represents the frequency when $\omega = N_\infty$.

discrete frequencies in the form of multiples of the forcing harmonic ($n\Omega, n \in N$). These peaks carry a substantial fraction of the energy at $z_s = 0.17$ m. There are also local peaks at sub-harmonic frequencies of approximately, 0.3Ω and 0.7Ω.

To compare the spectra in case FR3 with 5° offcriticality with those in the case of critical slope, another simulation is done at an exactly critical slope angle and the results shown in Figure 2.5. The spectra do not exhibit qualitative changes. One difference is that the spectrum of vertical velocity drops rapidly for $\omega > N_\infty$ in the near-critical case but, when the slope angle is critical, the spectra show some discrete peaks for $\omega > N_\infty$, that may correspond to forced waves generated and trapped in the near-boundary region.

2.4 Turbulent regime

At sufficiently high values of incoming Froude number, the energy density in the reflected wave field is found to be large enough for stratified, phase-dependent turbulence to develop when the slope is either critical or somewhat off-critical. The inviscid, linear analysis of S11 concluded that, during the transient evolution of a near-critical reflected wave, unstable regions could occur and the present results are in agreement with that conclusion. DNS allows us to go beyond theory by making precise the mechanism of transition to turbulence during near-critical reflection as will be shown in section 2.4.1 and quantify the role of turbulence during the flow evolution. After the transient buildup of turbulence, the flow statistics reach an approximately quasi-steady dependence on wave phase. The phasing of turbulence during this quasi-steady state is found to have qualitative differences between critical and near-critical cases as described in section 2.4.2.

2.4.1 Development of turbulence in near-critical cases

During the transient evolution of the reflected wave, the fluid velocity increases and, correspondingly, the density deviation from the background increases. Since the near-bottom vertical wavelength also decreases, the isopycnals steepen leading to the possibility of wave breaking and turbulence. The simulations show wave breaking within one wavelength from the boundary. Figures 2.6(a) and 2.6(b) show contour plots of along slope velocity and turbulent kinetic energy for case FR4S10 at time t = 10T. The velocity contours in part (a) show the spatially periodic field corresponding to an internal wave as well as the velocity intensification (approximately 5 times that of the incoming wave) expected for near-critical reflection. The TKE field in part (b) shows two locations of turbulence within a span of a single along-slope wavelength. These two turbulence patches, one close to the wall and another away from the wall, appear periodically during a cycle at any given streamwise coordinate. After the initial transient, the amplitude of the oscillatory TKE in these patches remains approximately constant corresponding to a quasi-steady state. Figures 2.6(c) and (d) show vertical density profiles at

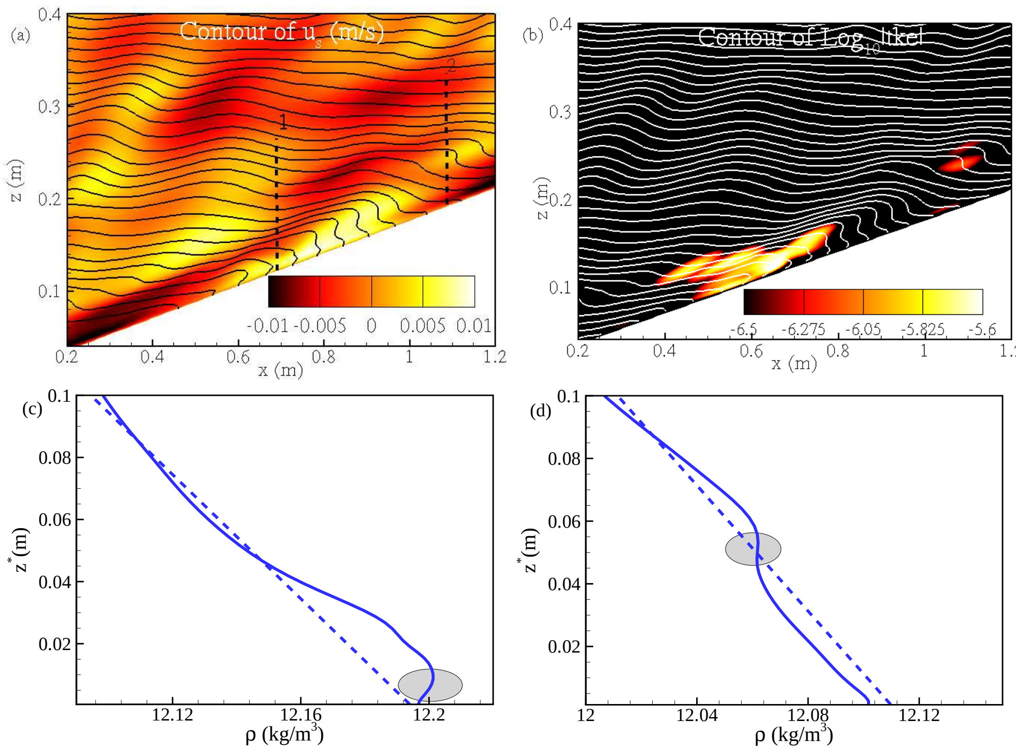

Figure 2.6: The development of intensified velocity and patches of turbulence during near-critical reflection is illustrated by spatial x-z cuts at t = 10T for case FR4S10 with $Fr = 0.074$ and offcriticality of 5°: (a) Contour of along slope velocity, (b) Contour of turbulent kinetic energy. Half the streamwise domain size, corresponding to a single wavelength, is shown. Convectively unstable regions (shaded ellipses) shown by profiles of density as a function of height from bottom at (c) location 1 and (d) location 2. These locations are indicated by dotted lines in (a).

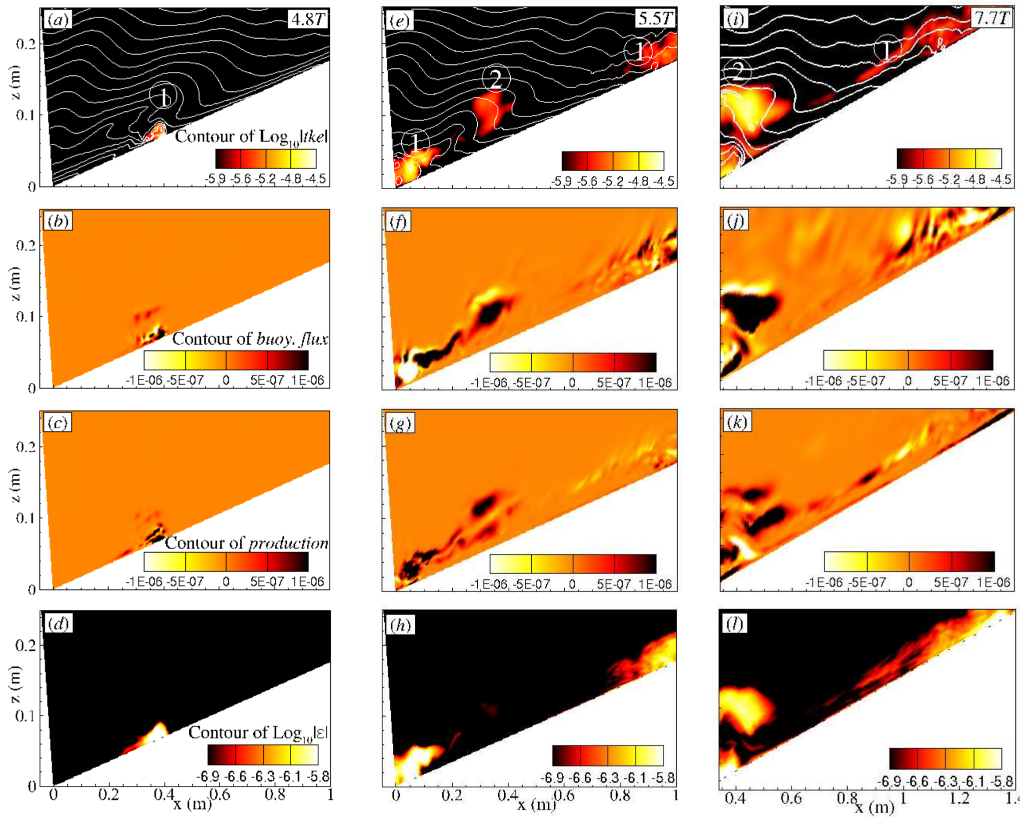

Figure 2.7: Turbulence statistics in a $x-z$ plane are shown for case FR6S10 with $Fr = 0.148$ and near-critical slope angle of 10°. Half the streamwise domain corresponding to a single wavelength is shown. Column 1 corresponds to at an early time of t = 4.8 T, column 2 to a later time of t = 5.5 T, and column 3 to t = 7.7T close to the quasi-steady state. Rows from top to bottom show TKE, buoyancy flux, turbulent production and turbulent dissipation rate.

locations 1 and 2 indicated in (a). The grey shaded regions in figures 2.6(c) and 2.6 (d) are convectively unstable regions that correspond to turbulence locations near the wall and further away from the wall, respectively.

We now move to the development of turbulence in case FR6S10 with the same value of off-criticality, 5°, as case FR4S10, but with a higher incoming wave amplitude corresponding to $Fr = 0.148$. Figure 2.7 shows contours of turbulent statistics in case FR6S10 at 3 time instances. Figures 2.7(a)-(d), comprising column 1, show the onset of turbulence near the wall. Figure 2.7(e)-(h) correspond to a later time when another patch of turbulence develops away from the wall. Figure 2.7(i)-(l) corresponds to the fully-developed, quasi-steady state. At early time, t= 4.8T, there is a single patch of turbulence near the boundary, denoted by 1 in figure 2.7(a). At intermediate time, t = 5.5T, the near-wall patch 1 has strengthened and grown spatially. There is also an additional patch of turbulence detached from the boundary, denoted by 2. At time, t = 7.7T, the detached patch 2 is stronger in amplitude and also spatially larger. Examination of the isopycnals in front of the near-wall turbulence patch shows the presence of a thermal front with high streamwise temperature (density) variation. This front is found to propagate upslope as observed in previous laboratory experiments, e.g., Ivey & Nokes (1989), Thorpe (1992). Figure 2.7 (second row) shows positive buoyancy flux, associated with convective instability, at all locations with enhanced TKE while positive values of production are also seen in figure 2.7 (third row). Noteworthy is the behavior at quasi-steady state (column 3) where the correspondence of the detached large patch 2 of TKE to a similar large patch of positive buoyancy is clear.High dissipation is seen at all locations with enhanced TKE.

The analytical solution derived by S11 was evaluated for case FR6S10. In the analytical solution, a statically unstable region develops initially at the wall at a time that is earlier than the DNS (where the first turbulence patch is observed at 4.8T), during flow reversal from downslope to upslope. Owing to the absence of the viscous boundary layer in the analytical solution, the statically unstable region during the other flow reversal event from upslope to downslope that was seen in the DNS is absent in the analytical solution. At later time, a statically unstable region develops away from the wall and merges with the initial region so the region that could potentially break in the analytical solution to give turbulence is large. However, in the DNS, turbulence is found only in the region between the solid boundary and the first zero-crossing of the horizontal velocity. Evidently, in the simulations, turbulent mixing of the density and turbulent dissipation of momentum both change the isopycnal distribution above the first zero-crossing to prevent the internal wave from breaking into turbulence.

The TKE level increases with increasing wave amplitude. More interestingly, the spatial distribution of turbulence also depends on the incoming wave amplitude. At low Fr = 0.074, the patch near the boundary has higher TKE compared to the patch detached from the boundary as was noted earlier in figure 2.6(b). In contrast, for case FR6S10 with higher $Fr = 0.148$, TKE in the patch away from the wall is almost of the same magnitude as that in the patch near the wall. This is because, away from the boundary, the increase in the magnitude of density deviation caused by the higher wave amplitude of case FR6S10 is able to cause a thicker region of unstable density leading to a larger positive buoyancy flux and more intense turbulence. In contrast, the wall boundary condition limits the thickness of the overturning region that develops adjacent to the bottom boundary.

2.4.2 Comparison of turbulence between critical and near-critical cases

The nonlinear response differs qualitatively between critical and near-critical slopes. For instance, at low $Fr = 0.074$, there is little turbulence during critical reflection while the case with 5° off criticality has substantial TKE and turbulent dissipation. Qualitative differences in near-bottom turbulence are discussed in this section by comparing cases FR6S15 (critical) and FR6S5 (10° off-criticality). Both cases have $Fr = 0.148$, wave propagation angle of 15°, and develop substantial levels of turbulence.

We now turn to the temporal phasing of turbulence. The time evolution of turbulent kinetic energy along with available potential energy, $APE = g^2\rho^{*2}/(2{\rho_0}^2{N_\infty}^2)$ with ρ^* denoting the deviation from the background density, is shown for critical and near-critical slope reflection in figure 2.8. Both quantities are averaged over the slope-normal coordinate, $0 < z_s < 0.25$ m. The slope-wise velocity is also plotted to show the relative phases of peak TKE and APE. In the critical case, turbulence is initiated at cycle 4.5 as shown in figure 2.8(a). A peak in available potential energy occurs twice each cycle shortly prior to the zero-velocity point as shown by downward pointing arrows 1 and 3. The TKE increases when the available potential energy is maximum (arrow 1) and it peaks as marked by arrow 2 before the upslope velocity reaches its maximum value. However, no peak of TKE is found after the peak potential energy (arrow 3) during the flow reversal from upslope to downslope motion.

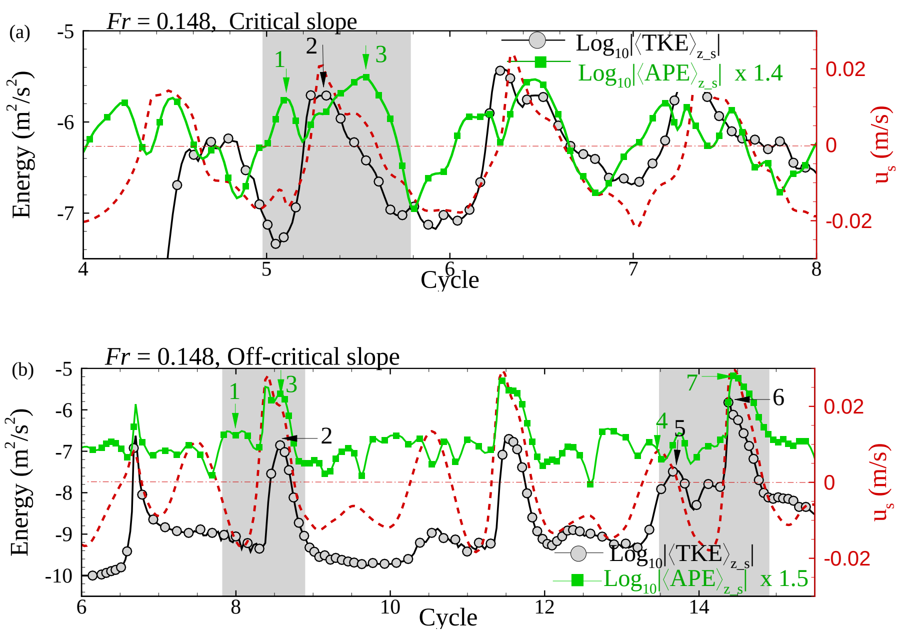

Figure 2.8: Time evolution of turbulent kinetic energy and available potential energy, averaged in slope-normal direction, and measured at mid-slope contrasted between critical and near critical cases. Dashed red color line represents along-slope velocity. The cases have wave angle of $\alpha = 15°$ and $Fr = 0.148$: (a) Critical slope angle $\beta = 15°$ (b) Near-critical slope angle $\beta = 5°$

The phasing of turbulence during near-critical reflection is shown in figure 2.8(b) and is now contrasted with the critical case. The important difference is that the TKE peaks skip cycles in contrast to the critical case where there is one TKE peak every cycle. During near-critical reflection, the first peak in TKE is found at t =6.5T as shown in figure 2.8(b). The next peak of TKE at approximately t = 8.5T, see arrow 2, occurs after 2 cycles during transition from up to downslope flow and a peak in available potential energy. During this cycle, there is a single peak of TKE with shear production playing an important role aided by the convective instability that occurs during flow reversal from upslope to downslope flow. The next peak of TKE occurs after 3 cycles at approximately t = 11.5 T. Later, during cycle 14, there are *two* peaks in TKE: peak 5 occurs at a similar downslope flow phase as the earlier peaks while the second peak (arrow 6) occurs shortly after flow reversal from downslope to upslope motion when there is a peak in APE (arrow 7). The different phasing of TKE in the near-critical case occurs because the interaction between the incident and reflected wave becomes important in this situation. Due to this interaction, the wave field gets weaker periodically as evident from the small velocity peaks and little turbulence between cycles 9-11 in figure 2.8(b). Mean flows with little temporal variability are found during this quiescent period with little turbulence when the near-boundary wave field is weak. However, there are strong down and upslope flow every 3 cycles (for example at t=8-8.5T, 11-11.5T and 14-14.5T) and correspondingly strong turbulence bursts during these periods.

Figure 2.9 shows the comparison of TKE contours during times with turbulence after quasi-steady state has been reached. Critical slope reflection results in one turbulence burst every wavelength and the burst occurs close to the wall as shown in figure 2.9(a). Near-critical slope reflection results in two distinct patches of turbulence in a wavelength. The patch closer to the wall in figure 2.9(b) occurs during the transition from up to downslope flow and the second patch that is detached from the wall occurs during the transition from down to upslope flow.

Figure 2.10 shows the time evolution of production, dissipation and buoyancy flux averaged in the slope-normal direction for critical and near-critical slope

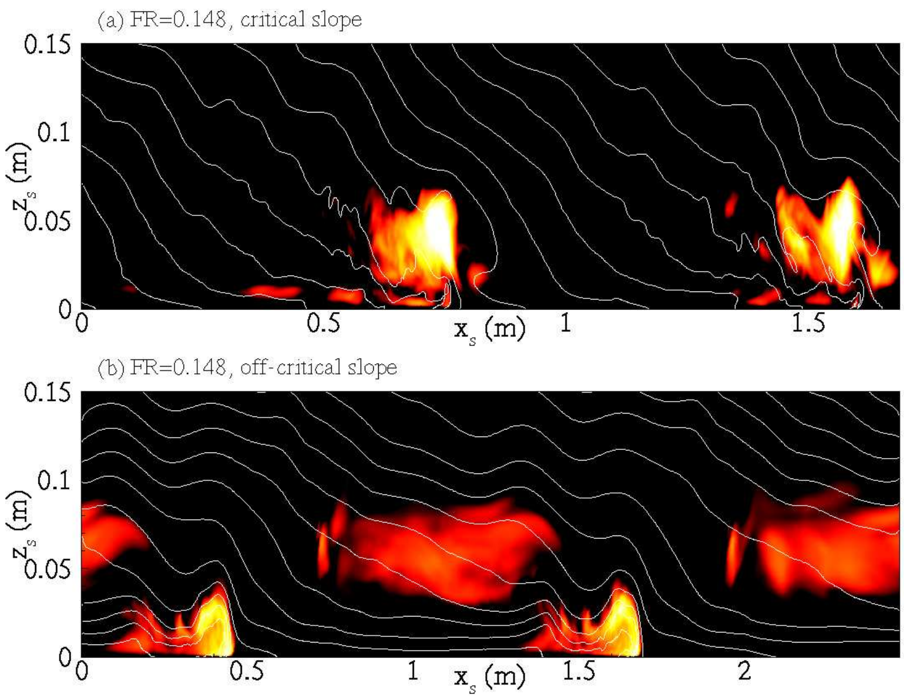

Figure 2.9: Spatial contours of turbulent kinetic energy at a quasi-steady state: (a) Case FR6S15, with critical slope angle $\beta = 15°$ and $Fr = 0.148$, is shown at $t = 9.1T$, (b) Case FR6S5 with near-critical slope angle, $\beta = 5°$ and $Fr = 0.148$, is shown at $t = 20.8T$.

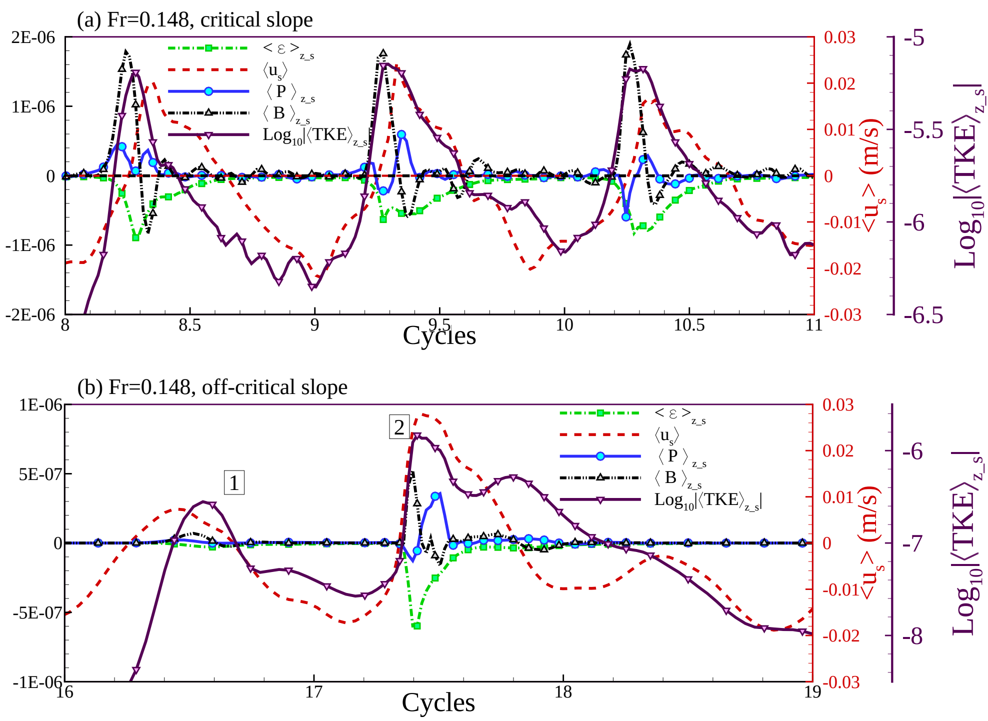

Figure 2.10: Comparison of terms in the TKE budget between critical and near-critical cases. Time evolution of production, dissipation and buoyancy flux averaged along slope-normal direction at mid-slope. Red colored dashed line is the along-slope velocity (averaged over 10 points near the maximum velocity location): (a) Case FR6S15 with critical slope angle $\beta = 15°$ and $Fr = 0.148$, (b) Case FR6S5 with near-critical slope angle, $\beta = 5°$ and $Fr = 0.148$.

angles. The difference observed between critical and near-critical slope cases is that, for critical slope reflection, the peak of buoyancy flux is dominant when compared with the peak of turbulent production, whereas during near-critical slope reflection, both buoyancy flux and production are significant contributors to the increase in the turbulent kinetic energy. Figure 2.10(a), corresponding to the critical slope case, exhibits a positive peak in the averaged buoyancy flux at 8.2T when the near-bottom flow reverses from down to upslope flow. There is some inter-cycle variability: the magnitude of the buoyancy flux peak changes during the subsequent cycles(not shown here). Negative production, which is unusual in turbulent flows, is seen after the positive peak in buoyancy flux. The mechanism of the negative production in the context of internal tide generation has been shown by Gayen & Sarkar (2011d) to be related to shear acting on turbulence structures initiated by buoyancy, a mechanism that is also operative here. For near-critical slope reflection with off-criticality 10°, a period with turbulence peaks is shown in figure 2.10(b). The primary peak marked by (2) is associated with both positive buoyancy flux and shear production. There is an auxiliary peak marked by (1) which occurs because of turbulence advection.

2.5 Mean Kinetic Energy

Turbulent dynamics has been discussed extensively in the previous section. The impact of turbulence on the mean flow is discussed in this section by making use of the mean kinetic energy equation.

The mean kinetic energy $m.k.e = (\langle u_i \rangle_y \langle u_i \rangle_y)/2$ evolves as

$$\frac{\partial(m.k.e)}{\partial t} + \langle u_j \rangle_y \frac{\partial(m.k.e)}{\partial x_j} = -P - \bar{\epsilon} + \bar{B} - \frac{\partial T_j}{\partial x_i}, \tag{2.16}$$

where $P = -\langle u_i' u_j' \rangle_y \langle S_{ij} \rangle_y$, $\bar{\epsilon} = \nu \frac{\partial \langle u_i \rangle_y}{\partial x_j} \frac{\partial \langle u_i \rangle_y}{\partial x_j}$, $\bar{B} = -\frac{g}{\rho_0} \langle \rho^* \rangle_y \langle w \rangle_y$, $T_i j = \langle p^*/\rho_0 \rangle_y \langle u_j \rangle_y - 2\nu \langle u_i \rangle_y S_{ij} + \langle u_i' u_j' \rangle_y \langle u_i \rangle_y$. Here P is production, $\bar{\epsilon}$ is the viscous dissipation rate of the mean velocity, $\bar{B}$ is the mean buoyancy flux with $\langle w \rangle_y$ denoting the mean vertical velocity, $\frac{\partial T_i}{\partial x_j}$ is the transport of mean kinetic energy with $S_{ij} = \frac{1}{2}(\frac{\partial \langle u_i \rangle_y}{\partial x_j} + \frac{\partial \langle u_j \rangle_y}{\partial x_i})$. The above equation is integrated in slope-normal direction

Table 2.4: Ratio of integrated production, mean dissipation, mean buoyancy to the input energy flux, $\mathbb{I}$. The energy input is transferred to turbulent kinetic energy through $\mathbb{P}$, to mean potential energy through $-\mathbb{B}$, and dissipated by viscosity through $\mathbb{D}$ and the remaining energy represented by $\mathbb{A}$ is the flux advected out of the domain.

	$\mathbb{P}/\mathbb{I}$	$\mathbb{D}/\mathbb{I}$	$-\mathbb{B}/\mathbb{I}$	$\mathbb{A}/\mathbb{I}$
$FR6S15$	0.06	0.51	0.42	0.005
$FR6S5$	0.035	0.44	0.48	0.04
$FR4S10$	0.03	0.51	0.42	0.03

and time, e.g., the integrated advection is

$$\langle A \rangle_{zt} = \int_0^{z_1} \int_{t_1}^{t_2} A \, dt \, dz_s, \tag{2.17}$$

where $z_1 = 1.5m$, t_1 and t_2 are chosen such that at least 4 wave periods are included in the quasi-steady state.

Let the integrated unsteady (or tendency) term in Eq. (2.16) be denoted by $\mathbb{U}$, advection term be denoted by $\mathbb{A}$, transport term by $\mathbb{T}$, production term by $\mathbb{P}$, dissipation term by $\mathbb{D}$, and buoyancy term by $\mathbb{B}$. After the reflected wave is established, the integrated values of advection and tendency are found to be approximately zero. Among the transport terms, the dominant contributor is the velocity-pressure correlation (internal wave flux). The value of the internal wave flux at $z_s = 1.5m$ is considered to be the input energy flux, $\mathbb{I}$, to the system that drives the near-boundary flow. The input, $\mathbb{I}$, is as follows:

$$\mathbb{I} = \int_0^{l_x} \left[\langle p^* \rangle \langle w_s \rangle \right]_{z_s=1.5} \, dx_s. \tag{2.18}$$

This input energy flux is accessible for conversion to mean buoyancy, conversion to turbulence through production, and destruction through viscous effects. The production term, $\mathbb{P}$, is usually positive resulting in the gain of turbulent kinetic energy at the expense of a loss of mean kinetic energy. The mean buoyancy term is the work done by gravity on the mean vertical motion. Negative mean buoyancy term indicates a transfer to mean potential energy. The input flux, $\mathbb{I}$, computed at

$z_s = 1.5$ has two components: (i) the wave field generated at the forcing region that travels towards the boundary, and (ii) the reflected wave field. The contribution of the reflected wave can be estimated by calculating the wave flux at a section above the wave forcing region and below the sponge region. It negligibly small in the exactly critical case FR6S15. However, in off-critical case FR6S5, since the reflected waves move away from the boundary, the radiated flux is significant ($\approx 10\%$ of the total incoming flux).

Three different cases (FR6S15, FR6S5, FR4S10) are examined to assess the role of different terms in the mean kinetic energy equation. Table 2.4 lists various terms in the mean kinetic energy equation. The mean dissipation, $\mathbb{D}$, and the transfer to mean potential energy through $\mathbb{B}$ balance the input wave flux. For critical reflection, 89 % of the total mean dissipation occurs in the boundary region, i.e., $0 < z_s < 0.15m$, and remaining occurs outside the boundary layer. For the off-critical case FR6S5, 82 % of the total mean dissipation occurs in the boundary region. Mean dissipation is high in all the cases because of the relatively weak incident wave and low value of Stokes Reynolds number, $Re_s = \frac{U_0 \delta_s}{\nu}$, where $\delta_s = \sqrt{2\nu/\Omega}$ is the Stokes boundary-layer thickness. The value of $Re_s = 20.8$ for cases FR6S15, FR6S5 and $Re_s = 10.22$ for the case FR4S10. We emphasize that a typical Stokes boundary layer on a non-sloping bottom is laminar at these values of Re_s. It is the phenomenon of wave intensification and breaking associated with critical slope dynamics that results in turbulence in the present simulations, albeit at a Reynolds number much lower than in the ocean.

2.6 Parametric dependence of turbulence statistics

DNS results at various Froude numbers for every slope angle considered in our simulations are collected to characterize the TKE dependence on Froude number and off-criticality.

Figure 2.11 shows averaged turbulent kinetic energy, $\langle K \rangle_{zt}$, and averaged turbulent dissipation rate, $\langle \epsilon \rangle_{zt}$, at $Fr = 0.074$ and 0.148 as a function of off-

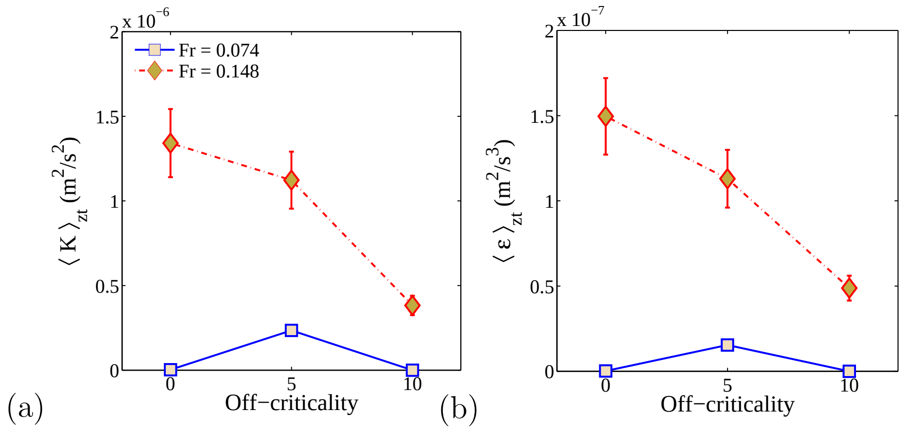

Figure 2.11: Cycle-averaged turbulent statistics at a mid-slope location and spatially averaged over a 0.25 m high boundary region are plotted as a function of off-criticality (degrees) in slope angle: (a) Turbulent kinetic energy, (b) Turbulent dissipation rate. The $\langle K \rangle_{zt}$ and $\langle \epsilon \rangle_{zt}$ values at $Fr = 0.074$ are *multiplied by a factor of 2* to accomodate all the results into the figure.

Table 2.5: Wall shear stress normalized with incoming wave along slope amplitude,averaged over 10 cycles at a mid-slope location.

	Fr	$0°$	$5°$	$10°$
$\tau_{w,avg}$	0.148	0.1815	0.1406	0.1325

criticality defined as the difference between internal wave angle ($\alpha = 15°$) and the slope angle (β) of the case in question. Thus, off-criticality of $0°$ corresponds to an exactly critical slope, while $10°$ off-criticality corresponds to a slope angle of $5°$. At a low $Fr = 0.074$, the critical case is not turbulent, and the values of $\langle K \rangle_{zt}$ and $\langle \epsilon \rangle_{zt}$ are maximum when the off-criticality angle is $5°$ and then they drop. For the larger incoming wave amplitude of the $Fr = 0.148$ series of simulations, $\langle K \rangle_{zt}$ and $\langle \epsilon \rangle_{zt}$ are maximum at critical slope reflection and then decreases monotonically as the off-criticality increases.

Table 2.5 shows the wall shear stress (normalized with ρU^2, where U is the amplitude of the incoming wave velocity in the along-slope direction), averaged over 10 cycles, recorded at mid-slope. The wall shear decreases with increasing off-criticality due to an increase in vertical length scale of the region of bottom turbulence.

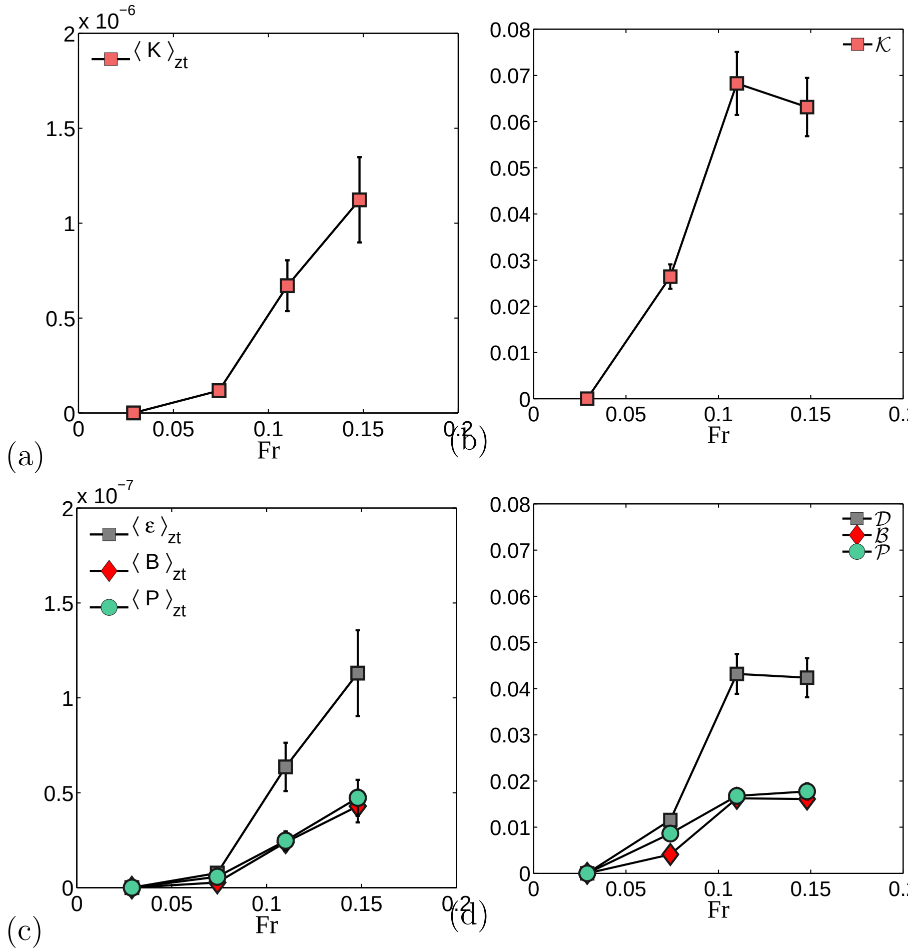

Figure 2.12: Turbulent statistics (cycle-averaged and spatially averaged over a 0.25 high boundary region at midslope) as a function of Froude number for a slope angle $\beta = 10°$: (a) averaged kinetic energy, (b) normalized kinetic energy, (c) averaged dissipation, buoyancy flux and production (d) normalized dissipation, buoyancy flux and production.

Normalized values of turbulent statistics are defined as follows,

$$\mathcal{K} = \frac{2\langle K\rangle_{zt}}{U_0^2 + W_0^2}, \qquad \mathcal{D} = \frac{2\langle \epsilon\rangle_{zt}}{\Omega(U_0^2 + W_0^2)}, \tag{2.19a}$$

$$\mathcal{B} = \frac{2\langle B\rangle_{zt}}{\Omega(U_0^2 + W_0^2)}, \qquad \mathcal{P} = \frac{2\langle P\rangle_{zt}}{\Omega(U_0^2 + W_0^2)}. \tag{2.19b}$$

For a near-critical slope angle, $\beta = 10°$, the effect of Fr on various turbulent statistics is assessed. Figure 2.12(a) shows averaged turbulent kinetic energy, $\langle K\rangle_{zt}$, and figure 2.12(b) shows normalized turbulent kinetic energy, plotted as a function of Froude number. Similarly, figures 2.12(c) and 2.12(d) show averaged and normalized values of terms in the TKE balance: dissipation, buoyancy flux and production, respectively. A rapid increase in averaged turbulent kinetic energy is found with increasing Fr. Upon normalization using the incoming wave amplitude, a natural velocity scale for the problem, the turbulent kinetic energy does not increase at the highest value of Fr. Terms on the r.h.s of the TKE equation, such as turbulent dissipation rate, also rapidly increase with increasing Fr. Guided by the finding here that turbulence occurs during only a fraction of the cycle and that this fraction eventually shows little dependence on the incoming wave amplitude, we take the scaling of the terms in the TKE transport equation to be $\Omega(U_0^2 + W_0^2)$. Fig. 2.12(d) shows that this normalization is able to substantially reduce the variation between cases at high Fr. An alternate normalization, based on $(U_0^2 + W_0^2)^{3/2}/\lambda$, was ruled out because it led to a systematic decrease with increasing Fr in the high-Fr regime.

2.7 Conclusions

The dynamics of internal waves reflected from a slope is examined as a function of incoming wave amplitude, measured by the wave Froude number, Fr, and the deviation of the slope angle, β, from the wave propagation angle, α. The choice of laboratory scale dimensions, e.g., the wave has a horizontal wavelength of $\lambda = 1.636$ m and a frequency of $\Omega = 0.15$ s^{-1}, allows the DNS approach that resolves turbulence, including the turbulent dissipation rate, without any additional models.

The effect of Fr at a near-critical slope angle is assessed. At zero Fr (no incoming wave), the numerical solution corresponds to a steady upslope streaming flow (Phillips (1970),Wunsch (1970)) with a balance between buoyancy and viscous drag. Near-critical reflection with an off-criticality angle $(\alpha-\beta)$ of 5° was examined for incoming waves with $0 < Fr < 0.148$. At low Fr, the internal wave response remains laminar. However, higher temporal frequencies, subharmonics and inter-harmonics are generated. During the initial transient, the near-bottom amplitude of the reflected wave increases and the near-bottom vertical wavelength decreases. The numerical solution in the laminar, low Fr cases agrees well with the analytical, inviscid solution derived by Scotti (2011) for critical and near-critical reflection except at the wall where there is a viscous boundary layer in the DNS. At a sufficiently high value of incoming wave amplitude (Fr), there is transition to turbulence.

The wave amplitude is also found to affect the functional dependence of the flow on slope angle. When Fr is small, the critical case is laminar and there is turbulence only in a narrow range of near-critical angles. At high Fr, there is turbulence at all the slope angles considered here.

The mechanism of transition to turbulence is investigated. It is found that, during the initial transient when the amplitude of the density variation in the internal wave increases, regions of static instability ($Ri_g < 0$) as well as shear instability ($Ri_g < 0.25$) are formed. The present nonlinear simulations show that it is wave breaking by the convective instability just after flow reversal from downslope to upslope that leads to turbulence during critical slope reflection similar to the result of Gayen & Sarkar (2011a) in the critical slope generation problem. In the case of near but not exactly critical reflection, transition to turbulence occurs at a different phase and arises due to both shear instability in upslope flow ($Ri_g < 0.25$ owing to wave shear) as well as convective instability during flow reversal from upslope to downslope. The inviscid analytical solution of Scotti (2011) was evaluated in a near-critical case and shows regions with static and shear instability, thus providing guidance as to the formation of turbulence. However, quantitative predictions of turbulence require fully nonlinear simulations. For instance, the first region of static instability occurs earlier in the analytical solution than in the simulations and, at later time, the statically unstable regions in the analytical solution are substantially larger than the turbulence patches in the simulations.

After the initial transient, a reflected wave field is established with periodic flow that has quasi-steady amplitude and phase-dependent turbulence. The phasing of turbulence is examined when the off-criticality angle, $\alpha - \beta$, varies between 0 and 10°. There are important differences between critical and near-critical cases. When the slope is critical, there is a single prominent peak of turbulent kinetic energy (TKE) per cycle that occurs just after flow reversal from down to upslope flow and is caused by positive buoyancy flux that occurs during the convective instability that accompanies the flow reversal event. The contribution of shear production to TKE is small. The phasing is similar when the off-criticality is 5°. In contrast, when the off-criticality has a larger value of 10°, turbulence is less regular and skips cycles. Both, buoyancy flux and shear production are found to be important contributors to the TKE in the near-critical case. The results in the various cases are collected to quantify the parametric dependence of TKE and turbulent dissipation rate (averaged over time and over distance above bottom) on slope angle and Froude number. Interestingly, it is found that reflection at near-critical angles can lead to more intense turbulence than critical slope reflection, for waves with small amplitude, that is, small Fr. The reason for this low Fr behavior is that, although the velocity intensification is smaller when the slope is offcritical, the convectively unstable region, not being restrained by the boundary, can be larger and thereby lead to stronger turbulence than the exactly critical case. At higher Fr, the values of TKE and turbulent dissipation rate exhibit a monotone decrease with increasing offcriticality.

At a given slope angle, the TKE and turbulent dissipation rate increase with increasing Fr. When normalized by incoming wave properties, the variability of turbulent statistics at high Fr decreases. In the present simulations, the maximum value of averaged TKE is approximately 7 % of the incoming wave kinetic energy,

K_{wave}, and the maximum value of averaged dissipation rate is approximately 5 % of ΩK_{wave}. If turbulent statistics, when appropriately normalized by wave characteristics, saturate with increasing Fr, parameterizations of wave dissipation for use in ocean models will be facilitated. Nevertheless, more work is necessary to establish if the results found in the present simulations holds under more general parametric variation as well as at geophysical scales.

2.8 Acknowledgements

Portions of this chapter were published in Journal of Fluid Mechanics (2013), coauthored by Dr. Gayen, Professor Alberto Scotti and Professor Sutanu Sarkar. V. K. Chalamalla, B. Gayen, A. Scotti & S. Sarkar (2013), Turbulence during the reflection of internal gravity waves at critical and near-critical slopes., *Journal of Fluid Mechanics*, *729*, 47–68.

Chapter 3

PSI in the case of internal wave reflected from an uniform slope

In the previous chapter, fully nonlinear three dimensional simulations of internal wave reflection were discussed. Subharmonic frequencies were found slightly away from the sloping bottom during off-critical reflection but not during exactly critical reflection. To study this phenomenon in detail, two dimensional numerical simulations of localized internal wave beam reflection on uniform slope are performed with a focus on parametric subharmonic instability (PSI).

3.1 Introduction

Internal tides are oceanic internal gravity waves that are generated by the flow of an oscillating tidal flow over bottom topography in the presence of density stratification. Some of the internal tide energy is dissipated locally due to small scale turbulence, while a substantial fraction is radiated out. The radiated tidal energy is thought to make a significant contribution to mixing in the ocean interior (Polzin *et al.*, 1997*a*; Munk & Wunsch, 1998; Ledwell *et al.*, 2000; Wunsch & Ferrari, 2004). One of the mechanisms by which internal tides dissipate energy is through reflection at a continental slope or at isolated topography. Two factors which work in conjunction to make the reflection process an important contributor to the transition from internal tides to turbulence are: (1) Continental slopes have substantial regions where the slope angle β is close to the critical angle for the semidiurnal internal tide (Cacchione *et al.*, 2002), and (2) Near-critical reflection leads to higher wave number and velocity amplitude for the reflected wave, enhancing the propensity for nonlinear effects.

When an internal wave reflects off a near-critical sloping bottom, the component of reflected wave number in the direction normal to the slope increases. When the slope angle β is close to the internal wave characteristic angle α (the situation of critical angle), the energy density of the reflected wave increases leading to high shear and small scale turbulence. This process has been studied theoretically in the frequency domain when $\beta \simeq \alpha$ (Dauxois & Young, 1999; Scotti, 2011). There have been several numerical and experimental studies (DeSilva *et al.*, 1997; Slinn & Riley, 1998*a*,*b*; Javam *et al.*, 1999; Tabaei *et al.*, 2005; Rodenborn *et al.*, 2011; Chalamalla *et al.*, 2013) exploring the reflection of internal gravity waves. Both shear-driven as well as convective-driven instabilities are found responsible for breakdown from waves to small scale turbulence. Off-critical reflection as a mechanism for nonlinear processes and turbulence has been less studied. In a study of nonlinear effects in reflecting and colliding wave beams by Tabaei *et al.* (2005), secondary waves with frequencies equal to the sum and difference of the participating wave beams are found. Chalamalla *et al.* (2013) found that, when the slope is near- but not exactly critical, wave breaking by larger overturns that are less restrained by the boundary is possible leading to higher turbulence levels than in the exactly critical case. The objective of the present study is to explore a different mechanism called parametric subharmonic instability(PSI) by which energy can be transferred to smaller vertical scales through generation of subharmonic waves.

An internal wave of frequency Ω and wave vector $\mathbf{k}$, when subjected to parametric subharmonic instability (PSI) decays by transferring energy to two waves of lower frequency, such that $\mathbf{k} = \mathbf{k}_1 + \mathbf{k}_2$ and $\Omega = \Omega_1 + \Omega_2$. The subharmonic frequencies can be either equal, i.e., $\Omega_1 = \Omega_2 = 0.5\Omega$ or unequal, depending on the flow conditions. A finite-amplitude free internal wave is susceptible to PSI through second-order interactions with infinitesimal perturbations as shown by theory (Hasselmann, 1967; Thorpe, 1968; McEwan, 1971), experiment (McEwan, 1971; Benielli & Sommeria, 1998) and numerical simulation (Koudella & Staquet, 2006).

There has been much recent interest in the role of PSI related to topographically generated internal tides. Transfer of energy from the internal tide to near-inertial motions with nearly half the fundamental frequency was predicted to be important at near critical latitude (29°N) in numerical simulations by MacKinnon & Winters (2005). Such transfer of energy at a modest rate was later observed in the ocean by MacKinnon *et al.* (2013). Carter & Gregg (2006) and, more recently, Sun & Pinkel (2013) have documented significant energy transfer from the semidiurnal tide to near-diurnal motions near Kaena Ridge.

Oceanic internal waves generated at steep topography with near-critical regions have high-mode content that often propagates as so-called internal wave beams. Laboratory and numerical experiments also show internal wave beams radiating off obstacles. The stability of internal wave beams of finite width is of interest. Wave beams have found to be susceptible to PSI during propagation as in the numerical simulations of generation at a continental shelf break (Gerkema *et al.*, 2006) and PSI may help explain the observed transfer of M2 to M1 energy in the vicinity of Kaena ridge. In laboratory experiments, Clark & Sutherland (2010) found that large-amplitude oscillation of a cylinder led to internal wave beams that break down after long time. Based on the experimental data and supporting numerical simulations, the breakdown was attributed to PSI. Recently, Bourget *et al.* (2013) experimentally found PSI of plane wave beams with frequency Ω that leads to subharmonics with frequencies 0.33Ω and 0.67Ω. Accompanying theoretical analysis of the stability of infinite-width sinusoidal plane waves helped elucidate how the division of subharmonic frequencies and their growth rates depends on frequency, wave number, and Reynolds number (Re) of the fundamental wave. In particular, the subharmonic frequencies were found to move towards 0.5Ω at large Re.

Interaction with the upper ocean pycnocline results in beam degradation according to observational studies (Cole *et al.*, 2009; Johnston *et al.*, 2010). Gayen

& Sarkar (2013) performed several two-dimensional simulations of an internal wave beam of vertical thickness, l_b, incident on a pycnocline of vertical thickness, l_p, and found that the refracted beam suffers PSI as long as l_p was sufficiently large to support the propagation of a vertical wavelength of the resulting subharmonic wave. Increasing the beam Re shifted the subharmonic frequencies from (0.3, 0.7) to approximately 0.5 in agreement with the analysis of Bourget *et al.* (2013). There was also a finite-amplitude threshold: PSI was absent when the beam velocity was decreased, i.e., the *incident* beam Froude number, $Fr_b = u/Nl_b$, was decreased from 0.035 to 0.015. In a followup three-dimensional study (Gayen & Sarkar, 2014), the cascade of energy through PSI to ultimately turbulence was demonstrated. Similar to observations, the simulation showed substantial degradation of the beam so that the main reflected wave carried only 30% of the incident energy. Javam *et al.* (2000) found PSI in a study of caustic reflection ($\omega = N$) in their two-dimensional numerical experiments. For sufficiently large values of incident wave Keulegan number (degree of non-linearity), internal waves with frequencies 0.3Ω and 0.7Ω were excited in the reflection region. Zhou & Diamessis (2013) studied the reflection of an internal wave beam at a free-slip horizontal surface finding nonlinear effects such as mean currents and harmonics. In addition, PSI was found at long time in the subsurface reflected zone.

Recent work has examined the conditions under which the spatially-localized internal wave field of a beam becomes unstable to PSI. Karimi & Akylas (2014) performed an asymptotic analysis for a small-amplitude beam subject to short (relative to the beam width) wavelength instability. It was found that quasi-monochromatic carrier waves that are sinusoidal with a localization envelope can suffer PSI, and an expression for the instability growth rate was derived. Thresholds in both the beam width (number of carrier wave lengths) and beam velocity were identified. Bourget *et al.* (2014) also recently examined the role of finite beam width. Their laboratory and numerical experiments showed that beam width and beam amplitude must be sufficiently large for the onset of PSI. An energy-based analysis of the wave-wave interaction helped explain the observed thresholds. As noted by Karimi & Akylas (2014) and Bourget *et al.* (2014), thresholds for PSI in beams are present because both the time of interaction (crossing time of a subharmonic wave packet across the beam envelope) and the strength of the quadratic interaction term must be sufficiently large to overcome viscous decay of the subharmonic.

Reflection of an internal wave beam at a solid boundary with slope angle β close to the wave propagation angle α substantially increases the wave amplitude and the wave number. It is thus possible that an incident internal wave beam of small amplitude that is stable, upon reflection at the solid boundary, leads to a reflected wave beam that is unstable to PSI. We examine this possibility through two-dimensional numerical simulations. The roles of wave amplitude, envelope shape, beam width, and Reynolds number are explored and connected with previous results on the stability of localized internal waves. The subsequent evolution of the subharmonic waves (and their energetics) is the focus of this paper. Section 2 of this paper describes the problem setup; section 3 describes the evolution of PSI; section 4 presents results on the energetics of subharmonic waves; finally, a summary and concluding remarks are given in section 5.

3.2 Formulation of the problem

Navier-Stokes equations under the Boussinesq approximation, and in a non-rotating environment are solved. Internal waves are forced by adding a momentum source to the right hand side of the vertical velocity equation. The governing equations are shown below:

$$\nabla \cdot \mathbf{u} = 0, \tag{3.1a}$$

$$\frac{Du}{Dt} = -\frac{\partial p^*}{\partial x} + \nu \nabla^2 u, \tag{3.1b}$$

$$\frac{Dw}{Dt} = -\frac{\partial p^*}{\partial z} - \frac{g\rho^*}{\rho_0} + \nu \nabla^2 w + A_0 sin(\Omega t) f(x,z), \tag{3.1c}$$

$$\frac{D\rho^*}{Dt} = \kappa \nabla^2 \rho^* - w\frac{d\rho^b}{dz}. \tag{3.1d}$$

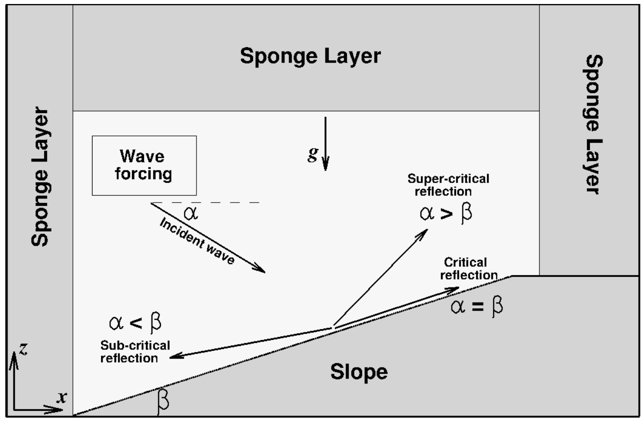

Figure 3.1: Schematic of the problem showing a uniform slope of angle β and an incident wave that propagates at an angle α to the horizontal. The reflected wave is also shown for three different scenarios of incident wave angle relative to slope angle: (1) Exactly critical reflection when $\alpha = \beta$, (2) Supercritical reflection when $\alpha > \beta$ and (3) Subcritical reflection when $\alpha < \beta$. The wave angle with respect to the vertical is preserved after reflection in all three cases.

Here, $d\rho^b/dz$ is the background density gradient.

The forcing term f(x,z) is applied far away from the sloping boundary (see schematic in figure 3.1) to produce a localized internal wave beam that travels towards the sloping boundary. Two choices are used for the forcing resulting in cross-beam profiles shown in figure 3.2. Although both profiles have the same carrier wave wavelength and similar widths, the shape of the modulation envelope is different: (a) top-hat with a constant amplitude that has a sharp cutoff to zero outside the beam, and (b) Gaussian. The forcing functions are as follows:

Top-hat

$$f(x,z) = \begin{cases} \cos k_{x,i}(x - x_0) \exp(-b_t |k_{x,i}(z - z_0)|^3) & \text{if } k_{x,i}|x - x_0| < n\pi, \\ 0. & \text{otherwise} \end{cases} \tag{3.2}$$

Gaussian

$$f(x,z) = \cos k_{\sigma,i}(\sigma - \sigma_0)\exp(-20b_g(\sigma-\sigma_0)^2)\exp(-b_g(r-r_0)^2). \tag{3.3}$$

In (3.2) for the top-hat forcing that is centered around (x_0, z_0), $k_{x,i}$ is the horizontal wave number of the carrier wave, the cubic-exponential function of z with parameter b_t localizes the forcing region to a small vertical region, and n sets the the number of carrier wavelengths in the beam. The forcing, (3.3), has a Gaussian localization of the envelope in both the along-beam coordinate, $r = x\cos\alpha - z\sin\alpha$, and the across-beam coordinate, $\sigma = x\sin\alpha + z\cos\alpha$, and a carrier wave cross-beam wavenumber $k_{\sigma_i} = \sqrt{({k_{x,i}}^2 + {k_{z,i}}^2)}$. The parameter, b_g, is chosen such that the width of the Gaussian beam is the same as the width of the top-hat beam.

The nondimensional parameters that govern the flow are Reynolds number Re_i, incoming wave Froude number Fr_i, ${N_\infty}^2/\Omega^2$ and Prandtl number Pr, defined as follows:

$$Re_i = \frac{u_i}{\nu k_{x,i}}, \quad Fr_i = \frac{u_i k_{x,i}}{\Omega}, \quad \frac{{N_\infty}^2}{\Omega^2} = -\frac{g}{\rho_0\Omega^2}\frac{d\rho^b}{dz}, \quad Pr = \frac{\nu}{\kappa}. \tag{3.4}$$

The Froude number $Fr_i = u_i k_{x,i}/\Omega$ as defined here measures the distance of wave self-advection relative to the wavelength, or fluid velocity relative to wave velocity and thus the nonlinearity of the incoming wave.

The governing equations (3.1) are written in generalized curvilinear coordinates and solved on an body conforming grid. A mixed finite difference/spectral discretization, a third-order Runge-Kutta-Wray time advancement, a fractional step method for the Navier-Stokes equations, and a multigrid Poisson solver for the pressure are employed. The numerical algorithm is described by Gayen & Sarkar (2011*b*). The top, left and right boundaries have Rayleigh damping (sponge layer) to absorb the internal wave energy away from the region of interest. The velocity and scalar fields are relaxed towards the background state in the sponge region by adding damping functions -$\sigma(x,z)\,[(u,w)]$ and $-\sigma(x,z)\,[\rho^*]$ to the right hand side

Table 3.1: Properties of the imposed incident wave (subscript i) and the resultant reflected wave (subscript r). The beam amplitude, u_i, is varied in series SUP1 (top-hat beam) and series SUP2 (Gaussian beam). All other cases have top-hat beam profiles. The background stratification is $N_\infty = \Omega/sin(\alpha)$, the kinematic viscosity is $\nu = 10^{-6}$ m^2/s and the Prandtl number is $Pr = 1$.

Case	$u_i(m/s)$	α	β	$\Omega(rads^{-1})$	$k_{x,i}(m^{-1})$	w	Fr_i	Re_i	Fr_r	$Fr_{r,th}$	PSI
Top-hat											
SUP1a	0.9×10^{-3}	18°	10°	0.1	1.7	$1.5\lambda_x$	0.015	529	0.15	0.17	No
SUP1b	1.8×10^{-3}	18°	10°	0.1	1.7	$1.5\lambda_x$	0.03	1059	0.30	0.35	Yes
SUP1c	2.7×10^{-3}	18°	10°	0.1	1.7	$1.5\lambda_x$	0.046	1588	0.42	0.52	Yes
SUP1d	3.6×10^{-3}	18°	10°	0.1	1.7	$1.5\lambda_x$	0.061	2118	0.53	0.7	Yes
SUP1e	4.5×10^{-3}	18°	10°	0.1	1.7	$1.5\lambda_x$	0.076	2647	0.62	0.87	Yes
SUP1f	5.4×10^{-3}	18°	10°	0.1	1.7	$1.5\lambda_x$	0.092	3176	0.7	1.0	Yes
Gaussian											
SUP2a	1.8×10^{-3}	18°	10°	0.1	1.7	$1.5\lambda_x$	0.03	1059	0.25	-	No
SUP2b	2.7×10^{-3}	18°	10°	0.1	1.7	$1.5\lambda_x$	0.046	1588	0.36	-	Yes
SUP2c	3.6×10^{-3}	18°	10°	0.1	1.7	$1.5\lambda_x$	0.061	2118	0.46	-	Yes
SUP2d	4.5×10^{-3}	18°	10°	0.1	1.7	$1.5\lambda_x$	0.076	2647	0.54	-	Yes
SUP2e	5.4×10^{-3}	18°	10°	0.1	1.7	$1.5\lambda_x$	0.092	3176	0.62	-	Yes
SUP2f	6.5×10^{-3}	18°	10°	0.1	1.7	$1.5\lambda_x$	0.11	3823	0.7	-	Yes
SUP3	1.8×10^{-3}	18°	10°	0.1	1.7	$3.0\lambda_x$	0.03	1059	0.26	0.35	Yes
SUP4	1.8×10^{-3}	18°	6°	0.1	1.7	$3.0\lambda_x$	0.03	1059	0.1	0.12	No

(a) **Supercritical reflection**

Case	$u(m/s)$	α	β	$\Omega(rads^{-1})$	$k_x(m^{-1})$	w	Fr	Re	PSI
F1	4.5×10^{-3}	18°	-	0.1	5.73	$3\lambda_x$	0.26	785	Yes

(b) **Freely propagating wave**

Case	$u_i(m/s)$	α	β	$\Omega(rads^{-1})$	$k_{x,i}(m^{-1})$	w	Fr_i	Re_i	Fr_r	$Fr_{r,th}$	PSI
C5	4.5×10^{-3}	10°	10°	0.1	1.7	$1.5\lambda_x$	0.076	2647	-	∞	No

(c) **Critical reflection**

Case	$u_i(m/s)$	α	β	$\Omega(rads^{-1})$	$k_{x,i}(m^{-1})$	w	Fr_i	Re_i	Fr_r	$Fr_{r,th}$	PSI
SUP6	2×10^{-2}	18°	8.88°	0.1	0.34	$1.5\lambda_x$	0.070	58823	0.44	0.55	Yes
SUP7	6×10^{-4}	7°	3.49°	0.0001407	0.034	$1.5\lambda_x$	0.14	17647	0.45	1.2	Yes
SUB8	6×10^{-4}	7°	10.5°	0.0001407	0.034	$1.5\lambda_x$	0.14	17647	0.46	3.5	Yes

(d) **High Reynolds number**

Table 3.2: Domain size and grid parameters for the simulated cases. All dimensions are in meters.

Case	N_x	N_z	L_x	L_z	$\Delta_{x,min}$	$\Delta_{z,min}$
SUP1a-1f	769	385	50.0	15.0	0.02	0.0043
SUP2a-2f	769	385	50.0	15.0	0.02	0.0043
SUP3	769	385	50.0	15.0	0.02	0.0043
SUP4	769	385	50.0	15.0	0.02	0.0043
F1	769	385	30.0	11.0	0.011	0.008
C5	769	385	50.0	15.0	0.02	0.0043
SUP6	1153	769	400.0	75.0	0.099	0.0043
SUP7	1153	769	2000.0	400.0	0.58	0.067
SUB8	1153	769	2200.0	450.0	0.63	0.053

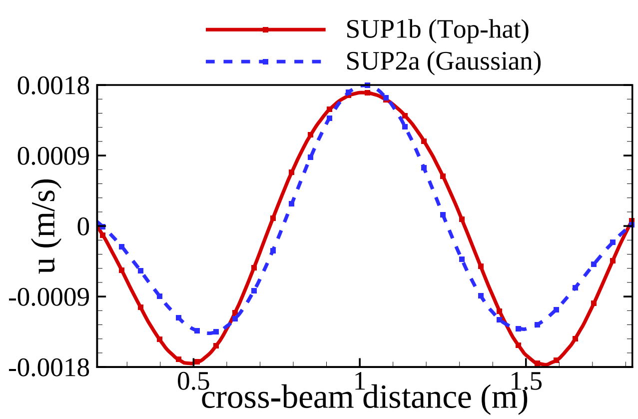

Figure 3.2: Cross-beam horizontal velocity profile is shown for cases SUP1b (top-hat beam) and SUP2a (Gaussian beam). The forcing parameters are chosen such that the beam width remains the same for Gaussian and top-hat beam profiles.

of the momentum and scalar equations, respectively. Variable time stepping with a fixed CFL number of 0.8 is used. No slip boundary conditions are imposed at the sloping bottom for u, w and no flux boundary condition for the density field.

A total of nineteen simulations are performed in this study as shown in table 3.1. Cases SUP1a-1f (top-hat beam), SUP2a-2f (Gaussian beam) concern *supercritical* reflection, $\alpha > \beta$. The six cases in series SUP1 and six cases in series SUP2 have fixed internal wave angle $\alpha = 18°$ and fixed slope angle $\beta = 10°$, while the incoming wave amplitude (wave Froude number) varies. Case SUP3 with a larger beam width $w = 3\lambda_x$, relative to case SUP1b, is simulated to examine if beam width changes the growth rate of subharmonic modes. To study the effect of off-criticality $(\alpha - \beta)$, SUP4 has been simulated with a shallow slope angle of $\beta = 6°$ so that the off-criticality $(|\alpha - \beta|)$ increases to 12°, while all the other parameters remain identical to case SUP3. The parameter which is modified from its preceding case has been highlighted with gray shading in table 3.1. Case F1 is the simulation of a wave beam having the same characteristics as the reflected wave of case SUP3 that is allowed to propagate freely in the absence of a sloping boundary. Case C5 considers exactly critical reflection with $\alpha = \beta = 10°$ and $Fr_i = 0.076$. SUP6 is a supercritical reflection case at high Reynolds number. Finally, to study reflection under oceanic conditions where wave angles are shallower, SUP7 (supercritical reflection, $\alpha > \beta$) and SUB8 (subcritical reflection, $\alpha < \beta$) are considered with a shallower internal wave angle of 7° and frequency corresponding to the M2 internal tide $\Omega = 0.0001407$ (rad/s). In cases SUP6 and SUP7, the slope angle β has been chosen such that $\sin(\beta) = 0.5 \sin(\alpha)$ and the reason for choosing this slope angle will be explained in the subsequent sections. All cases have a minimum vertical resolution $\Delta z_{min} < \delta_s$, where $\delta_s = \sqrt{2\nu/\Omega}$ is the Stokes boundary layer thickness. The smallest vertical wavelength in the instability corresponding to the subharmonic with the shallowest wave angle, e.g. 0.16 m in case SUP1e, is also well resolved by the grid.

3.3 Results

Simulations start with the generation of waves near the forcing region that travel towards the slope. These incident waves impinge on the slope and reflect forward when $\alpha > \beta$ or backward when $\alpha < \beta$. With decreasing off-criticality angle $(\alpha - \beta)$, the reflected wave beam has increasing energy density associated with velocity intensification and wavelength reduction after reflection. Linear theory predicts that the Froude number changes upon reflection according to

$$Fr_{r,th} = Fr_i \left[\frac{\sin(\alpha + \beta)}{\sin(|\alpha - \beta|)} \right]^2 . \tag{3.5}$$

Table 3.1 shows that the reflected beam Froude number, Fr_r, measured in the simulation increases by almost an order of magnitude for low Fr_i and agrees well with the theoretical prediction, $Fr_{r,th}$. However, at larger values of Fr_i, linear theory predictions are not accurate; e.g., Table 1 shows that, at $Fr_i = 0.092$ (SUP1f), the theoretical estimate is approximately 1.4 times the actual value of Fr_r.

At low values of incoming wave Froude number, the reflected wave beam remains stable. A new phenomenon found in this study is the *subharmonic instability* of the reflected wave beam when its Froude number Fr_r exceeds a value of approximately 0.3. Details about the instability of the reflected wave beam and the evolution of subharmonic wave energy are discussed in the subsequent sections. To calculate the wave numbers of reflected and subharmonic waves, a time series of horizontal and vertical line data is extracted and then band-passed around the frequency of interest. The slope of the band-passed space-time diagram gives the horizontal (vertical) phase speed and the horizontal(vertical) wave number is then calculated by $k_x = \omega/c_{p,x}$, $k_z = \omega/c_{p,z}$ where ω, $c_{p,x}$, $c_{p,z}$ are the frequency, horizontal and vertical phase speeds, respectively.

3.3.1 Evolution of subharmonic waves

Laboratory scale simulations

Figures 3.3(a)-(d) show contour plots of the horizontal velocity for case SUP1e. Figure 3.3(a) represents the initial stages of the reflection process with a

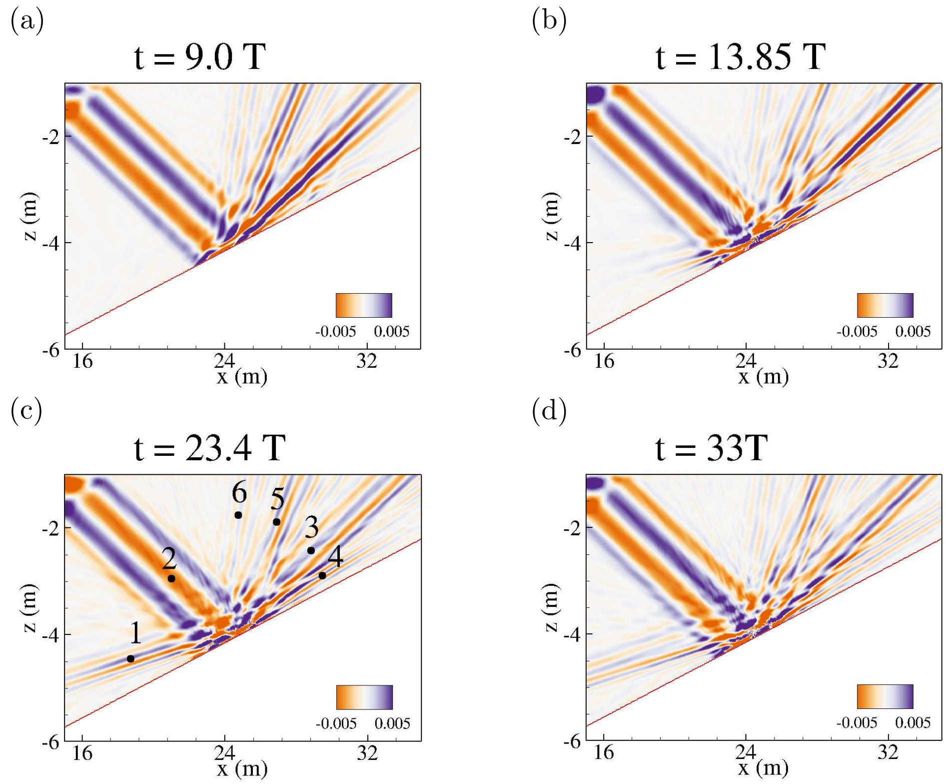

Figure 3.3: Case SUP1e. Contours of horizontal velocity u (m/s) at various time instances show the evolution of PSI. The incident beam travels from the upper left towards the slope.

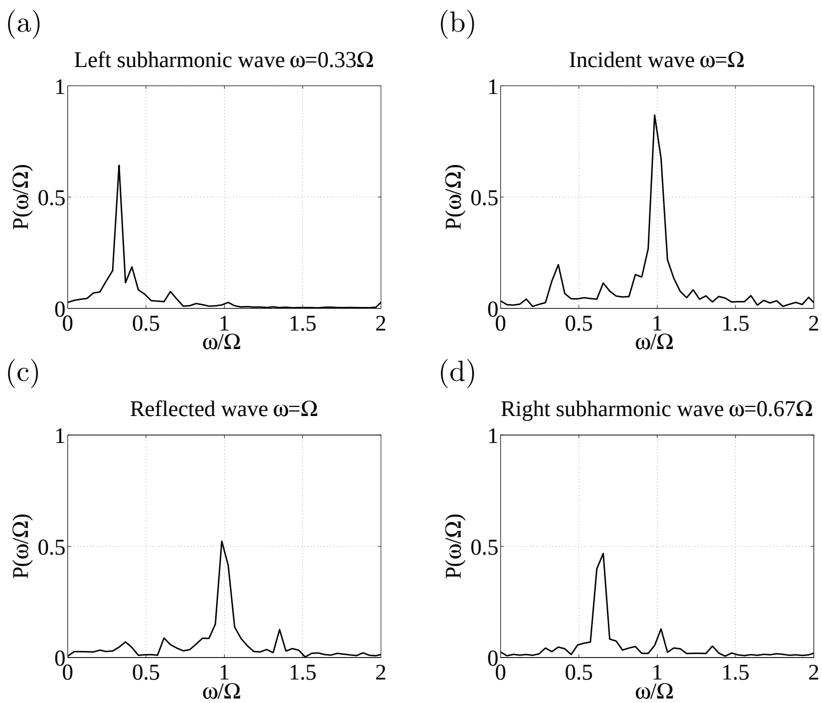

Figure 3.4: Case SUP1e. Frequency spectra of the horizontal velocity: (a) location 1 (left propagating subharmonic wave), (b) location 2 (incident wave), (c) location 3 (reflected wave), and (d) location 4 (right propagating subharmonic wave). (Locations in figure 3.3(c))

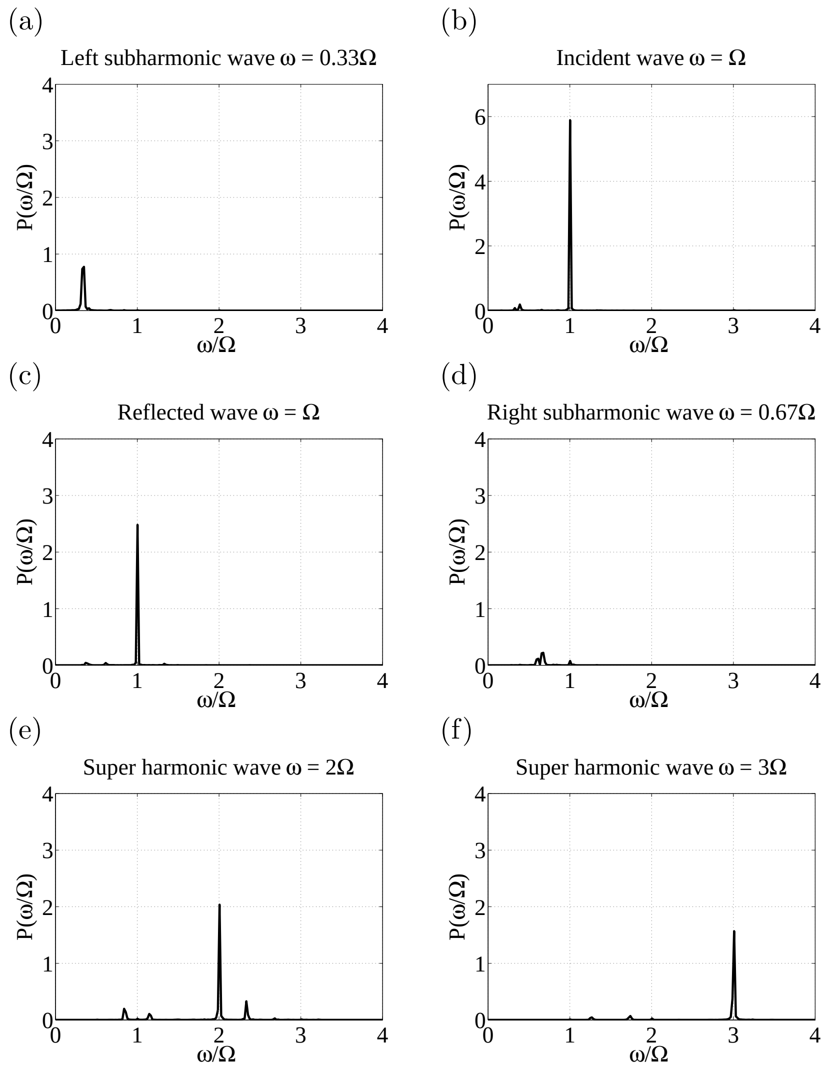

Figure 3.5: Kinetic energy spectra for case SUP1e compared among various locations: (a) location 1 (left propagating subharmonic wave), (b) location 2 (incident wave), (c) location 3 (reflected wave), (d) location 4 (right propagating subharmonic wave), (e) location 5 (superharmonic wave of frequency 2Ω), and (f) location 6 (superharmonic wave of frequency 3Ω). All these locations are shown in figure 3.3(c).

decreased wavelength and an increased velocity relative to the incident wave. The vertical wave number of the primary reflected wave ($k_{z,r} = 15.0$) is approximately 2.86 times higher compared to the incident wave ($k_{z,i} = 5.23$). Higher harmonics with $\omega = 2\Omega$ and 3Ω are also formed due to nonlinear interactions during the reflection. The second harmonic is evident as the steeper of two reflected beams in figure 3.3(a) while the even steeper third harmonic is more prominent in the vertical velocity field (not shown here).

At later time, two internal waves having shallower angles compared to the primary reflected wave emerge from the reflection region. One of them propagates to the left and the other towards the right. At t = 23.4T, these two waves are quite evident in the horizontal velocity field shown in 3.3(c). Since these waves have shallower angles, their footprint is weaker in the vertical velocity field (not shown here). Frequency spectra at four different locations 1-4 as specified in figure 3.3(c) are shown in figure 3.4. The left traveling subharmonic at location 1 has a peak at a frequency 0.33Ω and the right traveling subharmonic at location 4 has a peak at frequency 0.67Ω, as shown in figure 3.4. Both, location 2 (incident wave) and 3 (reflected wave) show a peak at the fundamental frequency Ω. Location 3 representing the reflected wave has additional peaks of substantial strength at the subharmonic frequencies (0.33Ω, 0.67Ω).

Frequencies of both the subharmonic waves add up to the primary wave frequency, satisfying one of the conditions of PSI. The wave numbers of the two subharmonic waves add up to that of the primary *reflected wave*, showing that it is the reflected wave and not the incident wave which undergoes the instability. For case SUP1e, the horizontal and vertical wave numbers of the subharmonic waves are shown in table 3.3. Both the subharmonic waves have smaller vertical wavelengths compared to the reflected wave. Figure 3.5 shows kinetic energy spectra at various locations 1-6 that were specified in figure 3.3(c). Location 2 which represents the incident wave has the highest peak value. Locations 5 and 6 which correspond to superharmonic frequencies also have significant energy with a level comparable to the primary reflected wave (location 3). Another important point to note here is that the left traveling subharmonic mode (location 1, 0.33Ω) has higher energy

Table 3.3: Case SUP1e. Horizontal and vertical wave numbers (m^{-1}) of the left and right subharmonic waves add up to the corresponding values of the incident wave.

$k_{x,left}$	$k_{x,right}$	$k_{x,r}$
-2.8 ± 0.3	7.8 ± 0.5	5.0 ± 0.3
$k_{z,left}$	$k_{z,right}$	$k_{z,r}$
24.0 ± 2.0	-39.0 ± 4.0	-15.0 ± 1.5

compared to the right traveling subharmonic mode (location 4, 0.67Ω).

Case C5, which corresponds to exactly critical reflection, does not show any sign of PSI. The geometry and the requirements of PSI (sum of daughter wave frequencies and wave numbers are equal to the corresponding values for the primary wave) combine to prevent the possibility of PSI after critical reflection. This is explained by figure 3.6 and its caption by considering all possible scenarios of subharmonic wave formation for a reflected wave in the critical angle case. Furthermore, the reflected beam becomes increasingly thinner as the slope angle approaches criticality. Although, the number of wavelengths does not change, the viscous boundary layer becomes increasingly important to the dynamics.

Increasing the beam width for a given value of incoming Froude number allows PSI to become stronger as predicted by Karimi & Akylas (2014). Case SUP3 with an incoming Froude number $Fr_i = 0.03$ and beam width $w = 3\lambda_x$ exhibits stronger PSI and higher subharmonic energy growth rate when compared to case SUP1b which has the same value of Fr_i and smaller beam width $w = 1.5\lambda_x$. Figure 3.7 is a comparison of horizontal velocity contours for cases SUP1b, SUP3 and SUP4 at time t = 51 wave cycles. The reflected waves in figures 3.7(a)-(b) show signs of PSI, however the amplitude of the subharmonics is larger when the beam width is $3\lambda_x$ (figure 3.7(b)) relative to $1.5\lambda_x$ (figure 3.7(a)).

The slope angle β affects the characteristics of the reflected wave and could thereby play a role in PSI, prompting an additional simulation, case SUP4. The incident wave properties of Case SUP4 are identical to case SUP3 but the slope has a shallower angle of $\beta = 6°$. There is no sign of PSI in case SUP4 over the simulation time of 56 wave cycles as can be inferred from Figure 3.7(c). According

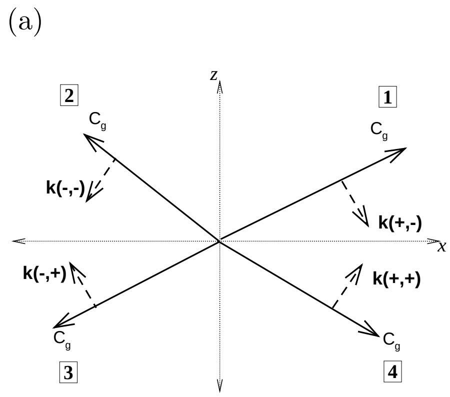

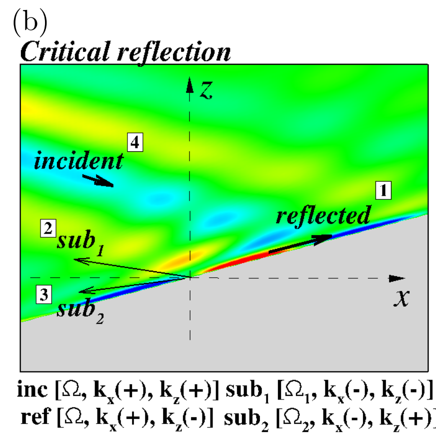

Figure 3.6: A wave undergoing critical reflection cannot undergo PSI. Panel (a) shows the four quadrants possible for the group velocity vector, $\mathbf{c}_g$, of internal waves that propagate outward from the origin. The corresponding wave number vector, $\mathbf{k}$, is also shown with a label where the first entry is the sign of the horizontal component, k_x, and the second is the sign of the vertical component, k_z. For example, a wave with $\mathbf{c}_g$ in the first quadrant has $k_x > 0$ and $k_z < 0$. Panel (b) shows contours of velocity, u, in the critical reflection (C5) case with energy propagation ($\mathbf{c}_g$) directions shown by arrows. The reflected wave propagates in the first quadrant, grazing along the slope. The subharmonic modes (Ω_1, Ω_2) must have *shallower* angle with respect to the horizontal than the reflected wave and, therefore, are constrained to the second and third quadrants as shown(sub_1, sub_2). However, $k_x < 0$ for both subharmonics, so that their sum *cannot* equal the $k_x > 0$ value of the reflected wave.

to linear theory, (3.5), the nonlinearity (Froude number) of the reflected wave decreases with an increase in the off-criticality ($\alpha - \beta$). Table 3.1 shows that the reflected wave has $Fr_r = 0.1$ in case SUP4 ($\alpha - \beta = 12°$) and $Fr_r = 0.26$ in case SUP3 ($\alpha - \beta = 8°$). Thus, in contrast to the unstable case SUP3, the amplitude of the reflected wave in case SUP4 is not sufficiently large for the wave to undergo PSI. Numerical simulation is *necessary* to accurately quantify the reflected wave characteristics. This is clear from Table 3.1 which shows that theory in the case of larger-Fr incoming beams overpredicts the reflected wave Fr substantially, by as much as 40% in case SUP1f. Nevertheless, it is of interest to examine if freely propagating beams can give insights into the PSI process. An additional simulation F1 (figure 3.8) is performed where an internal wave beam (having the same characteristics as the reflected wave of case SUP3) is generated and allowed to propagate freely in the absence of sloping boundary. Similar to the reflected wave in case SUP3, this freely propagating wave also undergoes PSI, bolstering our claim that the subharmonics found in the present reflection problem result from PSI of the reflected wave. Thus, the main role of reflection at the sloping boundary in terms of PSI could be to set the properties of the *reflected wave* such as wave number and amplitude and, thereby, the instability properties. It is however recognized that the reflection problem considered here has other elements, such as the viscous boundary layer, interaction of the propagating subharmonics with the incident, reflected and super harmonic waves, as well as the constraint of a solid boundary which would lead to quantitative differences with the free-beam problem.

In the scenario of supercritical internal wave reflection, given the constraints that wave numbers and frequencies of subharmonic modes should add up to the corresponding values of the primary wave, it is necessary that one of the subharmonic waves propagates in the first quadrant and the other propagates in the third quadrant. This combination was evident for the subharmonic waves of case SUP1e. The reflected wave in case SUP1e undergoes PSI to generate subharmonic waves of frequencies 0.33Ω and 0.67Ω in contrast to the classical example of both subharmonic modes having a frequency 0.5Ω. Equal division of frequencies among

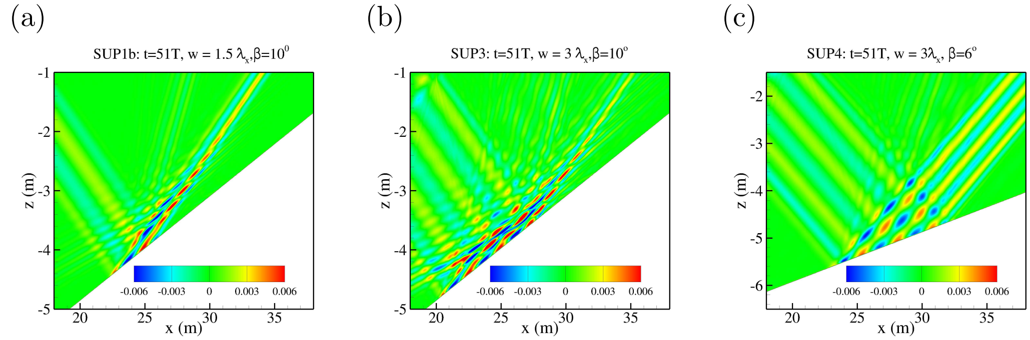

Figure 3.7: Contours of horizontal velocity u (m/s) for cases SUP1b (left), SUP3 (middle) and SUP4 (right) at time t = 51 T. Incident wave Froude number $Fr_i = 0.03$ is same for all three cases. Case SUP3 has twice the beam width of case SUP1b. All parameters are identical between cases SUP3 and SUP4, except the slope angle (SUP3: $\beta = 10°$, SUP4: $\beta = 6°$).

the subharmonic modes with $\omega = 0.5\Omega$ implies that each of the two subharmonics (one propagating in the first quadrant and the other in the third quadrant) makes the same angle $\alpha_{sub} = 0.5\sin(\alpha)$ with the horizontal. This imposes the following geometrical constraint on the slope angle: $\sin(\beta) = \sin(\alpha_{sub}) = 0.5\sin(\alpha)$. In other words, equality of subharmonic frequencies requires that the daughter waves graze the slope as they propagate away from the reflected wave. To evaluate this scenario, we have simulated case SUP6 with a slope angle that satisfies $\sin(\beta) = 0.5\sin(\alpha)$, and also chosen a higher Reynolds number. However, in spite of satisfying the slope angle constraint and allowing a higher Reynolds number, case SUP6 still shows subharmonic instability with unequal frequency division of 0.33Ω and 0.67Ω. It appears that the proximity of the wall hinders PSI with equal frequency division, perhaps because the wall boundary layer interferes with the formation of a resonant wavenumber triad involving slope-grazing subharmonics by imposing viscous oscillating boundary layer dynamics.

Large scale simulations

Two large scale simulations (cases SUP7 and SUB8) are performed with shallow internal wave angle $\alpha = 7°$ closer to oceanic conditions and a frequency corresponding to the M2 tide ($\Omega = 0.0001407$ rad/s). Rotation of the earth is not considered in these simulations for simplicity. Case SUP7 is supercritical

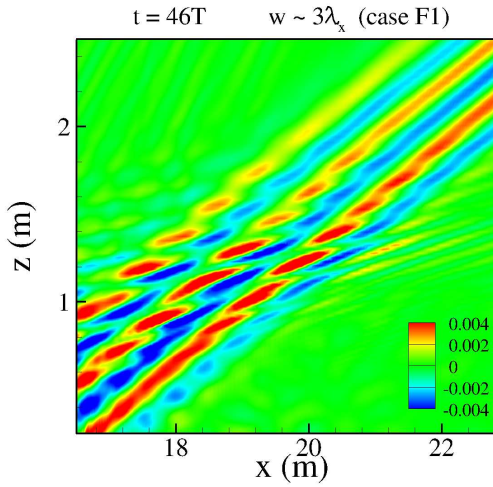

Figure 3.8: Contour of horizontal velocity u (m/s) for case F1 at time t = 46 T. A freely propagating wave with the same characteristics as the reflected wave of case SUP3 undergoes PSI as shown in this snapshot.

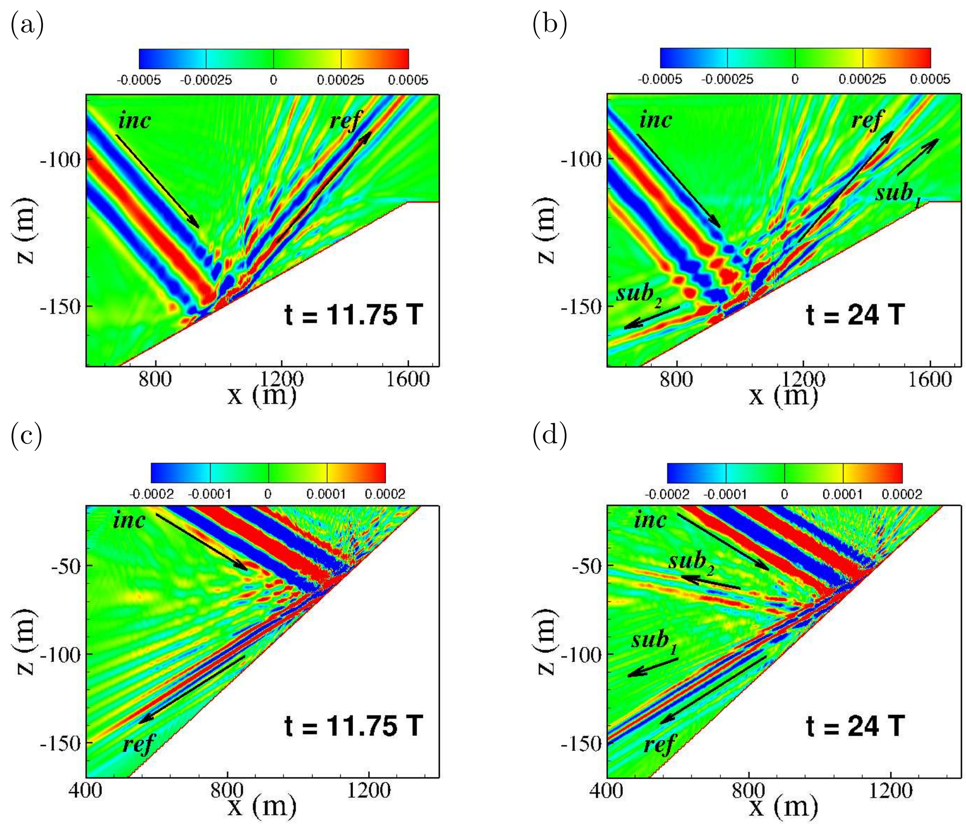

Figure 3.9: Contours of horizontal velocity u, (m/s) for large scale simulations: case SUP7 (upper row) and SUB8 (lower row) at times t = 11.75 T and t = 24T.

reflection ($\alpha > \beta$) and the slope angle $\beta = \sin^{-1}(0.5 \sin\alpha)$ is chosen such that it can accommodate subharmonic waves of frequency 0.5Ω. Case SUB8 is subcritical reflection ($\alpha < \beta$) and the slope angle is chosen as $10.5°$ such that $|\alpha - \beta| \approx 3.5°$ is same for both cases SUP7 and SUB8. Figures 3.9(a) and 3.9(b) show the horizonal velocity field for supercritical reflection at times $t = 11.75T$ and $t = 24T$, respectively. At time $t = 11.75T$, the reflected wave and the superharmonic wave of frequency 2Ω are primarily seen along with the incident wave. At a later time $t = 24T$, two subharmonic waves, one propagating towards the left and the other propagating towards the right, are seen. The frequency spectra show that the subharmonic modes have frequencies $0.33\Omega(sub_2)$ and $0.67\Omega(sub_1)$, similar to the frequency division found in case SUP1e. Figures 3.9(c) and 3.9(d) show horizontal velocity contours for subcritical reflection (case SUB8) at times $t = 11.75T$ and $t = 24T$. Similar to the case of supercritical reflection, subharmonic modes with frequencies 0.33Ω and 0.67Ω are seen at time $t = 24T$. In both these cases, the subharmonic mode with frequency 0.33Ω (sub_2) has higher energy compared to the subharmonic mode of frequency 0.67Ω (sub_1) due to the same reason (discussed for case SUP1e) that the group velocity for sub_2 is smaller compared to sub_1, and thus sub_2 has more time to interact and extract energy from the reflected wave. A difference to note between the cases of supercritical and subcritical reflection is that, in the supercritical reflection case, both the subharmonic waves make shallower angle with the slope compared to the reflected wave. However, in the subcritical reflection case, both the subharmonic modes make steeper angles with the slope (compared to the reflected wave) and are not spatially constrained by the slope.

3.4 Energetics

Growth rates of subharmonic wave energy $\sigma_{sub} = (1/E_{sub})dE_{sub}/dt$ and its cycle evolution is discussed in this section. Area-averaged subharmonic energy per unit mass,

$$E_{sub} = \frac{1}{A}\int \left(\frac{1}{2}(u_{sub}^2 + w_{sub}^2) + \frac{1}{2}(\frac{g\rho_{sub}^*}{\rho_0 N_\infty})^2\right) dA \ ,$$

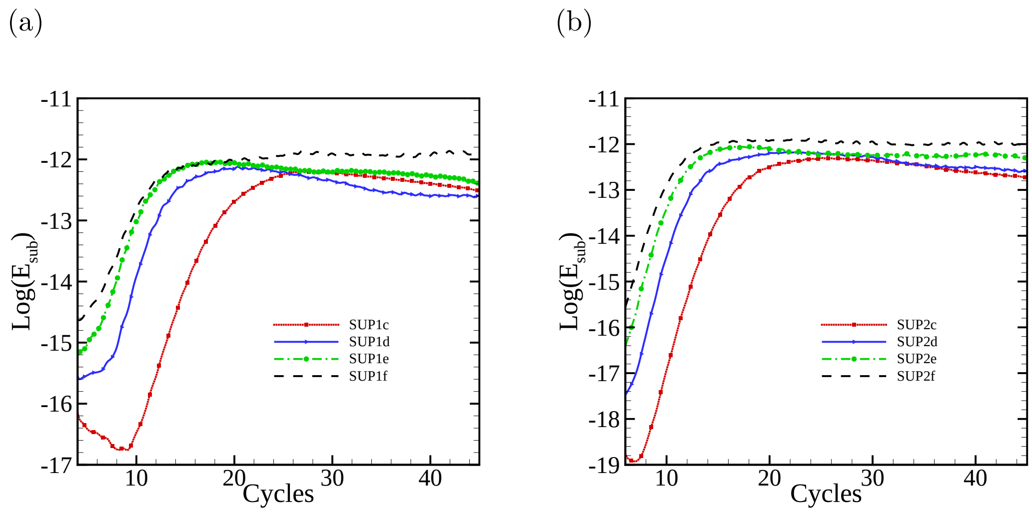

Figure 3.10: Cycle evolution of area-averaged subharmonic energy (kinetic + potential) for (a) top-hat beam (cases SUP1c-1f), (b) Gaussian beam (cases SUP2c-2f).

is calculated in a region surrounding the interaction zone. This area is chosen such that its lateral boundaries are sufficiently far from the interaction region, and the energy flux of subharmonic waves across the boundaries is negligible. Filtered fields $u_{sub}, w_{sub}, \rho^*_{sub}$ are obtained by considering a time series data of velocity and density fields at each point inside the chosen region. FFT of time series data is performed and a filter is applied around the desired subharmonic frequency, followed by an inverse Fourier transform. Figures 3.10(a)-(b) shows cycle evolution of subharmonic wave energy $Log(E_{sub})$ for cases SUP1c-1f and SUP2c-2f, respectively.

As time progresses, the subharmonic wave energy increases exponentially for all cases and a quasi-steady state with approximately constant energy is reached. The time at which the subharmonic wave energy reaches its peak value varies among the cases. When the reflected wave Froude number, Fr_r, increases from SUP 1c-f, the time to attain the peak value decreases for the top-hat beams as shown by figure 3.10(a). A similar trend is found for Gaussian wave beams (figure 3.10(b)). In total, the available incident wave energy is distributed among various frequencies including primary reflected wave, superharmonic and subharmonic frequencies with a fraction of the energy also going into viscous dissipation near the

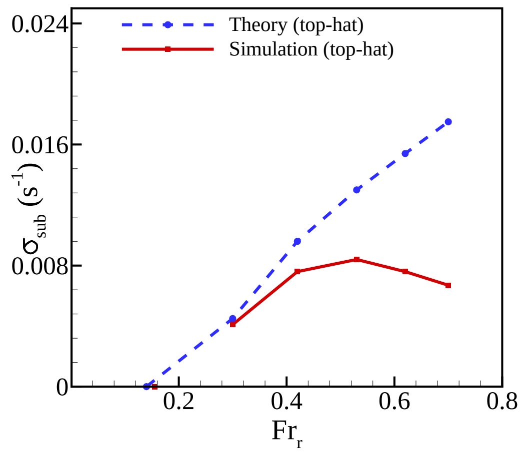

Figure 3.11: Subharmonic energy growth rates as a function of reflected beam amplitude (Froude number) compared between present simulations and theory of Karimi & Akylas (2014) for a series with top-hat beam profile (series SUP1a-1f).

reflection region.

The subharmonic growth rates in the simulations show a dependence on the reflected wave Froude number, Fr_r. It is of interest to place the results in the context of finite beam-width asymptotic theory (Karimi & Akylas, 2014) even though the assumptions of the analysis, namely, small amplitude beam and short wavelength subharmonics do not strictly apply. Details about the calculation of theoretical growth rates are given in the Appendix. Figure 3.11 compares growth rates for cases SUP1a-1f against theory.

We start with consideration of the critical value of Fr_r for onset of PSI. For a given wave of frequency Ω, wave number k, and beam envelope (whether top-hat or Gaussian) in a fluid of given viscosity, the critical value of Fr_r depends on the frequency of the subharmonic wave and the number of carrier wave lengths. As shown in figure 3.11, the theoretical critical value of Fr_r for a top-hat wave beam with 1.5 carrier wavelengths to generate a subharmonic with 0.5Ω is ≈ 0.145. Now, according to the simulations, case SUP1a with reflected wave Froude number 0.15 does not undergo PSI while case SUP1b with $Fr_r = 0.3$ does show PSI. Case SUP2a (Gaussian envelope) with $Fr_r = 0.25$ does not exhibit PSI. Therefore, we infer that the critical Froude number for the reflected wave beam to undergo

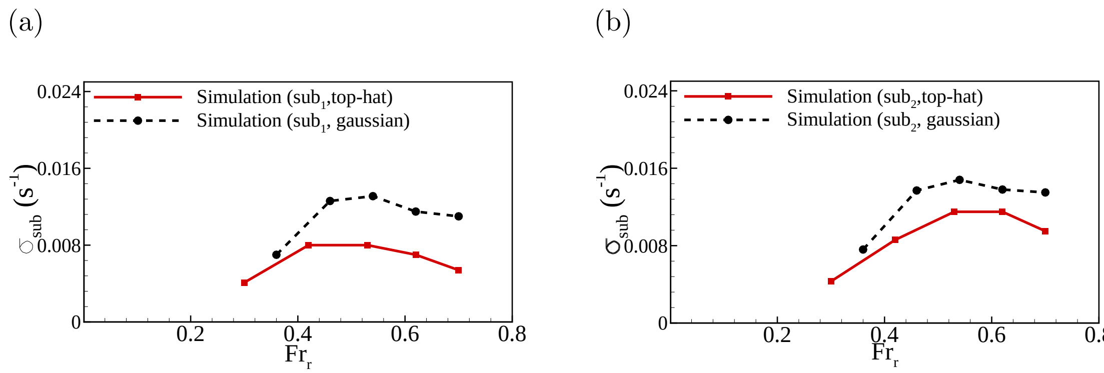

Figure 3.12: Comparison of subharmonic energy growth rates computed from the simulations between top-hat (cases SUP1b-1f) and Gaussian beams (cases SUP2b-2f).

PSI in the simulations is $0.25 - 0.3$, which is somewhat higher than the value predicted by Karimi & Akylas (2014). However, it is important to note that the subharmonic frequencies obtained in the simulation are 0.33Ω and 0.67Ω in contrast to subharmonic frequency $\Omega_{sub} \approx 0.5\Omega$ considered by Karimi & Akylas (2014).

We now turn to the magnitude of the subharmonic growth rates, σ_{sub}. At low values of Fr_r, the theoretical values of σ_{sub} agree well with the simulation values as shown in figure 3.11. When $Fr_r > 0.5$, σ_{sub} saturates at a value $\approx 0.008s^{-1}$, whereas theory predicts a continuing linear increase with increasing Fr_r, thus surpassing the simulation growth rates at high Fr_r. Figures 3.12(a) and 3.12(b) compare subharmonic growth rates between top-hat (SUP1) and Gaussian (SUP2) beam profiles. There is no qualitative difference with the top-hat beam; σ_{sub} increases with Fr_r for low values and then saturates for the Gaussian profile too. A quantitative difference is that σ_{sub} is higher for the Gaussian relative to the top-hat beam at all values of Fr_r. It is worth noting that Karimi & Akylas (2014) predict that the threshold value of Fr_r for the onset of PSI is smaller for the Gaussian beam profile consistent with a Gaussian beam being more unstable than the top-hat. The value of σ_{sub} for the left-traveling subharmonic mode (sub_2) is always higher relative to sub_1. The reason is that sub_2 has smaller group velocity compared to sub_1, has longer time to interact with the reflected wave and is, therefore, able to extract more energy.

The effect of beam width on the subharmonic energy growth rate is evaluated by doubling the beam width (compare cases SUP1b and SUP3). Theory and experiments predict that increasing the beam width, i.e., the number of carrier wavelengths, increases the growth rate. Our simulations are consistent with this prediction. Case SUP1b, with beam width $1.5\lambda_x$, has $\sigma_{sub} \approx 0.0042s^{-1}$, whereas SUP3 with beam width $3\lambda_x$ has $\sigma_{sub} \approx 0.0057s^{-1}$.

3.5 Discussion and conclusions

Through numerical simulations, we demonstrate that a stable propagating internal wave beam with small amplitude, upon reflection, leads to a reflected beam that can become unstable to PSI. Supercritical, critical and subcritical reflection with reflected wave angle larger, equal, and smaller, respectively, relative to the slope angle are simulated. Two different beam envelopes, top-hat and Gaussian, are considered. Since the off-criticality $(\alpha - \beta)$ is not large, the velocity of the reflected wave increases and wave length reduces in all the simulated cases leading to intensification of the reflected-wave Froude number, $Fr_r = uk_x/\Omega$. Linear theory is able to predict the intensification for small values of beam amplitude, but substantially overpredicts Fr_r for larger values. PSI is found in several of the simulated cases. For example, consider case SUP1e where the beam has an incoming $Fr_i = 0.076$ and a width of 1.5 wavelengths. At $t > 12T$ (figure 3.3) subharmonic modes emanate from the reflection region. The left traveling wave has a frequency 0.33Ω and the right traveling wave has a frequency 0.67Ω, adding up to the primary wave frequency. Both the horizontal and vertical wave numbers of the subharmonic modes add up to the corresponding quantities of the primary reflected wave showing that it is the reflected wave that undergoes the instability.

PSI of the internal wave beam is found to depend on the wave amplitude in series SUP1a-1f where the incoming beam amplitude is systematically varied, keeping all other parameters constant. In all cases exhibiting PSI, the subharmonic energy increases exponentially until it saturates to a nearly constant value. Subharmonic growth rates in the exponential-growth stage have been computed and compared against the theory of Karimi & Akylas (2014), based on asymptotically small beam amplitude and short subharmonic instability wave, for a freely propagating internal wave beam. For a given configuration (internal wave angle 18° and beam width $1.5\lambda_x$), PSI of the reflected wave is found in the simulations when $Fr_r \geq 0.3$. For $0.3 \leq Fr_r < 0.5$, the theoretical estimates of growth rate are close to the simulation values. On the other hand, for $Fr_r > 0.5$, the subharmonic growth rates obtained from the simulation data remains more or less constant, whereas the theoretical growth rates continue to increase linearly with Fr_r. The reason is that, in the simulations with high Fr_r, energy transfer to smaller scales becomes increasingly important and viscosity effectively dissipates energy at these scales. Karimi & Akylas (2014) found that increasing either the beam width or the internal wave angle (keeping the Froude number constant) increases the subharmonic growth rate. Thus, the threshold Froude number to undergo PSI is expected to be lower for wider and steeper internal wave beams. To study the effect of the beam width, case SUP3 is performed at an incoming wave Froude number $Fr_i = 0.03$ identical to SUP1b and a larger beam width of $3\lambda_x$ relative to $1.5\lambda_x$. Increasing the beam width from 1.5 to 3 carrier wavelengths is found to increase the growth rate by approximately a factor of 1.4. This result is consistent with the predictions by Karimi & Akylas (2014), however, a future parametric study that varies beam angle and beam width for given slope angle and compares the variation of critical Fr_r with theory is desirable.

Varying the shape of the beam envelope, keeping all the other parameters identical, does not qualitatively change the effect of beam amplitude. However, there is a quantitative effect on the subharmonic growth rates. As shown in figure 3.12(b), the Gaussian beam has higher subharmonic growth rates compared to the top-hat beam for a given value of Fr_r. This result is consistent with the result of Karimi & Akylas (2014) that the Gaussian beam is more susceptible to PSI compared to the top-hat beam.

From the preceding discussion, we conclude that higher-amplitude and wider incoming beams lead to reflected waves that are more prone to subharmonic instability. There is also a threshold for incoming beam amplitude for onset of PSI. These conclusions are consistent with the findings of Karimi & Akylas (2014), Bourget *et al.* (2014) in the case of freely-propagating wave beams. The values of the subharmonic growth rate in the simulations lie in the range, $0.004 < \sigma_{sub} < 0.014$ s^{-1} translating to 0.25 - 0.875 per cycle of the fundamental wave. These values are comparable to PSI growth rates in previous work.

Off-criticality $(\alpha - \beta)$ has a non-monotone effect on PSI. Decreasing off-criticality to zero suppresses PSI. The critical reflection $(\alpha = \beta)$ case C5 with parameters identical to case SUP1e does not show any signs of subharmonic instability. As shown in figure 3.6, the geometrical constraint due to the sloping bottom does not allow subharmonic modes (propagate with shallower angles than the fundamental) in quadrants 1 and 4, and the resonant wave number criterion for PSI does not allow subharmonic modes in quadrants 2 and 3. Thus, PSI of a critically reflected wave is suppressed. On the other hand, increasing the off-criticality $(\alpha - \beta)$ can be anticipated to weaken the reflected wave Fr based on the linear theory result, (3.5). Indeed, increasing the off-criticality to 12° (SUP4) from 8° (SUP3) by changing the slope angle, keeping all other parameters fixed, decreased the value of Fr_r sufficiently to suppress PSI.

Unlike Gayen & Sarkar (2013) and Bourget *et al.* (2013), increasing the Reynolds number (case SUP6) does not change the unequal frequency division among the subharmonic modes towards $\Omega_{sub} = 0.5$. Cases SUP7 and SUB8 with internal wave angle $\alpha = 7°$ and frequency corresponding to the M2 tide are performed to study reflection under more realistic oceanic conditions. Both these cases exhibit PSI with subharmonic frequencies 0.33Ω and 0.67Ω, similar to low Reynolds number simulations SUP1b-1f. In the case of supercritical reflection (case SUP7), the subharmonic frequency of 0.5Ω is possible only when both the subharmonic waves move along the slope with one daughter wave moving upslope in the first quadrant and the other daughter wave moving downslope in the third quadrant, and both waves grazing the slope. There are no boundary related constraints for equal-frequency subharmonics in the subharmonic case SUB8. However, equal division of subharmonic frequencies into 0.5Ω is absent in both cases SUP7 and SUB8 although the Reynolds number ($Re_i = u_i/(k_{x,i}\nu)$) is approximately 7 times larger compared to case SUP1e. It is possible that equal division of frequency in the reflection problem could occur at even higher values of Re.

In all the simulated cases which exhibit PSI, instability of the reflected wave is initiated near its generation region at the slope because the reflected wave is strongest near its origin. As the reflected wave becomes unstable near the generation region and loses energy to subharmonic modes, it becomes weaker as it travels away from the generation region. Therefore, although at a later time the reflected wave undergoes subharmonic instability away from its generation region, the instability is not as strong as it is near the reflection zone.

The present study identifies off-critical internal wave reflection as a mechanism for nonlinear cascade of internal waves to waves of smaller vertical scale through parametric subharmonic instability. In the future, three dimensional turbulence resolving simulations of internal wave beam reflection will be helpful to quantify the contribution of subharmonic modes to the turbulent dissipation at the bottom boundary.

3.6 Appendix: Calculation of theoretical growth rates

Theoretical growth rates that are employed for comparison in this paper are calculated from the results reported in Karimi & Akylas (2014) (hereafter referred to as KA). Several non-dimensional parameters introduced by KA as part of the the analysis are defined below, followed by the expression used by us to compute the dimensional subharmonic growth rate. All the dimensional quantities in the following discussion are denoted by the superscript $*$.
The characteristic length scale of the reflected wave beam is defined as

$$L^* = 1/k^*_{ref}, \tag{3.6}$$

where k^*_{ref} is the wave number of the reflected beam measured from the simulation data. The time scale used by KA for nondimensionalization is given by $1/N^*$, where

N^* is the buoyancy frequency. The wave amplitude parameter (also measures the degree of nonlinearity) is given by

$$\epsilon = Fr/\cos\,\alpha, \tag{3.7}$$

where α is the angle that the group velocity vector of the reflected wave makes with the horizontal and $Fr = u^* {k^*}_x/\Omega^*$ is the Froude number of the wave (reflected wave in the simulation) undergoing PSI. The scaled beam width is given by $D = 2\pi N_w \epsilon^{1/2}$, where N_w is the number of wavelengths of the reflected wave.

The non-dimensional growth rate λ_r (real part of the complex eigenvalue) as defined in equation (4.12) of KA is given by

$$\lambda_r = \gamma \frac{\hat{\lambda}_r}{\hat{k}} - \frac{\tilde{\nu} c^2}{D^2 \gamma^2} \hat{k}^2, \tag{3.8}$$

where $\hat{\lambda}(\hat{k})$ is obtained by solution of a characteristic equation. Here, the parameter $\tilde{\nu}$ (denoted by α in KA) is a nondimensional viscosity,

$$\tilde{\nu} = \frac{\nu^*}{2N^* {L^*}^2 \epsilon^2}\ , \tag{3.9}$$

and $\gamma = \sin\,\chi\,\cos^2(\chi/2)$, where $\chi = \alpha - \alpha_{sub}$, and α_{sub} is the angle made by the subharmonic group velocity vector with the horizontal. The relation between α and α_{sub} is given by $\sin\alpha/\sin\alpha_{sub} = \Omega/\Omega_{sub}$, where $\Omega = \Omega^*/N^*$ is the non-dimensional reflected wave frequency and Ω_{sub} is the non-dimensional subharmonic wave frequency. The nondimensional group velocity is $c = \Omega_{sub}(2 - \cos\,\chi)$ and the non-dimensional subharmonic wave number is

$$k_{sub} = L^* k^*_{sub}, \tag{3.10}$$

where k^*_{sub} is the average of left and right subharmonic wave numbers measured from the simulation data. The subharmonic frequencies (Ω_1 and Ω_2) are unequal in the simulation in contrast to $\Omega_{sub} \approx \Omega/2$ assumed by KA. In order to compare with theory, we employ the average frequency, $\Omega_{sub} = (\Omega_1 + \Omega_2)/2$, which also equals $\Omega/2$.

Solving the eigenvalue problem for a given beam envelope (top-hat is chosen in this paper for comparison) gives $\hat{\lambda}(\hat{k})$, which is plotted in figure 3 of KA. Two asymptotic limits are discussed, one near the bifurcation point $\hat{k} = \hat{k}_c^{(0)}(= \pi)$ and the other when $\hat{k} >> \hat{k}_c^{(0)}$. The solution $\hat{\lambda}(\hat{k})$ in these two asymptotic limits is given by equations (5.7) and (5.8) of KA, respectively. The value $\hat{k}$ obtained from the simulation data is found to be in the range 2π to 6π for cases SUP1b-1f, and all these values are within the range $\hat{k}_l < \hat{k} < \hat{k}_u$ as predicted by KA. Since the slope of the curve $\hat{\lambda}^{(0)}(\hat{k})$ (shown in figure 3 of KA) changes rapidly near the bifurcation point and remains nearly constant thereafter, and also the $\hat{k}$ values obtained from the simulation data for cases SUP1b-1f are always greater than $\hat{k}_c^{(0)}$, we employ equation (5.8) of KA in the asymptotic limit $\hat{k} >> \hat{k}_c^{(0)}$. Thus, we obtain $\hat{\lambda}^{(0)} = \hat{k}/2$.

Since KA define $\hat{k} = (\gamma D/c)k$ and the maximal instability growth rate is $\hat{\lambda}_r = \hat{\lambda}^{(0)} = \hat{k}/2$, (3.8) leads to the following nondimensional expression for the subharmonic growth rate:

$$\lambda_r = \frac{\gamma}{2} - \tilde{\nu} k_{sub}^2 \,. \tag{3.11}$$

Finally, the dimensional subharmonic growth rate is given by $\epsilon N^* \lambda_r$.

3.7 Acknowledgements

The contents of this chapter has been recently accepted for publication in Journal of Fluid Mechanics (Oct. 2015), coauthored by Professor Sutanu Sarkar. V. K. Chalamalla, & S. Sarkar (2015) PSI in the case of internal wave beam reflection at an uniform slope., *Journal of Fluid Mechanics* (*in press*).

Chapter 4

Mixing, dissipation rate, and their overturn-based estimates in a near-bottom turbulent flow driven by internal tides.

4.1 Introduction

It is well known that internal tides generated at rough topography lead to near-bottom turbulence during generation and reflection. Many observational studies have found enhanced mixing near topographic boundaries (Kunze & Toole, 1997; Eriksen, 1998; Munk & Wunsch, 1998; St. Laurent *et al.*, 2001; St. Laurent & Garrett, 2002; Moum *et al.*, 2002; Cacchione *et al.*, 2002; Rudnick *et al.*, 2003; Nash *et al.*, 2004; Aucan *et al.*, 2006) that is modulated at tidal frequencies. Accurate quantification of the turbulence and mixing at rough topography is a prerequisite for parameterization of tidal mixing in ocean models, inferring mixing rates from observed overturns, and ultimately to our ability to model the global ocean circulation (Vallis, 2000; Park & Bryan, 2000; Wunsch & Ferrari, 2004).

Due to the large variation of scales ranging from $\mathcal{O}$ (km) down to $\mathcal{O}$ (cm), simulations of oceanic internal tides that resolve the complete range of spatial and temporal scales are still beyond our capability. Nevertheless, recent simulations in an idealized setting have been helpful by showing pathways to turbulence through wave breaking near the top of topographic features (Legg & Klymak, 2008; Klymak *et al.*, 2010; Rapaka *et al.*, 2013), in intensified boundary flows at near-critical slopes (Gayen & Sarkar, 2011*c*) in the generation problem, and during reflection at critical and near-critical slopes (Chalamalla *et al.*, 2013). Convective instability was found to be responsible for transition to turbulence at near-critical slopes through the generation of counter-rotating streamwise rolls by Gayen & Sarkar (2010b) who employed DNS for a laboratory-scale model problem. In a scaled-up LES, Gayen & Sarkar (2011*a*) found vigorous turbulence following large convective overturns during flow reversal from downslope to upslope flow similar to the observation by Aucan *et al.* (2006) at a deep flank of Kaena ridge. Convective overturns have been identified above topography, e.g, at the crest of Kaena ridge by Klymak *et al.* (2008) in an observational study, in the bottom boundary layer of lakes (Lorke *et al.*, 2005, 2008; Becherer & Umlauf, 2011), in two-dimensional simulations (Legg & Klymak, 2008; Buijsman *et al.*, 2012), and in three-dimensional DNS and LES (Rapaka *et al.*, 2013). From the prevailing literature, it is thus clear that convective instability is one likely route to mixing in internal tides. However, accurate quantification of the amount of turbulent mixing accomplished by the convective overturns, especially given the oscillatory shear and stratification of near-bottom internal tides, remains an outstanding issue that motivates the DNS and LES of the present model problem.

A popular method to infer turbulent dissipation rate from observational data is based on the overturning length scale (Thorpe, 1977) which is a measure of the vertical extent of density overturns computed by adiabatically rearranging the density profile to attain a stable configuration. The Thorpe length scale, L_T, is defined as the r.m.s of the parcel displacements required to attain a density profile that is statically stable. Dillon (1982) performed a detailed study of the overturn method using measurements in the upper ocean. The ratio of Ozmidov scale, $L_O = \sqrt{\varepsilon/N^3}$, to Thorpe scale L_T was found to be of the same order in regions far away from the wind-driven boundary layer, both in mixed layers and in seasonal thermoclines. The turbulent dissipation rate was estimated to be $\varepsilon \propto {L_T}^2 N^3$, where N is the buoyancy frequency. Diapycnal diffusivity can also be estimated (Osborn, 1980) using $K_\rho = \Gamma\varepsilon/N^2$, where Γ is the mixing efficiency, often taken to be 0.2. Observational studies of internal tides, e.g., Alford *et al.* (2006); Martin & Rudnick (2006); Levine & Boyd (2006) often infer turbulent dissipation rate and diapycnal diffusivity from overturns although there are notable exceptions involving direct measurements of dissipation rate using shear probes, e.g. in Brazil Basin by Polzin *et al.* (1997*b*) and at the Hawaiian Ridge by Klymak *et al.* (2006).

During the mixing near bottom topography driven by internal tides, the evolution of Thorpe and Ozmidov scales could be different because of the strong and systematic temporal variability of turbulence. The three-dimensional, turbulence-resolving simulations performed here enable a direct calculation of the ratio of Ozmidov to Thorpe scales, as we can independently calculate both length scales from the available simulation data. The relationship between Thorpe and Ozmidov scales has been explored in the case of shear driven turbulence in previous studies. For instance, Smyth *et al.* (2001) analyzed DNS of the nonlinear evolution of Kelvin-Helmholtz billows finding that the ratio of Ozmidov to Thorpe length scales, L_O/L_T, continuously increases during the evolution from a very small value to an O(1) value. The flux coefficient, $\Gamma_i = B_i/\epsilon$, where B_i is the irreversible buoyancy flux was found to decrease with increasing time or, equivalently, with increasing value of L_O/L_T. More recently, Mater *et al.* (2013) examined the relationship between L_T and L_O using three-dimensional DNS results of decaying, statistically homogeneous, stratified turbulence. It was found that L_T and L_O were not linearly related. Instead, large overturns were found to be reflective of turbulent kinetic energy rather than turbulent dissipation rate in strongly stratified ($NT_L > 1$ where T_L is a large-eddy turbulence time scale) situations. In the present study, the evolution of Ozmidov and Thorpe length scales is discussed in the context of convectively driven turbulence in an oscillating boundary flow, the energetics of which is quite different from shear driven turbulence. In shear driven turbulence, direct transfer from mean kinetic energy to turbulent kinetic energy occurs through shear production. However, in convectively driven turbulence, mean kinetic energy drives the flow to a statically unstable density configuration, leading to an increase in the available potential energy, which is then released to turbulence through break down of the density overturn. The overturning length scale L_T in this context is representative of the potential energy available in an overturn to be released to turbulence and eventually to dissipation and background mixing. In the present problem, the density variation returns to a statically stable state owing to the oscillatory nature of the flow.

Ocean models utilizing internal tide parameterizations (Simmons *et al.*, 2004) suggest that the spatial and temporal variability of turbulent diffusivity need to be taken into account to properly model bottom abyssal stratification. The mixing efficiency, Γ, which is used to estimate diapycnal diffusivity, K_ρ, from turbulent dissipation rate through $K_\rho = \Gamma\varepsilon/N^2$ has often been oversimplified in ocean models by assuming a constant value of $\Gamma = 0.2$. In shear dominated flows, a small fraction is utilized for mixing the density field (Linden, 1979; W.R. & Caulfield, 2003; Ivey *et al.*, 2008). In contrast, convective instabilities show higher mixing efficiencies (Dalziel *et al.*, 2008; Gayen & Sarkar, 2013). Also, Γ varies substantially during a turbulent event (Smyth *et al.*, 2001; Dalziel *et al.*, 2008), suggesting that the systematic phasing of turbulence that is know to occur in internal tide driven mixing needs to be considered. In the present study, we calculate the mixing efficiency and diapycnal diffusivity from the values of turbulent dissipation, irreversible diapycnal flux and the stratification available from the simulation data.

The paper is organized as follows: The formulation of the problem is given and numerical method is summarized in section 2. The cyclic variation of turbulent kinetic energy and density variance budgets is described in section 3. In section 4, the evolution of available potential energy (which represents the energy that can be released to drive fluid motion) and irreversible diapycnal flux (which represents the transfer of energy from available to background potential energy) is discussed. The evolution of Thorpe and Ozmidov scales during the period of large convective overturns is described in section 5. Sections 6 and 7 contain results regarding the mixing efficiency and diapycnal diffusivity, respectively. The paper concludes with conclusions drawn in section 8.

4.2 Formulation

The schematic of the problem is shown in figure 4.1. The baroclinic bottom flow has thickness l_b, peak velocity U_b, and oscillates with the M2 tidal frequency. The width l_b is defined as the slope-normal distance between the bottom and the first zero crossing of the along-slope velocity. Going beyond Gayen & Sarkar (2011*a*), we present new results regarding the evolution of scalar variance, mixing efficiency and the recipe for inferring turbulent dissipation rate from overturns.

In our previous simulations of internal tide generation at laboratory scale (Gayen & Sarkar, 2011*c*; Rapaka *et al.*, 2013) and two-dimensional large-scale simulations, an oscillating barotropic tide leads to a baroclinic boundary flow with amplitude U_b and thickness l_b that is maintained against turbulent losses by barotropic-to-baroclinic energy conversion. Turbulence-resolving, three-dimensional simulations in streamwise-inhomogeneous domains of O(10) km required to realize O(100) m overturns in the baroclinic bottom boundary layer are not yet possible. We therefore adopt the approach described by Gayen & Sarkar (2011*a*). Thus, a patch of the larger-scale internal wave is simulated in a domain that is periodic in the spanwise and along-slope directions. The velocity amplitude U_b is maintained by adding a forcing term, $-\sigma_f(z_s)[u_s(x,t) - u_{s,f}(z_s,t)]$, to the right hand side of the along-slope momentum equation. The target velocity $u_{s,f}$ is given by

$$u_{s,f}(z_s,t) = A_0 \exp(A_1 z_s) \sin(A_2 z_s) \sin(\Omega t + \phi_0) \quad , \quad l_b/3 \le z_s \le l_b \, , \tag{4.1}$$

where z_s is the slope-normal coordinate and l_b is the slope-normal distance between the bottom and the first zero crossing of the along-slope velocity. The frequency is $\Omega = 0.0001407$ (rad/s), and the quantity $\sigma_f(z_s)$ is the forcing term with a value $\sim (1/\Delta t)$ (where Δt is the time step of the numerical simulation) in the forcing region that tends to zero outside the forcing region. The dimensional coefficients $A_0 = U_b/0.47$, $A_1 = -1.85/l_b$, and $A_2 = 3.2/l_b$ are chosen as a best fit of the chosen function to the shape of self-similar velocity profiles obtained for different slope lengths in the laboratory-scale internal wave generation problem of Gayen & Sarkar (2011c). The value of $\phi_0 = -\pi/2$, that is, the simulation starts with a phase corresponding to peak downslope initial velocity. The density is initialized with the background profile which describes the density variation at this phase. The flow cyclically restratifies in the internal wave generation problem during downslope flow and subsequently, during upslope flow, unstable stratification and convective overturns occur as is known from our laboratory-scale three-dimensional simulations (Gayen & Sarkar, 2011c; Rapaka *et al.*, 2013), observations and our large-scale two-dimensional simulations. We emulate the restratification here by renormalizing the density to the linear background during a short period (0.5 hrs) when the flow is at maximum downslope phase during the end of each wave cycle. All the quantitative results discussed in this paper such as mixing efficiency, turbulent dissipation and diffusivity are discussed for the first wave cycle (without density forcing) and, thus, the density restratification does not have any impact on the presented results. The renormalization is performed to sustain convectively-driven turbulence during the subsequent cycles and ensure a quasi-steady turbulence state with turbulence levels similar to that in the first cycle. We have verified that the mixing efficiency in the subsequent two cycles is similar to that in the first cycle in cases with no density forcing and with partial density forcing although the turbulence level decreases.

Two cases are considered: (1) Width $l_b = 6$ m and a peak velocity amplitude of $U_b = 0.0125$ m/s leading to Re small enough to allow DNS, and (2) Width $l_b = 60$ m and a peak velocity amplitude of $U_b = 0.125$ m/s that is closer to oceanic conditions. Both cases have the same value of background stratification N_∞ and wave shear U_b/l_b. Physical and computational parameters for the simulations are given in table 4.1. The choice of background stratification $N_\infty \sim \mathcal{O}(10^{-3})$ rad/s is consistent with measurements at deep (order 1 km) flanks of rough topography, e.g. Kaena Ridge (Aucan *et al.*, 2006)and the west ridge of the double-ridged Luzon Strait (Buijsman *et al.*, 2012).

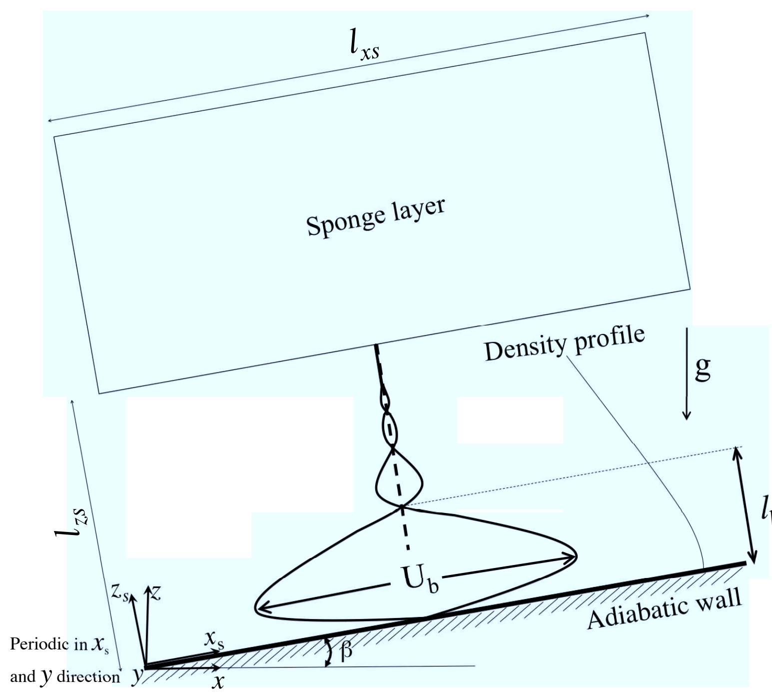

Figure 4.1: Schematic of the problem showing the oscillating along-slope velocity profile with width l_b and amplitude U_b. Slope makes an angle β w.r.t the horizontal. The slope-normal coordinate z_s is related to the vertical coordinate z by $z = x_s sin\beta + z_s cos\beta$. The density profile shown in the schematic is referenced w.r.t the slope-normal axis z_s.

4.2.1 Governing equations

Direct and large eddy simulations are performed to numerically solve the Navier-Stokes equations, under the Boussinesq approximation, in a non-rotating environment. Rotation of the earth is not considered in this study, since the time scale over which the convective instability evolves is too small for the rotation to have a direct effect on turbulent dissipation and mixing, the main focus of this paper. However, rotation can effect the baroclinic boundary flow, and this implicit effect of rotation is not considered in this study for simplicity. The dimensional form of the governing equations in the reference axis system $[x_s, y_s, z_s]$ rotated by an angle β with respect to the horizontal in the x-z plane is as follows:

$$\nabla \cdot \mathbf{u}_s = 0, \tag{4.2a}$$

$$\frac{D\mathbf{u}_s}{Dt} = -\frac{1}{\rho_0}\nabla p^* - \frac{g\rho^*}{\rho_0}(\sin\beta\mathbf{i} + \cos\beta\mathbf{k}) + \nu\nabla^2\mathbf{u}_s - \nabla\cdot\boldsymbol{\tau}, \tag{4.2b}$$

$$\frac{D\rho^*}{Dt} = \kappa\nabla^2\rho^* - \frac{d\rho^b}{dz}(u_s\sin\beta + w_s\cos\beta) - \nabla\cdot\boldsymbol{\lambda}. \tag{4.2c}$$

Here, u_s, v_s, w_s are along-slope, spanwise and slope-normal velocities respectively in a rotated coordinate system. Equations (4.2)a-(4.2)c will be solved numerically, details of the numerical method are discussed in the following section. Here, p^* denotes the deviation from the background hydrostatic pressure and ρ^* denotes the deviation from the linear background state, $\rho^b(z)$. z represents the true vertical coordinate here. For LES simulations, $\mathbf{u}_s$ and ρ^* represent filtered quantities. $\boldsymbol{\tau}$ and $\boldsymbol{\lambda}$ represent subgrid scale stress tensor and density flux vector, respectively. The subgrid scale stress tensor $\boldsymbol{\tau}$ in Equation (4.2)b is computed using the dynamic mixed model (Zang *et al.*, 1993; Vreman *et al.*, 1997) and a dynamic eddy diffusivity model (Armenio & Sarkar, 2002) is used for the density flux vector $\boldsymbol{\lambda}$,

$$\tau_{ij} = -2\nu_T\overline{S_{ij}} + \widehat{\overline{u}_i\overline{u}_j} - \widehat{\overline{u}}_i\widehat{\overline{u}}_j, \qquad \nu_T = C\overline{\Delta}^2|\overline{S}| \tag{4.3}$$

$$\lambda_j = -\kappa_T\frac{\partial\overline{\rho^*}}{\partial x_j}, \qquad \kappa_T = C_\rho\overline{\Delta}^2|\overline{S}| \tag{4.4}$$

where $\hat{()}$ represents the test filter, and $\bar{()}$ represents the grid filter. $\bar{\Delta}$ is the grid filter size, S_{ij} is the strain rate tensor, and $|S| = \sqrt{2S_{ij}S_{ij}}$.

The eddy viscosity and diffusivity coefficients, ν_T and κ_T defined above, are computed using current values of velocity and density. Here, C and C_ρ are the Smagorinsky coefficients evaluated through a dynamic procedure (Germano *et al.*, 1991) through the introduction of an additional test filter. The coefficients are averaged over the homogeneous directions (slope parallel plane), expressions for calculating these coefficients are described by Gayen *et al.* (2010a). For the DNS, $\boldsymbol{\tau}$ and $\boldsymbol{\lambda}$ are zero.

4.2.2 Boundary conditions

No slip boundary conditions are imposed at the bottom boundary for u_s,v_s, and w_s. The total density can be written as the sum of background density and density deviation:

$$\rho = \rho_0 + (z_s \cos\beta + x_s \sin\beta)\frac{d\rho^b}{dz} + \rho^*. \tag{4.5}$$

Zero mass flux boundary condition is imposed at the sloping bottom resulting in the density deviation at the sloping boundary given by

$$\frac{\partial \rho^*}{\partial z_s} = -\cos\beta\frac{d\rho^b}{dz}. \tag{4.6}$$

4.2.3 Numerical method

The simulations use a mixed spectral/finite difference algorithm. Derivatives in the streamwise and spanwise directions are treated with a pseudo-spectral method and derivatives in the vertical direction are computed with second-order finite differences. A staggered grid is used in the wall-normal direction. A low-storage third-order Runge-Kutta-Wray method is used for time stepping, and viscous terms are treated implicitly with the Crank-Nicolson method. The code is parallelized using the message passing interface (MPI). Periodicity is imposed in the x_s and y_s directions. The top boundary is an artificial boundary correspond-

Table 4.1: Parameters of the simulated cases. Each case has background stratification $N_\infty = 1.6 \times 10^{-3}$ rad/s, frequency $\Omega = 1.407 \times 10^{-4}$ rad/s, and slope angle $\beta = 5°$. The Reynolds number is based on the amplitude of the bottom velocity, U_b, and the Stokes boundary layer thickness, $\sqrt{2\nu/\omega}$. The bulk Richardson number defined as $Ri_b = N_\infty^2 {l_b}^2/{U_b}^2$ is 0.59 for both the cases. The kinematic viscosity ν is taken as 10^{-6} m^2/s and Prandtl number $Pr = 7$. Reference density ρ_0 is taken as 1000 kgm^{-3} for all the cases. Grid spacing for case 1 is $\Delta x = 0.019, \Delta y = 0.008, \Delta z_{min} = 0.002$, and for case 2 is $\Delta x = 0.23, \Delta y = 0.156, \Delta z_{min} = 0.0037$, all dimensions in meters. Δz^+ is ≤ 1.6 for DNS and ≤ 10 for the LES case. The minimum value of Kolmogorov length scale is $\eta_{k,min} \approx 0.002$ m in both the cases. Stokes boundary layer thickness $\delta_s = \sqrt{2\nu/\Omega}$ is 0.12 m in both the cases.

Case	U_b (m/s)	l_b (m)	$Re_s = U_b\delta_s/\nu$	N_x	N_y	N_z	l_{xs} (m)	l_y (m)	l_{zs} (m)	Remark
1	0.0125	6	1500	256	128	513	5.0	1.0	15.0	DNS
2	0.125	60	15000	128	64	641	30.0	10.0	150.0	LES

ing to the truncation of the domain in the vertical direction. Rayleigh damping or a sponge layer is used to minimize spurious reflections from the artificial boundary into the computational domain. The velocity and scalar fields are relaxed towards the background state in the sponge region by adding damping functions -$\sigma(z_s)\left[(u_s, v_s, w_s)\right]$ and $-\sigma(z_s)\left[\rho^*\right]$ to the right hand side of the momentum and scalar equations, respectively. The value of $\sigma(z_s)$ increases exponentially from zero at the bottom boundary of the sponge to a maximum value of $\sigma(z_s)\Delta t \sim \mathcal{O}(0.1)$.

4.2.4 Turbulence diagnostics

Various averaging procedures are used in analyzing the results of this study. Reynolds average, denoted by angle brackets $\langle . \rangle$, is computed by averaging in the slope-parallel plane. $\langle . \rangle_\phi$ represents phase averaging, $\langle . \rangle_z$ represents depth-averaging, and $\underline{(.)}$ represents averaging over the extent of an overturn. Any fluctuating quantity in the flow field is defined by subtracting the Reynolds average from the instantaneous value,

$$A' = A - \langle A \rangle \,. \tag{4.7}$$

The evolution of TKE is governed by the following equation:

$$\frac{dK}{dt} = P - \varepsilon + B - \frac{\partial T_j}{\partial x_j}, \tag{4.8}$$

where $K = 1/2\langle u_i' u_i'\rangle$, $P = -\langle u_i' u_j'\rangle\langle S_{ij}\rangle$ - $\langle\tau_{ij}\rangle\langle\overline{S_{ij}}\rangle$, $\varepsilon = \nu\langle\frac{\partial u_i'}{\partial x_j}\frac{\partial u_i'}{\partial x_j}\rangle$ - $\langle\tau_{ij}\overline{S_{ij}}\rangle$, $B = \frac{g_i}{\rho_0}\langle\rho' u_i'\rangle = -\frac{g}{\rho_0}\langle\rho' w'\rangle$, $T_j = \frac{1}{\rho_0}\langle p^{*\prime} u_j'\rangle - \nu\frac{\partial K}{\partial x_j} + \frac{1}{2}\langle u_i' u_i' u_j'\rangle$. Here, K denotes turbulent kinetic energy, P is turbulent production, ε is turbulent dissipation rate, B is turbulent buoyancy flux with w' denoting the fluctuating vertical velocity, $\frac{\partial T_j}{\partial x_j}$ is the divergence of the transport of turbulent kinetic energy with $s_{ij}' = \frac{1}{2}(\frac{\partial u_i'}{\partial x_j} + \frac{\partial u_j'}{\partial x_i})$ denoting the fluctuating strain rate.

The evolution of density variance is governed by the following equation:

$$\frac{d\langle\rho'^2\rangle}{dt} = T_\rho + P_\rho - \chi_\rho, \tag{4.9}$$

where, the scalar production $P_\rho = -2\langle u_j'\rho'\rangle\frac{\partial\langle\rho^*\rangle}{\partial x_j} - 2\langle\rho' w'\rangle\frac{d\rho^b}{dz}$ - 2 $\langle\lambda_j\rangle\frac{\partial\langle\overline{\rho^*}\rangle}{\partial x_j}$, scalar transport $T_\rho = \kappa\nabla^2\langle\rho'^2\rangle - \frac{\partial\langle u_j'\rho'^2\rangle}{\partial x_j}$, scalar dissipation rate $\chi_\rho = 2(\kappa + \kappa_T)\langle\frac{\partial\rho'}{\partial x_i}\frac{\partial\rho'}{\partial x_i}\rangle$, $\kappa_T = 0$ for the DNS case. Here, the molecular scalar diffusivity is defined by $\kappa = \nu/Pr$, where Pr is the Prandlt number.

4.3 Turbulence Budgets

The velocity is proportional to $\sin\phi$ where ϕ is the M2 tidal phase. The simulation starts at the phase ($\phi = -\pi/2$) of peak downslope velocity and linear background density profile. At this time, the density and velocity fields have no fluctuations with respect to their Reynolds average. The downward flow brings fluid in from above that is lighter than the fluid that it replaces. This causes the density gradient in the flow to progressively decrease. As shown in figure 4.6, the density profile spanning almost the entire region affected by the flow (except the thin boundary layer at the wall) becomes nearly uniform at $\phi = -0.3\pi$, exhibits a large region that is convectively unstable at $\phi = -0.15\pi$, and eventually breaks down into smaller overturns owing to turbulence at $\phi = 0.03\pi$. Figures 4.2(d)-(f) show the density field at various phases during the evolution of the convective

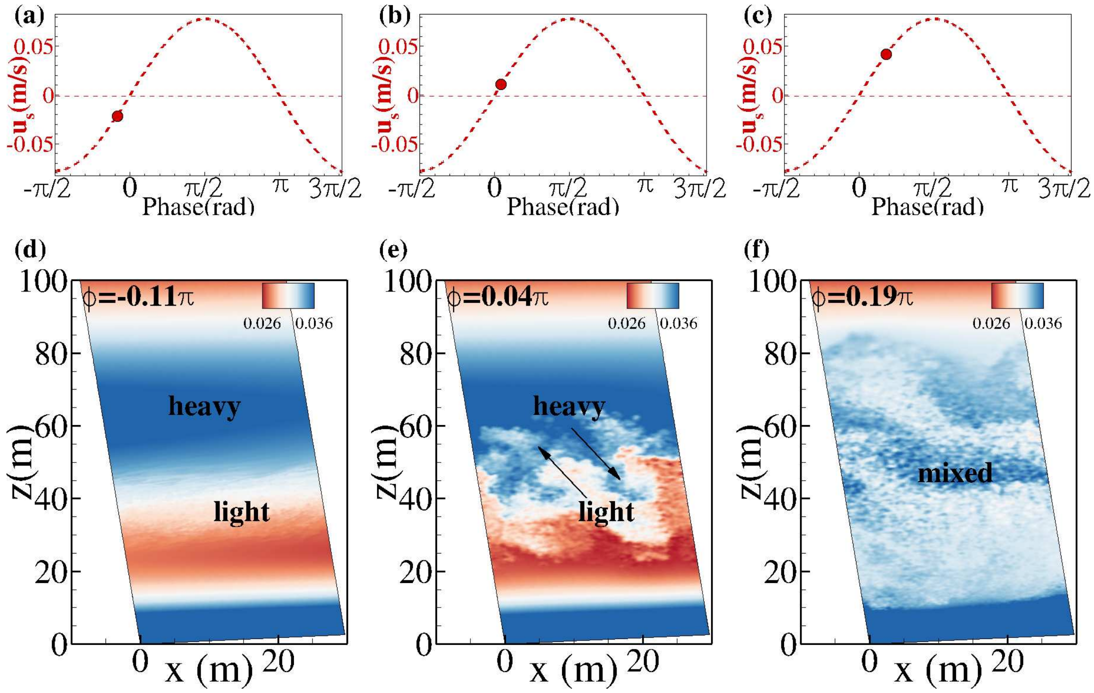

Figure 4.2: Density snapshots at various phases during the large convective overturning event from case 2. Top row shows the depth averaged streamwise velocity $\langle u_s \rangle$ (m/s) at various phases during the LCOE. The solid circle in each of these plots indicates the phase corresponding to the density snapshot directly below. Bottom row shows the snapshots of x-z density field ($\rho - 1000$) at various phases: (d) -0.11π, (e) 0.04π, and (f) 0.19π.

overturning event. The phase corresponding to each density snapshot is indicated by a solid circle in figures 4.2(a)-(c). At a phase $\phi = -0.11\pi$, just before the transition from downslope to upslope flow, lighter fluid is pushed from above which replaces the denser fluid between z $\approx$ 10 - 40 m as shown in figure 4.2(d). At a slightly later phase $\phi = 0.04\pi$, when the velocity is upslope but close to zero, the overturn breaks down into turbulence as shown in figure 4.2(e). At this phase, lighter fluid moves upward whereas the denser fluid moves downward, in the process of attaining a stable stratification. This large convective event mixes up the density field as shown at a later time in figure 4.2(f).

For completeness, we summarize the TKE balance that was previously discussed by Gayen & Sarkar (2011a) before presenting new results regarding the density variance balance. Figure 4.3(a) shows the cycle evolution of various terms in the TKE budget equation for case 1 along with the streamwise velocity (dotted-line) to establish the phase. All the terms plotted in this figure are averaged in the slope-normal direction. Corresponding to a convective instability, the turbulent buoyancy flux representing the transfer of available potential energy to turbulent kinetic energy starts to increase at phase $\phi \simeq -0.1\pi$ and peaks at $\phi \simeq 0$. We refer to this event during the flow reversal from downslope to upslope as LCOE (large convective overturning event) in our subsequent discussions. As the cascade to small scales proceeds, the turbulent dissipation rate progressively increases. Peak value of turbulent dissipation rate occurs at a slightly later phase $\phi \approx 0.08\pi$ when compared with the buoyancy flux. The transient term dK/dt follows a similar trend as the turbulent buoyancy flux throughout the LCOE, showing the dominance of buoyancy flux in the lifecycle of turbulence, a signature of convective instability. The shear production rate is small compared with the buoyancy flux. It has a small negative value just after upslope flow commences, a somewhat surprising phenomenon that is explained by Gayen & Sarkar (2011d) as due to the inclined coherent structures that form when shear distorts the convective overturns. Later, when the along-slope velocity approaches its positive maximum, the bottom boundary layer becomes turbulent due to the shear instability. During this phase of the cycle, the turbulent production is balanced by the turbulent dissipation rate whereas the buoyancy flux is negligible. At a later time, i.e., during the transition from upslope to downslope flow, no significant turbulent activity is observed. The reason is that the convective overturning region formed by heavier fluid replacing lighter fluid is close to the wall so that the eddies are restricted from growing by the bottom wall and also subject to stronger viscous damping.

Figure 4.3(b) shows the time evolution of various terms in the density variance equation. During the LCOE ($-0.15\pi \leq \phi \leq 0.2\pi$) there is an increase in scalar production and scalar dissipation. The transient term $\frac{d\langle \rho'^2 \rangle}{dt}$ averaged over the LCOE is approximately zero. Thus, the main balance is between the scalar production and scalar dissipation, i.e., hydrodynamic fluctuations extract energy from the background stratification to create scalar fluctuations which are dissipated at small scales by molecular effects. Scalar transport is negligible throughout the

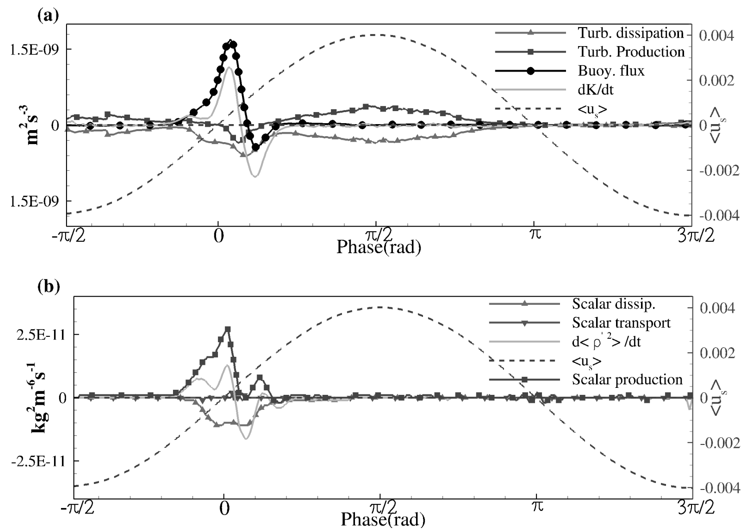

Figure 4.3: Cycle evolution (DNS, case 1): (a) TKE budget showing transient term dK/dt, turbulent production P, turbulent dissipation rate ε and turbulent buoyancy flux B; (b) Density variance budget showing transient term $d\langle \rho'^2 \rangle/dt$, scalar production P_ρ , scalar dissipation rate χ_ρ, scalar transport T_ρ. The dashed line is the depth averaged along-slope velocity $\langle u_s \rangle$ (m/s). All the quantities shown here are averaged along the slope-normal direction.

cycle. The evolution of scalar production resembles the buoyancy flux (shown in the TKE budget). Consider the scalar production term in the density variance equation:

$$P_\rho = -2\langle \rho' w_s' \rangle \frac{\partial \langle \rho^* \rangle}{\partial z_s} - 2\langle \rho' w' \rangle \frac{d\rho^b}{dz}, \tag{4.10}$$

$$P_\rho \approx B \frac{\rho_0}{g} \left(\frac{\partial \langle \rho^* \rangle}{\partial z_s} + \frac{d\rho^b}{dz} \right) \implies P_\rho \approx B \frac{\rho_0}{g} \frac{\partial \langle \rho \rangle}{\partial z}. \tag{4.11}$$

During the convective overturning event (LCOE), the density profile is unstable ($\frac{d\rho}{dz} > 0$). Since the buoyancy flux and the density gradient are both positive during the LCOE, the scalar production which is the product of the buoyancy flux and the density gradient is also positive and similar to buoyancy flux in its evolution. The second half of the tidal cycle in case 1 shows negligible activity in the density variance balance.

Figure 4.4(a) shows the time evolution of various terms in the TKE budget equation for case 2 simulated using LES. The turbulent dissipation is the sum of

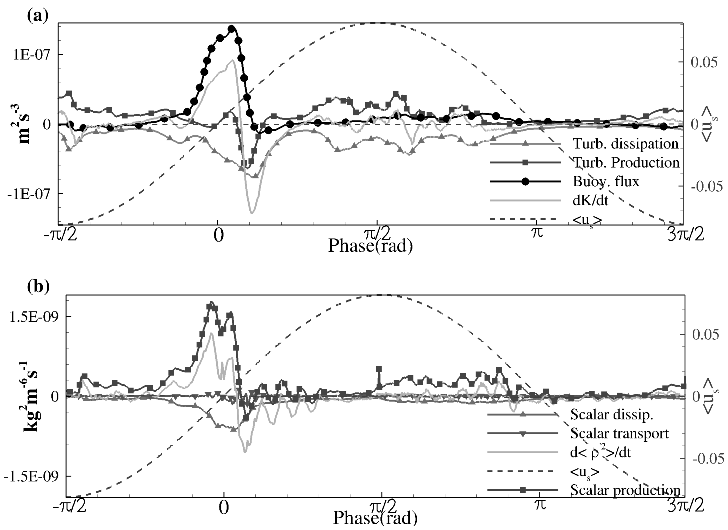

Figure 4.4: Cycle evolution (LES, case 2) of terms in the (a) TKE budget: transient term dK/dt, turbulent production P, turbulent dissipation rate ε and turbulent buoyancy flux B. (b)Density variance budget: transient term $d\langle\rho'^2\rangle/dt$, scalar production P_ρ , scalar dissipation rate χ_ρ, scalar transport T_ρ. The dashed line is the depth averaged along-slope velocity $\langle u_s\rangle$ (m/s). All the quantities shown here are averaged along the slope-normal direction.

the resolved and subgrid contributions. The flow evolution and the turbulence budgets are qualitatively similar to the low-Re DNS case discussed above. In the LES case, since the width of the beam is ten times larger than in the DNS case, the overturns are bigger and the magnitudes of terms in the turbulence budgets are higher compared to the DNS case. An important qualitative difference is that, at the smaller Re, the buoyancy flux is negative for some fraction of the LCOE whereas, at the larger Re, the buoyancy flux is almost always positive and lasts for a longer fraction of the cycle. Also, negative turbulent production is more prominent at higher Re, presumably because the inclined coherent structures suffer less damping by molecular viscosity. Figure 4.4(b) shows the time evolution of various terms in the density variance equation. The behavior is qualitatively similar to that at lower Re. One difference is that there is higher turbulence activity during $\pi/2 < \phi < \pi$ at higher Re. The TKE budget shows positive buoyancy flux during the phase $\pi/2 < \phi < \pi$ and the density variance budget show a slight increase in scalar production and dissipation at the same time. This activity is due to the turbulence created by combination of bottom shear (large upslope velocity) and convective overturns formed by the advection of heavier fluid from below.

4.4 Available Potential Energy

Background potential energy is calculated by reordering the density field (Winters *et al.* (1995);Winters & Barkan (2013)) such that it has stable stratification everywhere. A volume element dV_i with density ρ_i at depth z is assigned a new depth z^* in the re-ordered stable density profile. Background potential energy is defined by $BPE = \int_V \rho_i g z^* dV_i$. Available potential energy is then defined as the difference between total potential energy(TPE) and background potential energy(BPE),

$$APE = TPE - BPE = \int_V \rho_i g z dV_i - \int_V \rho_i g z^* dV_i. \tag{4.12}$$

The background potential energy evolves according to

$$\frac{d}{dt} BPE = \int_V g z^* \left(-\mathbf{u} \cdot \nabla \rho + \nabla \cdot (\kappa_{eff} \nabla \rho) \right) dV. \tag{4.13}$$

Using the product rule for divergence $z^* \nabla \cdot (\kappa_{eff} \nabla \rho) = \nabla \cdot (\kappa_{eff} z^* \nabla \rho) - \kappa_{eff} \nabla \rho \cdot \nabla z^*$, the second term in the above equation can be rewritten as

$$\frac{d}{dt} BPE = \int_V g z^* \left(-\mathbf{u} \cdot \nabla \rho \right) dV + g \int_V \nabla \cdot \left(z^* \kappa_{eff} \nabla \rho \right) dV - g \int_V \kappa_{eff} \nabla \rho \cdot \nabla z^* dV\,. \tag{4.14}$$

Following Winters *et al.* (1995), since z^* is a monotonic function of the density ρ and its spatial distribution depends implicitly on the density, a function ψ can be defined such that $z^* \nabla \rho = \nabla \psi$. Using the del operator product rule and the mass conservation equation $\nabla \cdot \mathbf{u} = 0$, the first term can be written as a surface integral. The second term in the above equation can also be written as a surface integral. Since z^* is a monotonic function of density, ∇z^* in the third term above can be written as $(dz^*/d\rho)\nabla\rho$ leading to,

$$\frac{d}{dt}BPE = -\int_S g\psi \mathbf{u}\cdot\mathbf{n}\, dS + g\int_S z^*\kappa_{eff}\nabla\rho\cdot\mathbf{n}\, dS - g\int_V \kappa_{eff}\frac{dz^*}{d\rho}|\nabla\rho|^2\, dV\, . \quad (4.15)$$

Finally,

$$\frac{d}{dt}BPE = \mathcal{F}_{adv} + \mathcal{F}_{diff} + \Phi_d. \quad (4.16)$$

In the case of LES, $\kappa_{eff} = \kappa + \kappa_T$, the sum of molecular and the eddy diffusivity. In the case of DNS, $\kappa_{eff} = \kappa$ (since $\kappa_T = 0$) is a constant. The first term on the r.h.s of equation (4.16) represents the change in background potential energy due to advective fluxes across the boundary of the integration domain. The second term represents the change in BPE due to the diffusive fluxes across the boundary and the third term is the irreversible diapycnal flux (Winters *et al.* (1995);Winters & D'Asaro (1996)) given by

$$\Phi_d = -g\int_V \kappa_{eff}\frac{dz^*}{d\rho}|\nabla\rho|^2\, dV. \quad (4.17)$$

Figure 4.5 shows density profiles at various time instances chosen to show the formation of the large convective overturn in case 1. The solid line represents the one-dimensional instantaneous density profile, which is constructed from the instantaneous three-dimensional density field. In the first step, each volume element is assigned an index ranging from i=1 to $(N_xN_yN_z)$. Starting with the left bottom corner of the domain, all the volume elements in the first $x_s - y$ plane (slope normal index = 1) are assigned indices ranging from 1 to N_xN_y in the order of span-wise and along-slope directions respectively. Then the second $x_s - y$ plane (slope-normal index = 2) is considered, with indices of volume elements ranging from N_xN_y+1 to $2N_xN_y$ and so on until the last $x_s - y$ plane, which has indices ranging from $N_xN_y(N_z - 1)$+1 to $N_xN_yN_z$. Each volume element dV_i is then squashed leading to a triangular or parallelogram shaped two-dimensional element of area $dA_i = dV_i/l_y$, and arranged in the vertical direction in the order of their indices, i.e volume element with index =1 is placed at the bottom followed by the volume element with index = 2 and so on. Each element is assigned a height z^*, which is the height of the centroid of the squashed two-dimensional element.

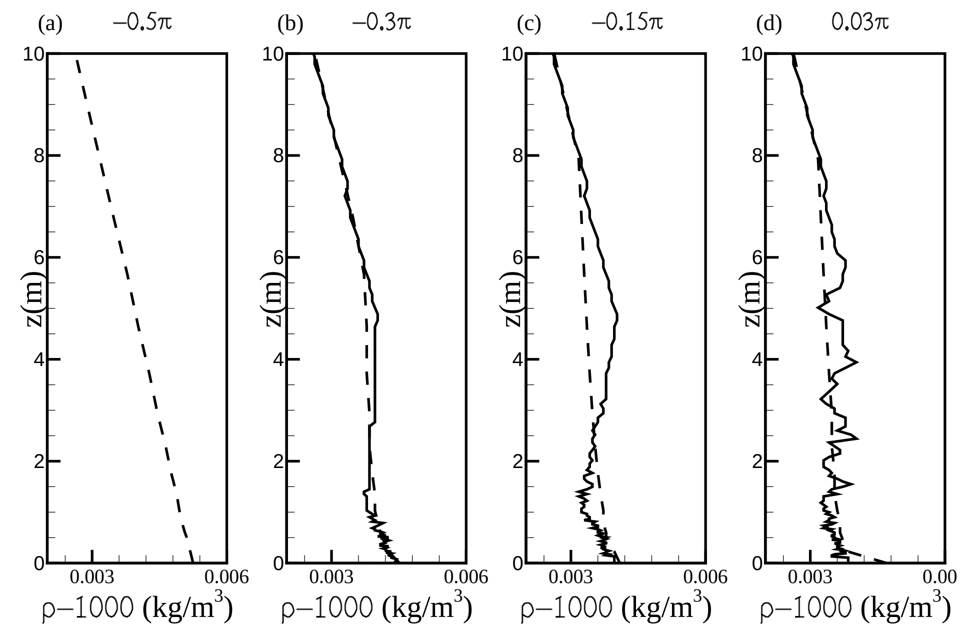

Figure 4.5: Density profiles at various time instances are shown for case 1: (a) $\phi = -0.5\pi$ (t=0), (b) $\phi = -0.3\pi$, (c) $\phi = -0.15\pi$, (d) $\phi = 0.03\pi$. The solid line represents the one-dimensional density profile obtained from the three-dimensional density field and the dashed line represents the re-ordered density profile.

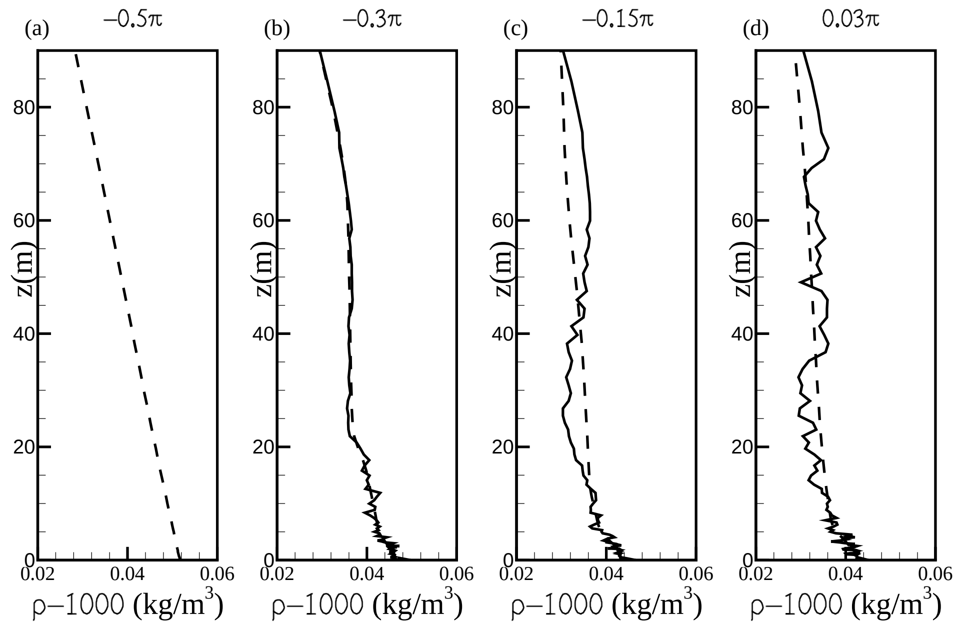

Figure 4.6: Density profiles at various phases shown for case 2: (a) $\phi = -0.5\pi$ (t=0), (b) $\phi = -0.3\pi$, (c) $\phi = -0.15\pi$, (d) $\phi = 0.03\pi$. The solid line represents the one-dimensional density profile obtained from the three-dimensional density field and the dashed line represents the re-ordered density profile.

The dashed line represents the one-dimensional reference state. The procedure employed in constructing the one-dimensional reference state is similar to that of the one-dimensional instantaneous profile, except that the density is sorted such that the stratification is stable everywhere. The densest element is placed at the bottom and the next dense element is placed on top of it and so on until the lightest of all the elements is placed at the top. A more detailed description about the reference state construction is available in Winters & Barkan (2013).

Figure 4.7 (a)-(b) shows the evolution of APE in the flow. The buoyancy flux and diapycnal flux are also shown to explain the phasing of these energy rate terms relative to the APE. The APE in the DNS (Figure 4.7 a) starts to increase at phase $\phi = -0.3\pi$ at the same time that the density profile starts deviating from the background. At a slightly later phase $\phi = -0.15\pi$, APE is close to maximum. The density profile at this phase (figure 4.5 c) shows a density overturn that extends from 1 m above bottom to 4 m above bottom, spanning half the bottom flow thickness. APE continues to increase until $\phi = -0.1\pi$, i.e., when the large overturn starts to break down into small scale turbulence. The irreversible diapycnal flux starts to increase at phase -0.1π, after the APE has reached its maximum value. It is worth noting that diapycnal flux commences to rise at the same phase when the TKE budget plot show an increase in the turbulent dissipation. Just after the state of zero flow, when $\phi = 0.03\pi$, many small scale density overturns are found spanning the entire thickness, $l_b = 6$ m, of the bottom flow. The evolution of these overturns and the corresponding Thorpe scales will be discussed in the subsequent sections of this paper. Diapycnal flux, which is a measure of irreversible mixing, continues to increase until $\phi \approx 0.08\pi$ and then starts to decrease, following a similar evolution as the turbulent dissipation rate shown in the TKE budget (figure 4.3). The buoyancy flux begins to rise at the same time that the diapycnal flux rises and peaks at a similar time. The peak value of the buoyancy flux is significantly larger than that of the diapycnal flux. However, the buoyancy flux decreases rapidly after its peak, plummets to zero, and attains negative values while Φ_d remains always positive.

The density profiles in case 2 show similar qualitative behavior. Figure 4.6

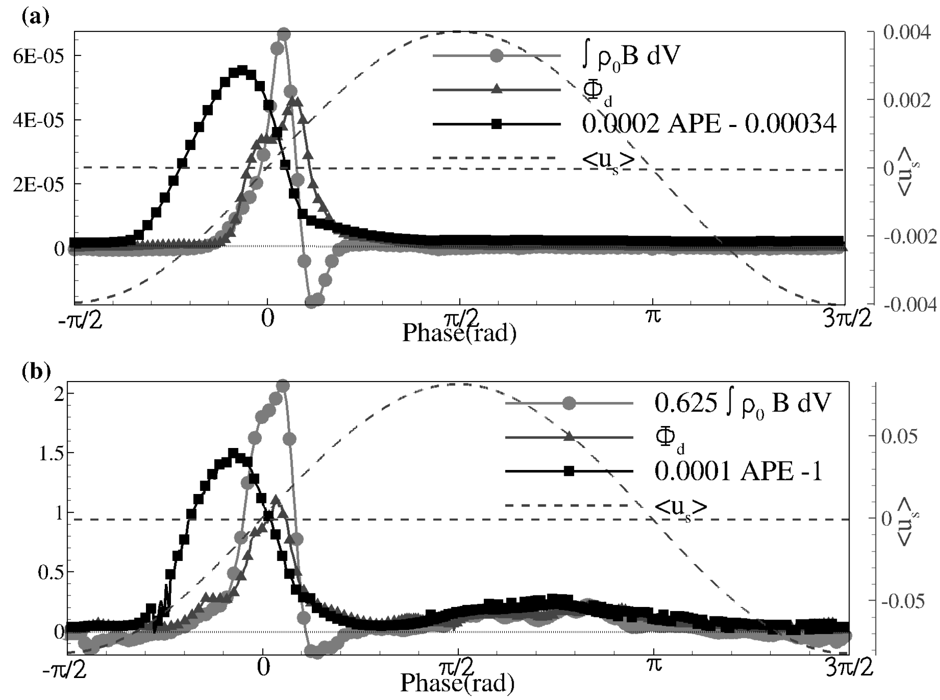

Figure 4.7: Evolution of APE, buoyancy flux, and diapycnal flux (Φ_d). The upper panel corresponds to case 1 and the lower panel to case 2. The dashed line is the depth-averaged streamwise velocity $\langle u_s \rangle$ (m/s). APE has units of kgm^2s^{-2} whereas units of Φ_d and $\int \rho_0 BdV$ are kgm^2s^{-3}

shows 1-d density profiles at various phases during the LCOE. In this case, the density profile at $\phi = -0.15\pi$ exhibits unstable stratification spanning 20 to 60 m above the bottom. The convective overturn breaks down so that, at $\phi = 0.03\pi$, small scale density fluctuations are present all the way from the bottom up to 70 m above bottom, spanning the entire thickness of the bottom flow as was seen in case 1. In contrast to the lower-Re case, the available potential energy and diapycnal flux show some activity in the later half of the cycle as shown in figure 4.7(b). The lower flank of the upslope flow in this larger-scale problem is able to produce overturns (by bringing heavy fluid from depth to overlay lighter fluid) that extend further away from the bottom wall restraint and are more effective in mixing the density field.

4.5 Thorpe Scales

The evolution of the Thorpe scale [1] (L_T) is described and contrasted with that of the Ozmidov scale, $L_O = \sqrt{\varepsilon/N^3}$, in section 4.54.5.1. Simulation data provides the simplification of computing the Thorpe length scale from the mean density profile (obtained by averaging the three dimensional density field in both the horizontal directions). The mean density profile is a function of slope normal coordinate z_s and time. In observational studies, the turbulent dissipation rate is customarily inferred from overturns in instantaneous density profiles obtained at moored or towed profilers. Therefore, the simulation data is used to investigate the behavior of Thorpe scales computed from individual density profiles, i.e., a virtual mooring with infinite vertical profiling speed. Both, mean and instantaneous density profiles lead to the same qualitative result regarding the inability of L_T to serve as a proxy for L_O in the present flow. Thorpe estimates of the turbulent dissipation rate are compared to the actual values in section 4.54.5.2.

To meet the overturn selection criterion, the density gradient is required to be positive over at least four contiguous grid points. The Thorpe displacement for each volume element dV_i within an overturn is defined as $d_i = z_i - z$, where z and z_i are vertical positions of a volume element before and after reordering the density profile. The Thorpe scale, L_T, for each overturn is defined as the root mean square (r.m.s.) of the displacements of each volume element within an overturn,

$$L_T = \sqrt{\frac{\Sigma d_i^2 dV_i}{\Sigma dV_i}}. \tag{4.18}$$

The overturn Ozmidov scale is defined as

$$L_O = \sqrt{\frac{\varepsilon}{\underline{N}^3}}, \tag{4.19}$$

[1]The method used here to compute the Thorpe length scale scale is non-standard. Overturn boundaries are determined as the boundaries of inversions in the density profile. It will be shown that our implementation of the Thorpe estimate substantially overestimates the dissipation of the convective instabilities present in this flow. The standard method leads to a higher value of L_T and, therefore, the overestimate of the turbulent dissipation would have been *even higher* with the standard method.

where $\underline{\varepsilon}$ and $\underline{N}$ are the turbulent dissipation rate and stratification averaged over each overturn.

4.5.1 Evolution of Thorpe length scales

Figure 4.8 shows the distribution of overturns, computed from the mean velocity profile, at four different time instances over the lifetime of a LCOE for case 1. The vertical extent of a single bar corresponds to the overturn height and the horizontal extent corresponds to the Thorpe length scale calculated for that overturn. At phase $\phi = -0.19\pi$, there is a single overturn extending from 1 m above bottom to 4 m above bottom with a Thorpe length scale of $L_T = 1.96$ m. The sequence from figure 4.8 (a)-(d) shows the cascade to small scales: the number of small overturns increases and the Thorpe length scales decrease. At phase $\phi = 0.07\pi$, multiple overturns occur over $z = 0.5$ m to $z = 7$ m with a maximum Thorpe length scale of only 0.17 m. Figure 4.9 is an analogous plot for case 2. At phase $\phi = -0.19\pi$, there is a single large overturn as in case 1 but larger by an order of magnitude ($L_T \simeq 20$ m) that subsequently breaks down into multiple smaller overturns. For both cases 1 and 2, the ratio of Thorpe scale to the overturn height ranges from 0.5 to 0.7 with a mean value of ≈ 0.6.

Instantaneous density profiles at various virtual moorings have also been examined for the evolution of L_T. Similar to the mean density profile, the density profiles at all virtual mooring obtained by sampling the simulation data also show that L_T is large at the beginning of the LCOE and progressively become smaller with a broader distribution as the initially large overturns disintegrate.

We now turn to a comparison of the evolution of Thorpe scales with that of the Ozmidov scales. Figure 4.10(a) shows the time evolution of Thorpe and Ozmidov length scales in case 1. As the flow transitions from peak downslope to near-zero velocity, a large region of unstable density gradient is created resulting in the increase of Thorpe scale ($L_T \approx 2$ m). The Thorpe scale remains nearly constant for a certain fraction of the cycle (about 30 mins) and then disintegrates into multiple small overturns over a finite time (about 90 mins). The Ozmidov scale starts to increase during the disintegration of the large overturn. Ozmidov scales

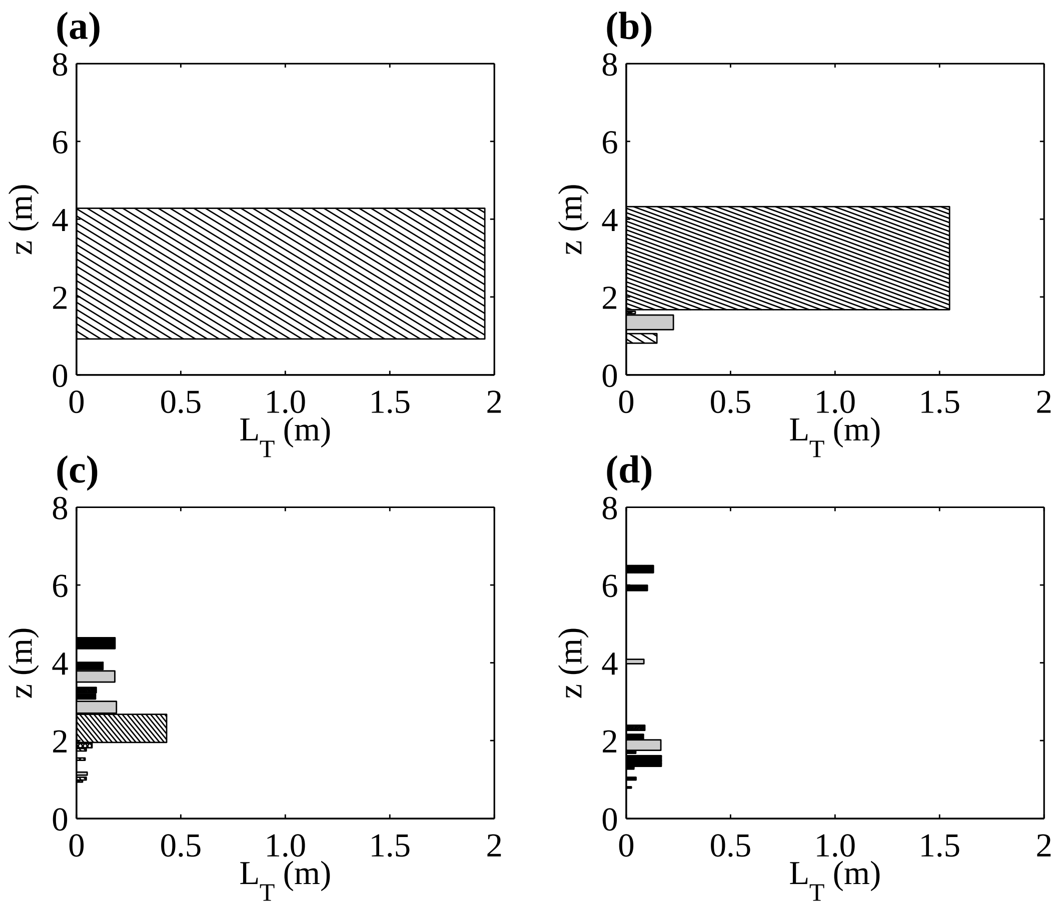

Figure 4.8: Distribution of density overturns along the slope-normal direction is shown at four time instances in case 1 (DNS). Mean density profile is used to detect overturns and compute L_T. Time instances chosen are: (a) -0.19π, (b) -0.13π, (c) -0.01π, (d) 0.07π. Time range is chosen during the flow reversal from down to up-slope. Vertical extent of each bar represents the overturn height and the horizontal extent represents the Thorpe scale calculated for that overturn. Note that the horizontal and vertical coordinates have different scales.

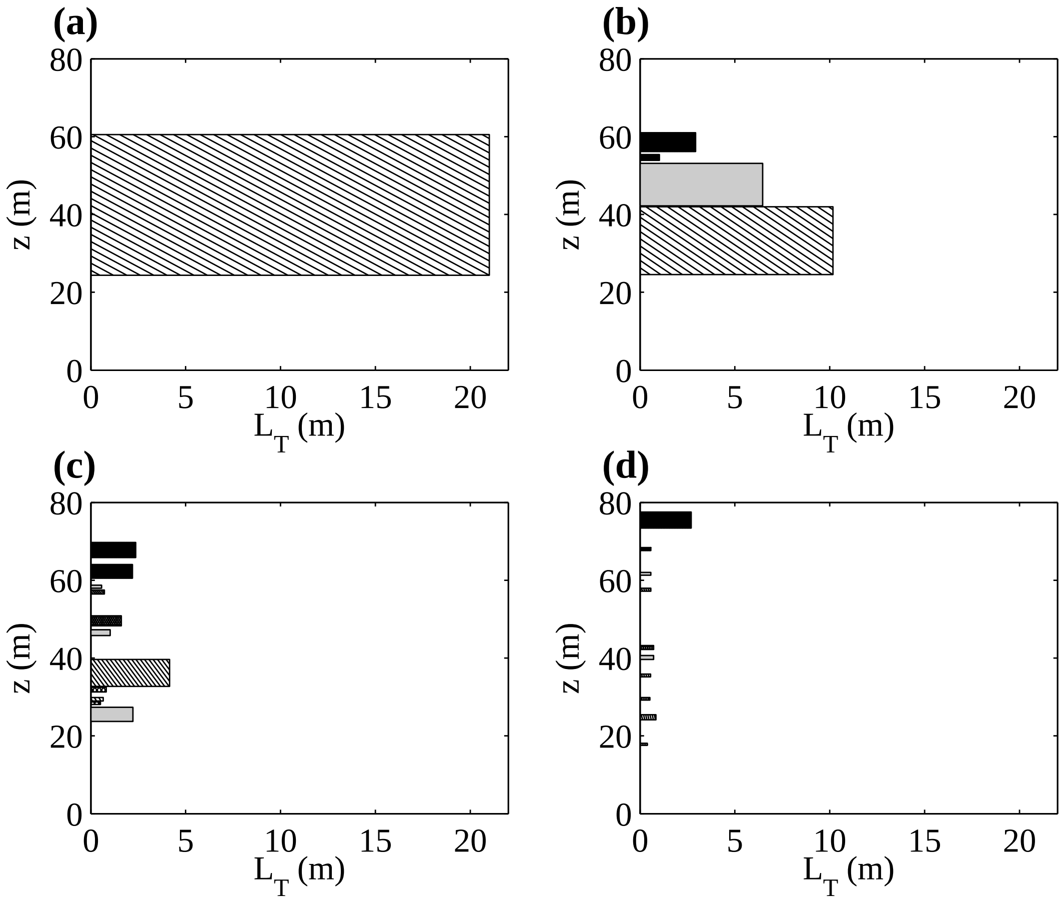

Figure 4.9: Distribution of density overturns in case 2 (LES). Mean density profile is used to detect overturns and compute L_T. Time instances chosen are: (a) -0.19π, (b) -0.12π, (c) -0.02π, (d) 0.06π. Time range is chosen during the flow reversal from down to upslope. Each bar is drawn between the top and bottom of an overturn, and the horizontal extent represents the Thorpe scale calculated for that overturn.

decrease a bit around $\phi = 0.2\pi$, as the turbulence caused by convective overturns decays. L_O starts to increase at around 0.3π due to the increased dissipation caused by enhanced near bottom shear when the peak upslope velocity is large. In contrast, there are no significant overturns at this time and L_T is close to zero. Case 2 with larger l_b, U_b and Re show a similar dependence of the Thorpe and Ozmidov scales on phase in figure 4.10(b). Nevertheless there are two qualitative differences: the range of values taken by L_O show a significantly larger spread in case 2 after the large overturn disintegrates and both L_T and L_O show substantially more activity in case 2 relative to case 1 during the upslope flow (compare part (b) to part (a) of figure 4.10). The bottom panel of figure 4.10 is the analog of the top panel for an individual virtual mooring profile. Similar to the mean profile, the evolution of the Thorpe scales from an individual mooring profile is different from that of the Ozmidov scales and exhibits a similar phase lag. It is interesting to note that Thorpe length scales obtained from the simulation data at an individual location exhibit a wider range of values during the buildup of the LCOE and a longer time interval over which the large overturns disintegrate.

The evolution of Ozmidov and Thorpe scales, employing either mean or single location density profiles, shows that they are *not* linearly related. There is phase lag between their maxima because the Thorpe scale, a measure of overturning length scales, is the largest just prior to breakdown by convective instability, whereas the Ozmidov scale is computed based on the turbulent dissipation which attains its peak value only after there is sufficient time for the cascade to small scales to be established. The instantaneous value of the ratio of Ozmidov to Thorpe scale is found to vary between $\mathcal{O}(0)$ to $\mathcal{O}(100)$ and it is amply evident that L_T cannot be used as proxy for L_0 at the corresponding time in the present flow.

4.5.2 Turbulent dissipation rate inferred from Thorpe scales

The turbulent dissipation rate is estimated from the Thorpe scale by assuming that L_O is proportional to L_T, and the customary choice of $C_d = L_O/L_T = 0.8$

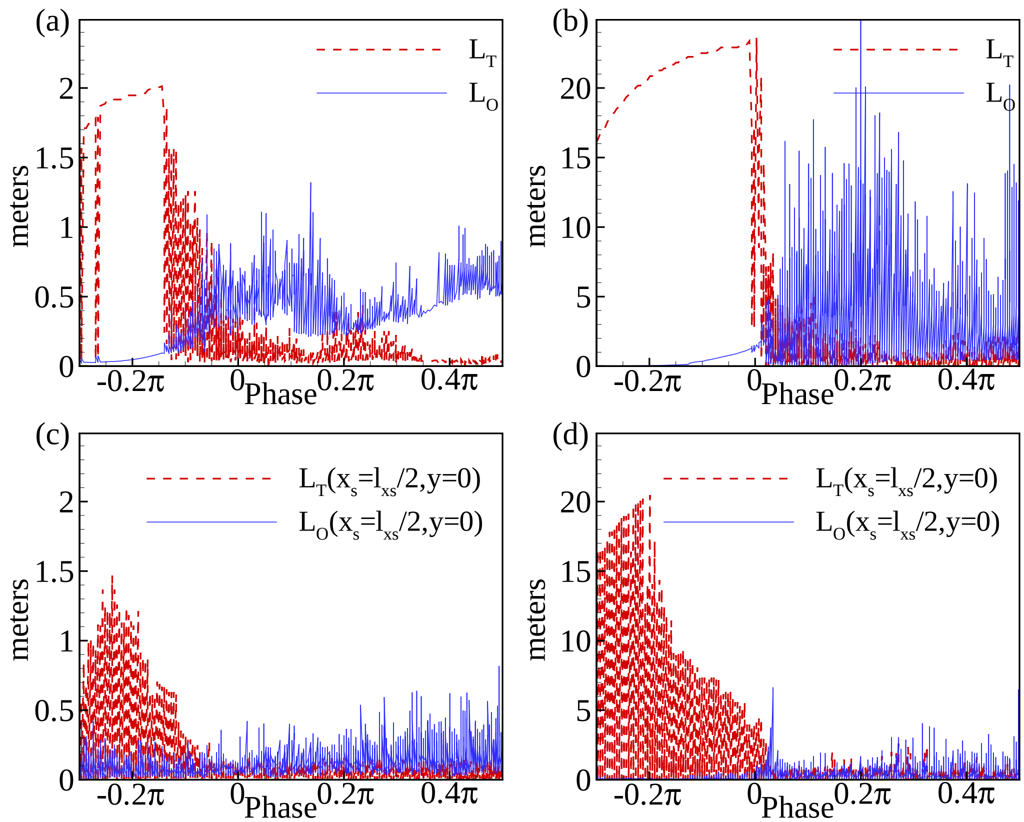

Figure 4.10: Comparison of the phase evolution of Thorpe and Ozmidov scales. Both quantities are multi-valued functions of phase. **Top row**: Panels (a) and (b) show results calculated using the mean density profile for the DNS and LES cases, respectively. **Bottom row**: Panels (c) and (d) show results calculated from the density profile at a single location ($x_s = l_{xs}/2, y = 0$) for DNS and LES cases, respectively.

leads to the following Thorpe dissipation rate estimate,

$$\varepsilon_T = {C_d}^2 {L_T}^2 N^3 = 0.64 {L_T}^2 N^3 \,. \tag{4.20}$$

The depth-averaged value of the actual dissipation rate in the simulation, $\langle \varepsilon_S \rangle_z$, is compared with the depth-averaged value of the Thorpe dissipation rate estimate, $\langle \varepsilon_T \rangle_z$, at the same time. Here,

$$\langle \varepsilon_S \rangle_z \quad = \frac{\int_0^{Z_0} \varepsilon dz_s}{Z_0}, \tag{4.21}$$

$$\langle \varepsilon_T \rangle_z \quad = \frac{\sum_{i=1}^{n_{ovt}} 0.64 \big({L_{T,i}}^2 \underline{N_i}^3 \big) L_{H,i}}{Z_0}. \tag{4.22}$$

Note that the vertical averaging distance is $Z_0 = 8$ m for the DNS case and 80 m for the LES case. Subscript i denotes the i-th overturn and n_{ovt} denotes the number of overturns in the profile.

Figures 4.11(a) and 4.11(b) compares the Thorpe dissipation rate estimated from overturns in the mean density profile with the actual value of turbulent dissipation rate. The phase range shown here is during the LCOE. Initially, when the overturn is large and the stratification is still strong, $\langle \varepsilon_T \rangle_z$ is large. At a later time, when the overturn breaks down into turbulence, $\langle \varepsilon_T \rangle_z$ decreases whereas $\langle \varepsilon_S \rangle_z$ increases. $\langle \varepsilon_S \rangle_z$ peaks at around $\phi = 0.1\pi$ and subsequently exhibits a gradual decrease as as the turbulence decays. The peak value of $\langle \varepsilon_S \rangle_z$ is approximately 6-7 times smaller compared to the peak value of $\langle \varepsilon_T \rangle_z$ inferred from the mean density profile in both DNS and LES cases.

Various locations were considered to calculate the Thorpe dissipation rate from individual density profiles. The variability among the dissipation rate estimates at different locations is small and only two locations ($x_s = l_{xs}/2, y = 0$ and $x_s = l_{xs/2}, y = l_y/2$) are shown as examples. Figures 4.11(c) and 4.11(d) compare $\langle \varepsilon_T \rangle_z$ at these two locations with the actual value for DNS and LES cases, respectively. The phase lag between peak values of $\langle \varepsilon_T \rangle_z$ and $\langle \varepsilon_S \rangle_z$ that was found when using the mean density profile remains when individual density profiles are used.

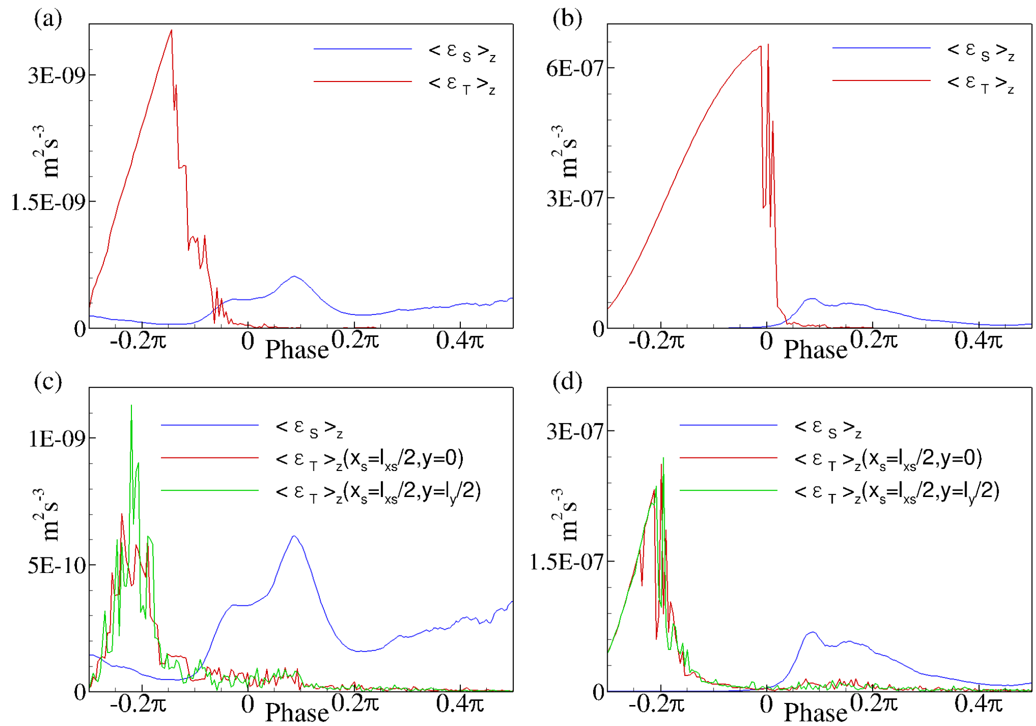

Figure 4.11: The depth-averaged value of turbulent dissipation rate inferred from the Thorpe scales, $\langle \varepsilon_T \rangle_z$, is compared with the actual turbulent dissipation rate in the simulation, $\langle \varepsilon_S \rangle_z$. Both quantities are single-valued functions of phase. **Top row**: Panels (a) and (b) are based on Thorpe length scales detected in the mean density profile for DNS and LES cases, respectively. **Bottom row**: Panels (c) and (d) are based on Thorpe length scales detected in the density profile at two specific locations ($x_s = l_{xs}/2, y = 0$ and $x_s = l_{xs/2}, y = l_y/2$) for DNS and LES cases, respectively.

It is worth noting that $\langle\varepsilon_T\rangle_z$ inferred from the mean density profile has its peak value 3-4 times larger compared with $\langle\varepsilon_T\rangle_z$ inferred at virtual mooring locations. Tracking each overturn obtained from both the mean density profile and virtual mooring profiles suggests that the peak value of L_T is slightly larger and the value of N is noticeably larger for overturns obtained from the mean density profile, resulting in higher peak Thorpe scale dissipation ($\propto {L_T}^2N^3$) inferred from the mean density profile.

The phase evolution of $\langle\varepsilon_T\rangle_z$ and $\langle\varepsilon_S\rangle_z$ show that Thorpe length scales substantially overestimate the dissipation during the initial stages of LCOE and substantially underestimate the dissipation during the later stages of LCOE. In fact, there are time periods when one of the two dissipation values is *near zero* while the other is *substantial*. The cycle-averaged values of the dissipation rate have also been compared and, upon cycle averaging, the actual turbulent dissipation rate is found to be comparable to the value inferred from Thorpe scales for both DNS and LES cases. In the DNS, the cycle-averaged value of the actual dissipation rate is $\langle\varepsilon_S\rangle_z = 1.42 \times 10^{-10}$ m^2/s^3 while the corresponding values of Thorpe dissipation rate are $\langle\varepsilon_T\rangle_z = 1.83 \times 10^{-10}$ m^2/s^3 (from mean density profile) and $\langle\varepsilon_T\rangle_z = 2.85 \times 10^{-11}$ m^2/s^3 (from density profile at a location). The cycle-averaged values in the LES are $\langle\varepsilon_S\rangle_z = 1.36 \times 10^{-8}$ m^2/s^3, $\langle\varepsilon_T\rangle_z = 6.54 \times 10^{-8}$ m^2/s^3 (from mean density profile) and $\langle\varepsilon_T\rangle_z = 1.10 \times 10^{-8}$ m^2/s^3 (from density profile at a location).

Recall that a modeling coefficient, C_d, appears in the Thorpe dissipation rate estimate, Eq. (4.20). From the preceding results, it is clear that C_d at a given time is generally not a O(1) coefficient. The simulation data is examined to assess if O(1) values of C_d may apply in an *"average"* sense over parts of the cycle. To do so, we define

$$C_\phi = \sqrt{\frac{\langle\varepsilon_S\rangle_{z\phi}}{\langle\varepsilon_T\rangle_{z\phi}/0.64}} \tag{4.23}$$

Here, $\langle\ \rangle_{z\phi}$ represents depth averaging followed by phase averaging. The value of the dissipation coefficient C_ϕ, which indirectly represents an average value of L_O to L_T during the flow evolution, depends on the phase range over which averaging is done and may be less than or greater than unity.

Values of C_ϕ for two choices of the length of phase averaging (ϕ varying from $-\pi/2$ to $3\pi/2$ spanning the entire wave cycle and a shorter interval spanning the LCOE) are shown in tables 4.2 and 4.3. C_ϕ, computed as an average over the entire cycle, has values of 0.7 and 1.78 for the mean density profile and virtual mooring profile, respectively, in the DNS case; corresponding values for the LES case are 0.36 and 0.88, respectively. The O(1) value of the phase-averaged estimate of the dissipation coefficient, C_ϕ, found in this study is not a mere coincidence. It can be explained on the basis of available potential energy as given below. As was described earlier in section 4 of this paper, available potential energy is the primary source of eventual turbulence and dissipation during the convective instability and its subsequent nonlinear evolution. The available potential energy of an overturn is

$$APE \quad \propto \quad \Delta\rho g L_T \quad \propto \quad g\frac{d\rho}{dz}{L_T}^2 \propto \underline{N}^2 {L_T}^2 \,, \tag{4.24}$$

where the density difference over an overturn $\Delta\rho$ is taken to be proportional to the product of the Thorpe displacement and the sorted density gradient of that overturn and $\underline{N}$ corresponds to the average background stratification (after sorting) of that overturn. The characteristic time scale of the overturn is given by

$$\sqrt{\frac{L_T}{g'}} = \frac{1}{\underline{N}} \,, \tag{4.25}$$

where $g' = (\Delta\rho/\rho_0)g$ is the reduced gravity. Thus, energy is released at the rate of $APE \times N$. Over the duration of the convective event, a substantial fraction of the APE cascades to turbulence to be eventually dissipated by molecular effects so that over the entire cycle,

$$\langle \varepsilon_S \rangle \propto \langle APE \times \underline{N} \rangle \propto \langle {L_T}^2 \underline{N}^3 \rangle. \tag{4.26}$$

Thus,

$$C_\phi = \sqrt{\frac{\langle \varepsilon_S \rangle_{z\phi}}{\langle {L_T}^2 \underline{N}^3 \rangle_{z\phi}}} = O(1)\,. \tag{4.27}$$

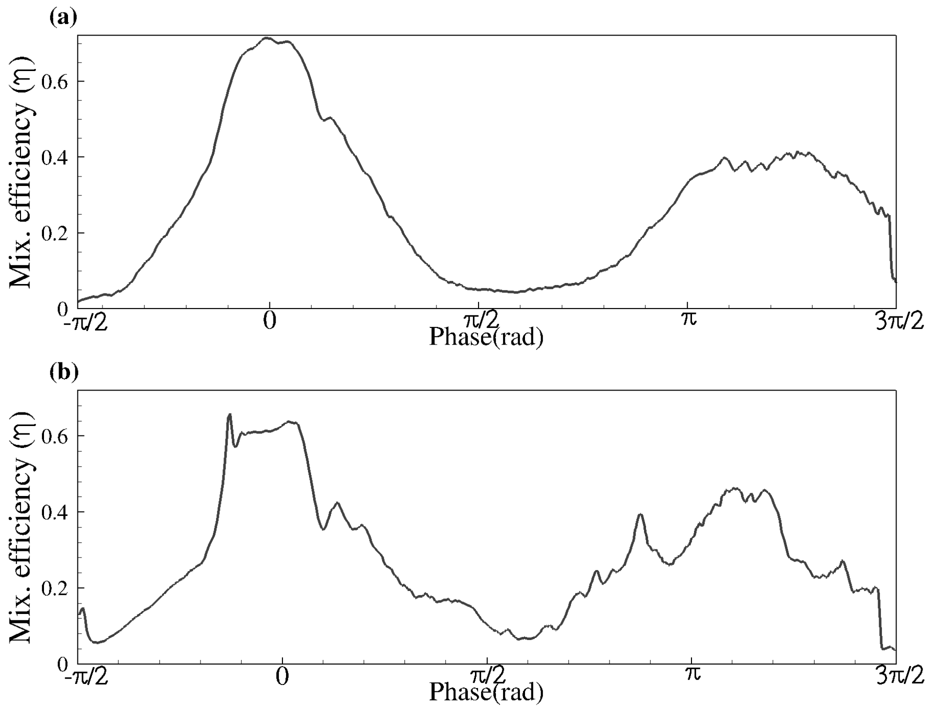

Figure 4.12: Evolution of instantaneous mixing efficiency $\eta(t)$ as defined by equation (4.28): (a) case 1 (DNS), (b) case 2 (LES).

4.6 Mixing Efficiency

The instantaneous and phase averaged mixing efficiencies are as follows:

$$\eta(t) = \frac{\Phi_d}{\Phi_d + \int_0^{Z_0} \varepsilon_V \, dz_s} \tag{4.28}$$

$$\langle \eta \rangle_\phi = \frac{\int_{t1}^{t2} \Phi_d dt}{\int_{t1}^{t2} \left(\Phi_d + \int_0^{Z_0} \varepsilon_V \, dz_s \right) dt} \tag{4.29}$$

where Φ_d is the irreversible diapycnal flux integrated over the volume defined by $V = l_{xs} l_y Z_0$, $\varepsilon_V = \rho_0 l_{xs} l_y \varepsilon$. For case 1, $Z_0 = 8$ m and for case 2, $Z_0 = 80$ m. Z_0 is the height up to which turbulent fluctuations are observed during a tidal cycle. Figure 4.12 shows the time evolution of mixing efficiency for both cases 1 and 2. Mixing efficiency starts with a small value at peak downslope flow. For case 1, mixing efficiency increases with time during the first quarter of the cycle and reaches its peak slightly before the irreversible diapycnal flux has its maximum value. At a later time, mixing efficiency drops gradually to near-zero value. It starts to increase again at $\phi = 0.7\pi$ until $\phi \approx 1.3\pi$. The TKE budget during the second half of the cycle exhibits little turbulent dissipation or diapycnal flux, the mixing efficiency during this part of the cycle increases because ε become smaller than Φ_d. Mixing efficiency averaged over various fractions of a tidal cycle is shown in tables 4.2 and 4.3. Mixing efficiency averaged over the LCOE ranges between $0.4 - 0.5$, which is *substantially higher* than the commonly used value of 0.2 in both DNS and LES cases. This agrees well with the mixing efficiency computed in previous studies (Dalziel *et al.* (2008);Gayen & Sarkar (2013)) of turbulence driven by convective instability. The cycle averaged mixing efficiency ranges between $0.3 - 0.4$ in both the cases, this value is also high compared to the value of 0.2 used to estimate diapycnal diffusivity from turbulent dissipation rate.

4.7 Diffusivity

Quantification of mixing, i.e., estimation of diapycnal diffusivity needs a good understanding of the details of the turbulent event. The standard method of estimating the diffusivity from turbulent dissipation rate (usually an inferred value) is $K_\rho = 0.2\varepsilon/N^2$. This model had been derived making two important assumptions: (1) The mixing efficiency is 0.2 and constant throughout the turbulent event, and (2) Turbulence is a quasi-steady state process so that the turbulent dissipation is balanced by the sum of turbulent production and buoyancy flux. Neither of these assumptions is correct in the present flow. Analysis of the TKE and scalar variance budgets in the previous sections of this paper reveal that the tendency term can be significant compared to the other terms during the tidal cycle. Also, assuming a constant value of 0.2 for mixing efficiency during the LCOE is a substantial underestimate.

We calculate the diapycnal diffusivity following Barry *et al.* (2001) who derived a formula to calculate the diapycnal diffusivity based on diapycnal flux Φ_d and the density gradient averaged over the volume. Phase averaged diapycnal

Table 4.2: Key results for Case1 (DNS) having bottom flow with peak velocity $U_b = 0.0125$ m/s and width $l_b = 6$ m. First row corresponds to results obtained by averaging over the large convective overturning event (LCOE) that spans the phase range $(-0.3\pi, 0.4\pi)$ and the second row to averaging over the entire cycle $(-0.5\pi, 1.5\pi)$. C_ϕ is the dissipation coefficient defined in (4.23), $\langle\eta\rangle_\phi$ is the phase averaged mixing efficiency and $\langle K_\rho\rangle_\phi$ is the phase averaged diapycnal diffusivity.

Averaging period (ϕ)	C_ϕ(mean)	C_ϕ(mooring)	$\langle\eta\rangle_\phi$	$\langle K_\rho\rangle_\phi$ (m^2/s)
$(-0.3\pi, 0.4\pi)$	0.5	1.17	0.55	9.3×10^{-5}
$(-0.5\pi, 1.5\pi)$	0.7	1.78	0.4	3.7×10^{-5}

Table 4.3: Key results for Case 2 (LES) having bottom flow with peak velocity $U_b = 0.125$ m/s and width $l_b = 60$ m. Quantities defined as in Table 2.

Averaging period (ϕ)	C_ϕ(mean)	C_ϕ(mooring)	$\langle\eta\rangle_\phi$	$\langle K_\rho\rangle_\phi$ (m^2/s)
$(-0.3\pi, 0.4\pi)$	0.27	0.66	0.39	2.1×10^{-3}
$(-0.5\pi, 1.5\pi)$	0.36	0.88	0.31	2.0×10^{-3}

diffusivity is given by,

$$\langle K_\rho\rangle_\phi = \frac{\langle\Phi_d\rangle_\phi}{Vg(d\rho/dz)_{average}}. \tag{4.30}$$

Here, V is the volume of the fluid and $(d\rho/dz)_{average}$ is the density gradient averaged over volume and phase. $\langle K_\rho\rangle_\phi$ calculated over various fractions of a cycle is shown in tables 4.2 and 4.3. The diffusivity averaged over the large convective overturning event is high in both cases 1 and 2 when compared with the overall cycle averaged value. The diffusivity averaged over the entire wave period is two orders of magnitude higher in case 2 when compared with case 1, consistent with an inertial scaling of $\approx U_b l_b$. It is also worth noting that the diffusivity in the high-Re case is 2×10^{-3} m^2/s , which is almost 4 orders of magnitude larger than the molecular diffusivity.

4.8 Conclusions

Mixing during near-bottom convective overturns driven by internal tides is investigated with a detailed analysis of scalar mixing and turbulent dissipation rate in an oscillatory, baroclinic boundary flow. During downslope flow, light fluid from above replaces heavier fluid resulting in the formation of an unstable density gradient detached from the viscous boundary layer. The available potential energy (APE) continues to increase until the large overturn breaks up into multiple small overturns via three-dimensional convective instability during flow reversal from down to upslope. The overturn height in this large convective overturn event (LCOE) scales with the thickness l_b of the boundary flow. In the case with a small $l_b = 6$ m that is amenable to DNS, the tallest overturn has a height of 3 m with the corresponding Thorpe length scale close to 2 m. For the case with $l_b = 60$ m computed with LES, the tallest overturn has a height of 35 m with the corresponding Thorpe scale of 20 m. There is substantial energy transfer from available potential energy (APE) to the turbulent kinetic energy (TKE) through the fluctuating buoyancy flux and the shear production of turbulence is small during the LCOE.

It is found that there is a substantial phase lag between the Thorpe and Ozmidov length scales during the evolution of the convective overturning event. Thorpe scales are maximum during the initial stages of the convective instability but the Ozmidov scale is small. At a later time, when three dimensional turbulence and dissipation become prominent leading to an increase of the Ozmidov sale, the overturns are smaller and are spread over the most of the water column involved in the boundary flow. In brief, when L_T decreases, L_O increases. The simulations show that Ozmidov, L_O, and Thorpe length scales, L_T, are different functions of the tidal phase and L_T cannot serve as a proxy for L_O at that time. Our result is consistent with Smyth & Moum (2000) who, in the case of shear-driven stratified turbulence, found that $R_{OT} = L_O/L_T$ varies from $\mathcal{O}(0.1)$ during the initial large-overturn stage to $\mathcal{O}(1)$ during the later stage of well-developed broadband turbulence. The present case of convectively driven turbulence shows one to two orders of magnitude increase in R_{OT} during the course of LCOE in both DNS and LES cases.

Turbulent dissipation rate estimated from Thorpe scales using mean density profile and individual density profiles (virtual mooring) is compared with the actual dissipation rate computed from the simulation data. It is found that Thorpe length scales overestimate the dissipation by more than an order of magnitude during the initial stages of the overturning event and underestimates the dissipation, again by more than an order of magnitude, during the later stages. It is not possible to obtain a reliable estimate of turbulent dissipation rate at a given time by measuring overturns at that time. However, their cycle-averaged values are comparable. This is manifested in the form of the *cycle-averaged* dissipation coefficient C_ϕ (usually taken to be 0.8), being $\mathcal{O}(1)$ in both DNS and LES cases. This $\mathcal{O}(1)$ value of cycle-averaged C_ϕ is explained based on available potential energy of the large convective overturns cascading to turbulence and molecular dissipation over a cycle. Thus, it may be possible to average the turbulent dissipation obtained by Thorpe analysis of an ensemble of density profiles during an *entire* wave period to approximate the cycle-averaged dissipation rate. Similarly, Thorpe analysis over the *entire* lifetime of a LCOE could give the average dissipation associated with the LCOE. A single value of buoyancy frequency N ($\sim 10^{-3}$ rad/s), representative of deep ocean stratification, is considered in this study. Varying the buoyancy frequency may have an effect on the formation and detailed characteristics of convective instabilities. However, once a convective instability is formed, the fundamental argument made in this paper that the Thorpe scale L_T is not linearly related to the Ozmidov scale L_O at the same time is expected to be valid, independent of the precise value of N.

The instantaneous mixing efficiency η, during the convective mixing event has its peak value close to 0.7 in DNS and 0.6 in LES. The cycle-averaged mixing efficiency of 0.3-0.4 is also substantially larger than the commonly assumed value of 0.2. High mixing efficiencies close to 0.5 have been reported (Dalziel *et al.*, 2008; Lawrie & Dalziel, 2011; Gayen & Sarkar, 2013) in situations where turbulence is driven by convective instability. A recent experimental study (Wykes & Dalziel, 2014) reported that mixing efficiency can be as high as 0.75 when the unstable density region is confined within a stable stratification from above and below, a configuration that occurs here (figures 4.5(c) and 4.6(c)) during the flow reversal mixing phase.

Thus, it is important that the mechanism leading to turbulence (e.g. shear instability or convective instability) needs to be established before choosing a value for η to infer mixing rates. The volume averaged diffusivity varies by two orders of magnitude between DNS and LES cases, following an inertial scaling of turbulent diffusivity: $K_\rho \propto U_b l_b$. The tidally-modulated enhanced diffusivity of $\mathcal{O}(10^{-3}$ m^2/s) that we find here for the high-Re case is consistent with enhanced values of bottom diffusivity found near rough topography.

It is encouraging that DNS of this problem of tidally-modulated, bottom-intensified boundary flow that occurs at near-critical slopes and LES of a scaled up version give consistent results regarding the mixing efficiency and Thorpe/Ozmidov scales. Nevertheless, other scenarios of tidally driven turbulence near topography, e.g. breaking lee waves and downslope jets, remain to be explored to examine the generality of the results obtained here.

4.9 Acknowledgements

The contents of this chapter is published in Journal of Physical Oceanography (2015), coauthored by Professor Sutanu Sarkar. V. K. Chalamalla, & S. Sarkar (2015) Mixing, dissipation rate, and their overturn-based estimates in a near-bottom turbulent flow driven by internal tides., *Journal of Physical Oceanography*, *45*, 1969–1987.

Chapter 5

Multi-scale modeling of internal tide generation

5.1 Introduction

Due to the large variation of scales ranging from $\mathcal{O}$ (km) down to $\mathcal{O}$ (cm), simulations of oceanic internal tides that resolve the complete range of spatial and temporal scales are well beyond our current capability. Understanding and quantifying the effect of small scale turbulence and mixing on the large scale flow evolution is important in the context of ocean circulation. We propose a multi-scale simulation approach to utilize the Stratified Ocean Model with Adaptive Refinement (SOMAR) for large scale flow evolution coupled with Large Eddy Simulation to model the small scale turbulence and mixing. SOMAR has been designed to handle high anisotropy in the grid (via a leptic Poisson solver, Santilli & Scotti (2011)), which is necessary to efficiently handle scale-anisotropy of high mode internal waves.

5.2 SOMAR-LES

Stratified Ocean Model with Adaptive Refinement (SOMAR) is a computational framework (Santilli & Scotti, 2015) developed by Ed Santilli as part of

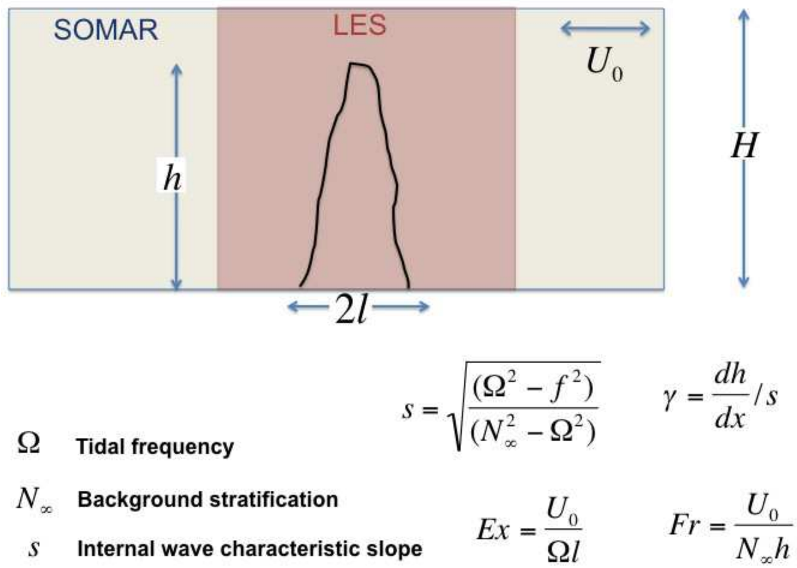

Figure 5.1: Schematic of SOMAR-LES simulation. Outer box represent SOMAR computational domain. The red colored rectangular box closer to the ridge represent the LES computational domain.

his Ph.D. thesis at University of North Carolina, Chapel Hill. It is suitable for modeling oceanic flows where the scales of motion can be highly variable in both space and time. Its feature of local adaptive mesh refinement efficiently captures regions of enhanced shear or local overturning, refines the grid in those regions, and thus allows the reduction of computational cost drastically when compared to single-grid simulations. Oceanic flows, e.g, low-mode internal waves are marked by high anisotropy which SOMAR can efficiently handle with the help of an additional feature, a leptic solver.

SOMAR solves the Navier-Stokes equations under the Boussinesq approximation in a curvilinear coordinate system. Adaptive mesh refinement is a method of refining the grid locally making it more finely spaced in some regions. The grid refinement regions are identified based on the flow physics of the problem. For example, in test cases that we have considered so far: vorticity, Richardson number and velocity gradients are considered in identifying the cells which need to be tagged for refinement. Details of the SOMAR time stepping algorithm are presented in the appendix of this chapter. The ratio of the fine grid spacing to the coarse grid spacing and the number of refinement levels are some of the important decisions that the user needs to make before starting a simulation, based on a general idea of flow physics and the specific goal of the simulation. This method saves computational cost by efficiently refining the grids only in the regions that are necessary.

5.2.1 One-way Coupled Model

In the present study, we developed a framework for one-way coupling between SOMAR and LES. The DNS/LES computational model (Gayen & Sarkar, 2011a) is an in-house code developed by Dr. Bishakhdatta Gayen for sloping topography as part of his Ph.D. thesis which, in turn, is based on the model (Taylor & Sarkar, 2008) for flat-bottom flows developed by Dr. John Taylor as part of his Ph.D. thesis. SOMAR solves the Navier-Stokes equations on a coarser grid (when compared to LES), and the grid spacing is not sufficient to resolve turbulence. LES with a finer grid is nested within the SOMAR computational domain near the region of interest. SOMAR solves the Navier-Stokes equations, taken as two-dimensional here, on the outer coarse grid and, simultaneously, the LES model solves Navier-Stokes equations in a three-dimensional box on the nested fine grid. The schematic for SOMAR+LES simulation is shown in figure 5.1. The time stepping on both are performed simultaneously and they communicate with each other at every time step. In the one-way nesting that we perform here, feedback is provided to SOMAR from LES in the form of eddy viscosity and diffusivity, however no feedback is provided to LES from the outer SOMAR grid. This technique is appropriate for the present problem because the LES model is forced with the barotropic tide and does not require any additional forcing from the parent SOMAR grid. Details about the coupling technique are as follows:
SOMAR-LES time stepping:

1. SOMAR is initialized with zero velocity and density deviation on coarser base grid.

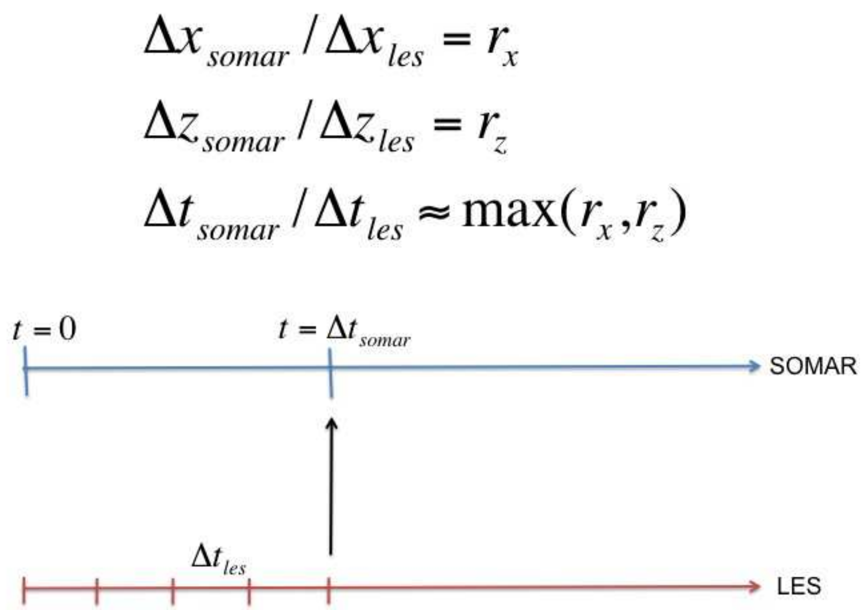

Figure 5.2: Schematic showing the time stepping in SOMAR-LES algorithm.

2. SOMAR creates a refinel level with finer grid ($\Delta x_{somar} = r_x \Delta x_{les}$, $\Delta z_{somar} = r_z \Delta z_{les}$). Here, r_x, r_z are the refinement ratios specified through the input file. The refined level (LES) in the present study is shown in figure 5.1.

3. LES model is initialized with the finer grid, and an additional direction is added (span-wise) to LES with uniform grid spacing.

4. Both SOMAR and LES are forced with an oscillating barotropic tide with a given velocity amplitude and frequency.

5. SOMAR completes its time step and then LES starts its time advancement with smaller time steps compared to SOMAR, see figure 5.2.

6. SOMAR and LES communicate after LES advances through the time interval Δt_{SOMAR}. The eddy viscosity and diffusivity obtained from the LES model, which are functions of phase and space, are communicated to SOMAR and averaged back on the SOMAR grid.

5.3 Tidal flow past model Kaena ridge

Observations and numerical studies as part of HOME (Hawaiian Ocean Mixing Experiment) have found large overturns associated with enhanced dissipation near the top of the ridge (Aucan *et al.*, 2006; Levine & Boyd, 2006; Klymak *et al.*, 2008; Legg & Klymak, 2008). However, there still seems to be no agreement regarding the fraction of energy dissipated locally, due to the lack of resolution in both observations and numerical simulations. So far, we have performed four simulations with a combination of SOMAR, SOMAR-LES and scaled-down LES. The first experiment is a two-dimensional numerical simulation using SOMAR on a single level grid. The second case is a coupled SOMAR-LES simulation, where SOMAR and LES are time advanced together on coarser and finer grids, respectively. SOMAR is run in 2D mode and LES is run in 3D mode allowing the overturns to break down into small scale turbulence, unlike in two dimensional simulations where the flow is not allowed to evolve in the third direction. The horizontal extent of the SOMAR computational domain is much larger compared to the LES domain. The LES domain is designed keeping in mind that recent studies have found turbulence and nonlinear phenomena close to the ridge. The LES box is nested within the SOMAR domain with four times finer horizontal resolution compared to the outer SOMAR grid. Vertical grid resolution is same in both SOMAR and LES. Cases 3 and 4 are large eddy simulations performed on a 100 times scaled down geometry which provide higher resolution of turbulence. All the non-dimensional parameters remain same among cases 1, 2 and 3. In case 4, earth's rotation is included, which results in an increase in the steepness parameter.

Dimensional parameters of the simulations are given in table 5.1. U_0 is the tidal velocity amplitude, N_∞ is the background bottom stratification, Ω is the tidal forcing frequency, and l is the half-width of the topography. Topographic steepness is $\gamma = \frac{dh}{dx}/s$, where $s = [(\Omega^2 - f^2)/(N^2 - \Omega^2)]^{1/2}$ is the slope of the internal tide characteristic. The Excursion number is $Ex = U_0/(l\Omega)$ and the Froude number is $Fr = U_0/(N_\infty h)$, where h is the height of the topography. The Stokes boundary layer thickness is $\delta_s = \sqrt{2\nu/\Omega}$, and the Reynolds number is $Re_s = U_0\delta_s/\nu$.

The primary goal of these set of simulations is to demonstrate the advantages of running a coupled SOMAR-LES model. The effect of small scale turbulence on the evolution of large scale flow will be the focus of this study, along with the quantification of local dissipation. Case 1 is performed on the SOMAR base level coarse grid, it does not have a sub-grid scale model and thus it does not resolve turbulence. On the other hand, in case 2, LES provides the eddy viscosity and diffusivity calculated from the sub-grid scale model to SOMAR at every time step. Comparison of radiated wave flux between cases 1 and 2 demonstrates the effect of the small-scale turbulence represented in terms of eddy viscosity and diffusivity obtained from the LES. We expect the scaled down LES simulations to be most accurate among all the simulations performed in this study. The base grid SOMAR simulation (case1) and coupled SOMAR-LES simulation (case2) will be compared against the benchmark of scaled-down LES simulation (case 3). The simulation data will be examined to understand turbulent mechanisms and compare with previous observations and numerical simulations of flow near the Hawaiian ridge. Also, the complete baroclinic energy budget will be quantified to estimate the fraction of energy conversion to internal tides that is dissipated locally. The modal structure of the internal wave field will also be determined, since it is important to get an estimate of the energy in low mode waves as they propagate long distances before dissipating at remote locations by interacting with isolated topography or continental slope/shelf.

Figure 5.3 shows horizontal velocity field from the SOMAR coarse level simulation which corresponds to case 1 shown in table 5.1. Velocity snapshots are shown at three different time instances (a) t = 1.85T, (b) t = 2.0T and (c) t = 2.12T respectively. Both high mode and low mode waves can be seen at all time instances, with high mode waves propagating vertically and low mode waves propagating horizontally away from the topography. High mode waves are found to emanate from the critical region (where slope angle matches with the internal waves characteristic slope) of the topography and traverse vertically in both upward and downward directions. The upward propagating wave interacts with the pycnocline, undergoes refraction and finally reflects back from the top surface as evident in the upper 300 m of the velocity snapshots shown in figure

(a)

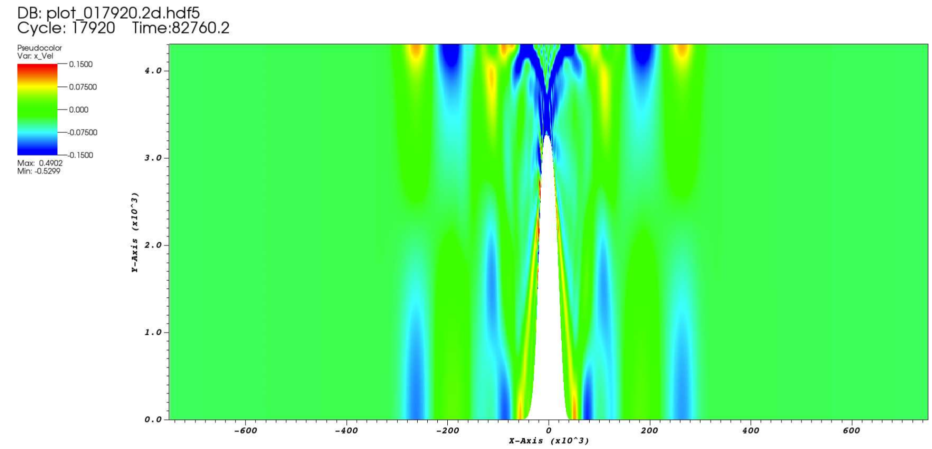

(b)

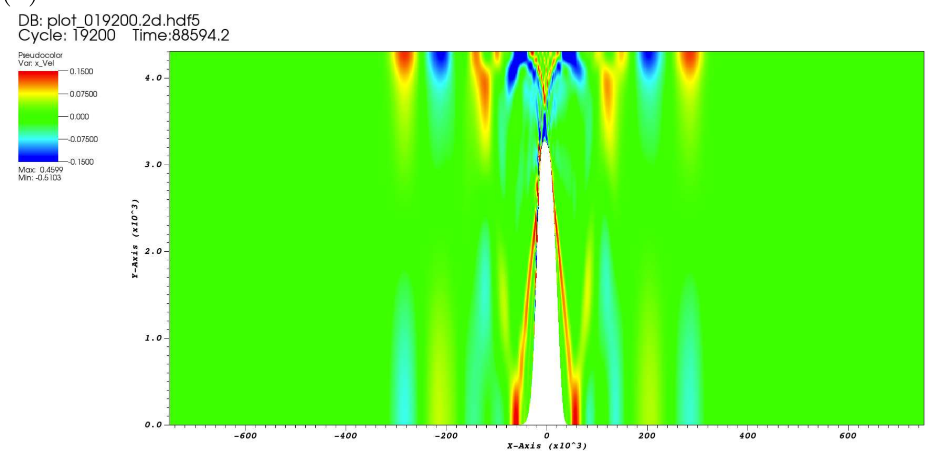

(c)

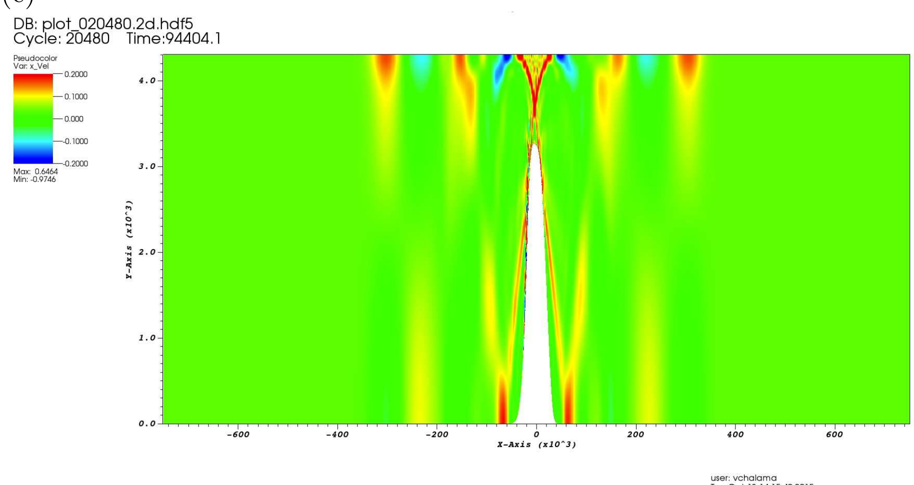

Figure 5.3: Horizontal velocity field of tidal flow past Kaena ridge at time (a) $t \approx 1.85T$, (b) $t \approx 2.0T$, (c) $t \approx 2.12T$. High mode internal waves are generated near the critical region of the ridge and propagate vertically and, at the same, time low mode waves propagate horizontally. Low mode waves propagate faster, since they have higher phase speeds compared to the high mode waves.

Table 5.1: Dimensional parameters for simulations of model Kaena ridge. The kinematic viscosity $\nu = 10^{-5}$ m^2/s for cases 1,2 and 3 and $\nu = 2 \times 10^{-5}$ m^2/s for case 4. Prandtl number $Pr = 7$ for all cases.

$Case$	$U_0(m/s)$	γ	$N_\infty(s^{-1})(deep)$	$\Omega(s^{-1})$	$f(s^{-1})$	h (m)	Remark
1	0.05	3.3	0.0024	0.000141	0.0	3300	SOMAR
2	0.05	3.3	0.0024	0.000141	0.0	3300	SOMAR-LES
3	0.05	3.3	0.24	0.0141	0.0	33	Scaled-down LES
4	0.05	4	0.24	0.0141	0.008	33	Scaled-down LES

Table 5.2: Non-dimensional parameters for simulations of Kaena ridge.

$Case$	Ex	Fr	Re_s	Remark
1	0.011	0.006	1883	SOMAR
2	0.011	0.006	1883	SOMAR-LES
3	0.011	0.006	188	Scaled-down LES
4	0.011	0.006	133	Scaled-down LES

Table 5.3: Grid parameters

$Case$	$dx_{min}(m)$	$dy(m)$	$dz_{min}(m)$	LX (m)	LY (m)	LZ (m)	Remark
1	70	-	2.6	750,000	-	4300	SOMAR
2-SOMAR	70	-	2.6	750,000	-	4300	SOMAR-LES
2-LES	17.5	39	2.6	344,000	2500	4300	SOMAR-LES
3	1	0.39	0.026	2470	25	43	scaled-down LES
4	0.8	0.23	0.019	3990	15	43	scaled-down LES

5.3. The downward propagating high mode wave reflects back from the bottom (at $x \approx \pm 70$ m) before interacting with the low mode wave near the upper surface ($x \approx \pm 140$ m).

Figure 5.4 shows spanwise averaged horizontal velocity field from the higher-resolution LES simulation (case 3) at two different time instances (a) t = 1.25T, (b) t = 1.75T. Figures 5.5,5.6 and 5.7 shows the evolution of w_{rms} field for case 3. The turbulence is mainly seen during flow reversal from down to upslope due to convective overturns near the critical slope region and due to the lee wave breaking that is found near the ridge crest as shown in figure 5.6. Figure 5.8 shows density contours at t = 1.12T for cases 1 and 2 respectively. Case 2, which is a coupled

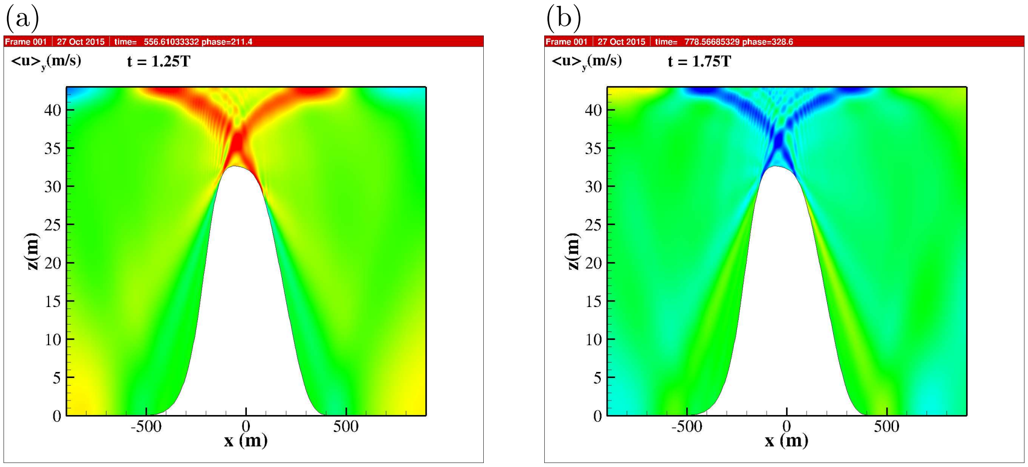

Figure 5.4: Horizontal velocity field of tidal flow past model Kaena ridge in a 100 times scaled down domain: (a) $t \approx 1.25T$, (b) $t \approx 1.75T$.

model with eddy viscosity and diffusivity communicated to SOMAR from LES, shows more small scale features near the overturning region (comparing figures 5.8(a) and 5.8(b)).

In order to quantify the energy conversion from barotropic to baroclinic motions, the velocity field is split into different components including barotropic, baroclinic and a three-dimensional fluctuation field as given below:

$$u(x,y,z,t) = U + u_{bc} + u'$$
$$w(x,y,z,t) = W + w_{bc} + w'\,.$$

Similarly, pressure is decomposed as $p^* = P^* + p_{bc} + p'$ where p^* stands for the deviation from hydrostatic pressure. U, P^*, W are the barotropic components, where U, P^* are calculated by depth averaging u and p^* respectively, and the vertical barotropic component is given by $W(z) = -\frac{\partial}{\partial x}([z - h(x)]\,U)$. The terms u_{bc}, w_{bc} and p_{bc} are baroclinic components.

The baroclinic energy without diffusive fluxes is given by the following equation (Kang, 2010; Kang & Fringer, 2012; Rapaka *et al.*, 2013; Jalali *et al.*, 2014)

$$\frac{\partial}{\partial t}(\overline{E_k} + \overline{E_p}) + \nabla \cdot \overline{\mathbf{F}} = \overline{C} - \overline{\varepsilon}_{bc} - \bar{P} \tag{5.1}$$

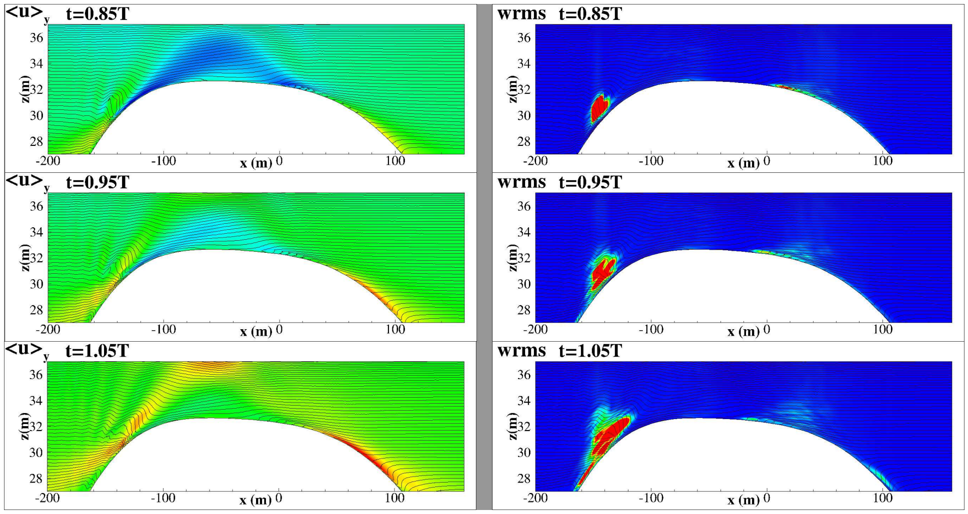

Figure 5.5: Left panel show horizontal velocity field averaged in the span-wise direction at different time instances. Similarly, right panel shows vertical rms velocity field at different time instances

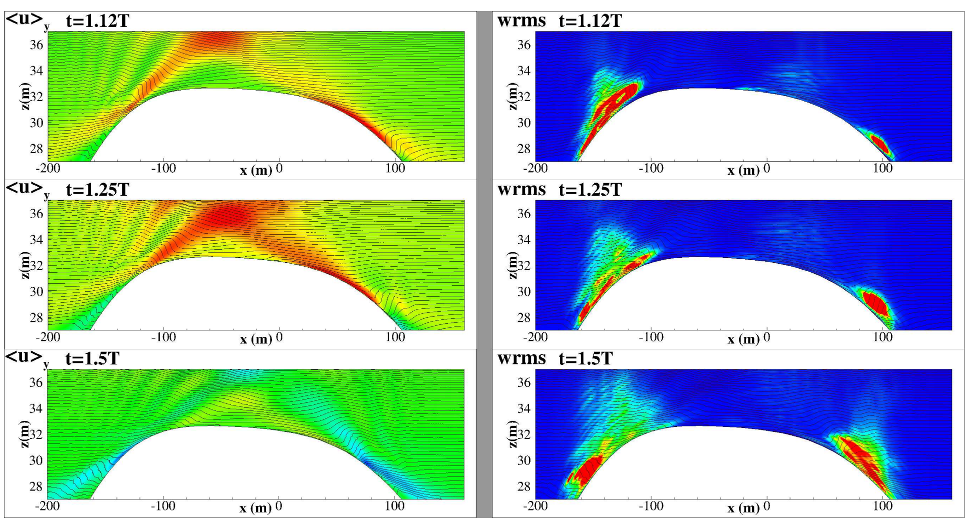

Figure 5.6: Left panel show horizontal velocity field averaged in the span-wise direction at different time instances. Similarly, right panel shows vertical rms velocity field at different time instances

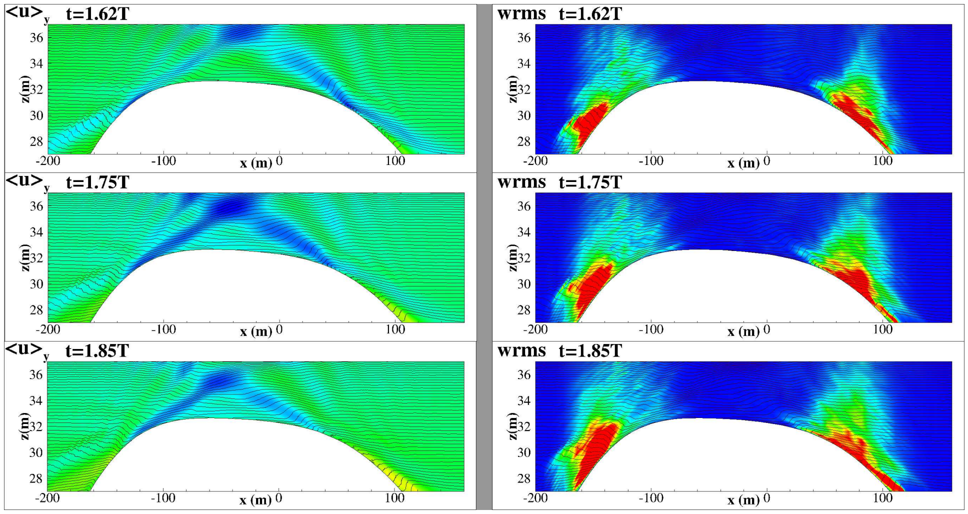

Figure 5.7: Left panel show horizontal velocity field averaged in the span-wise direction at different time instances. Similarly, right panel shows vertical rms velocity field at different time instances

Each term in the above equation is given below:

Unsteadiness	$\dfrac{\partial}{\partial t}(\overline{E_k} + \overline{E_p})$
Pressure Flux (M)	$\nabla_H.(\overline{\boldsymbol{u_{bc\,H}}\, p^*})$
Advection Flux (M_{adv})	$\nabla_H.(\,\overline{\boldsymbol{u_H}(E_p + E_k)} + \overline{\boldsymbol{u_{bc\,H}} E_{hk}}\,)$
Dissipation (ε_{bc})	$\overline{\rho_0 \nu \dfrac{\partial (\boldsymbol{u_{bc}})_i}{\partial x_j} \dfrac{\partial (\boldsymbol{u_{bc}})_i}{\partial x_j}} + \varepsilon_p$
Turbulence production (P)	$-\,\overline{\langle u_i' u_j' \rangle_y \, \langle S_{ij} \rangle_y}$
Conversion (C_l)	$-\,\overline{\dfrac{dp_{tot}}{dz} W}$
Nonlinear Conversion (C_{nl})	$\rho_0(\,U \overline{\nabla_H.(\boldsymbol{u_{bc\,H}} u_{bc})} + V \overline{\nabla_H.(\boldsymbol{u_{bc\,H}} v_{bc})}\,)$

where overbar lines represent depth integration, subscript H denotes horizontal, E_k is the baroclinic kinetic energy density and E_{hk} is the cross-term given by

$$E_k = \frac{1}{2}\rho_0 \left({u_{bc}}^2 + {v_{bc}}^2 + {w_{bc}}^2 \right), \quad E_{hk} = \rho_0 (U u_{bc} + V v_{bc}) \, .$$

(a)

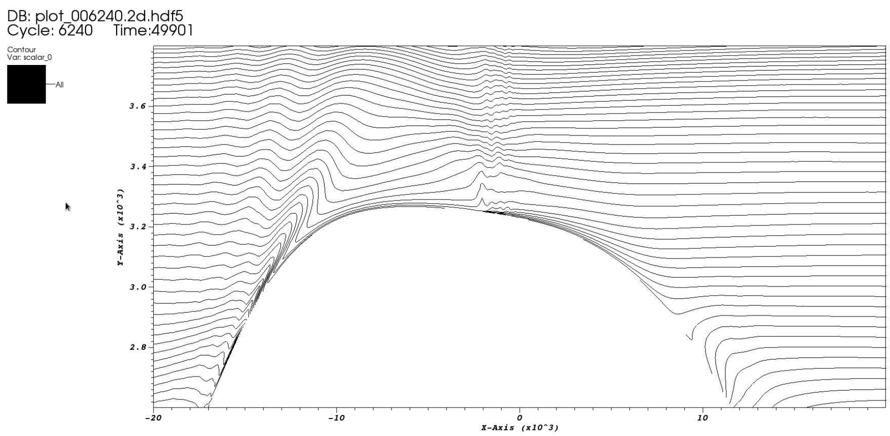

(b)

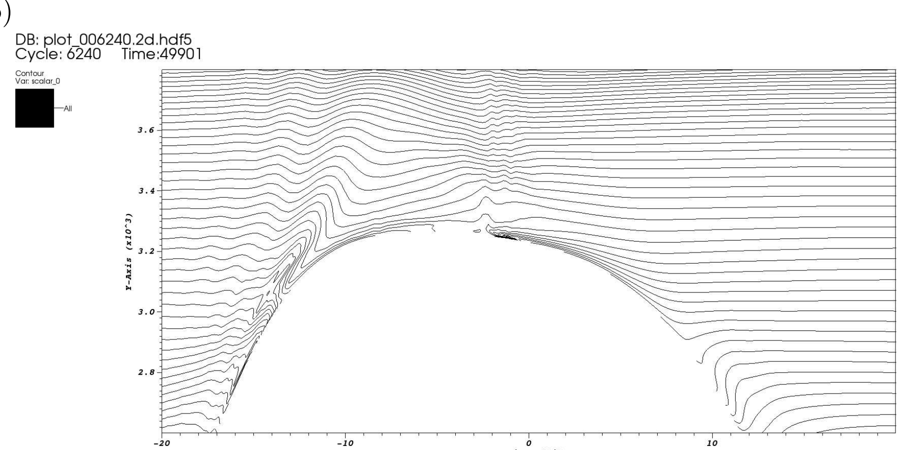

Figure 5.8: Density contours at time $t \approx 1.12T$ for (a) case 1, (b) case 2.

The rate of strain tensor, S_{ij}, is defined as $S_{ij} \equiv \frac{1}{2}(\frac{dU_i}{dx_j} + \frac{dU_j}{dx_i})$. The energy flux, $\nabla \cdot \overline{\mathbf{F}}$, in equation (5.1) is expressed as the sum of the wave flux, M, and the advective flux, M_{adv}. The conversion, $\overline{C}$ also includes the 'linear', C_l, and the nonlinear part of conversion, C_{nl}. P is the turbulence production term which represents the conversion from internal tide to turbulence locally (Rapaka *et al.*, 2013). For a nonlinear background stratification, the available potential energy (APE) and dissipation is given by (Kang, 2010; Kang & Fringer, 2012) :

$$E_P = \int_{z-\zeta}^{z} g[\rho(z) - \rho_r(z')]dz'$$
$$\varepsilon_p = g\kappa\nabla\rho^* \cdot \nabla\zeta$$

where ρ_r is the reference density $\rho_r = \rho_0 + \rho_b$, where ζ is a vertical displacement of fluid particle.

$$E_P = \frac{g^2\rho^{*2}}{2\rho_0 N^2} + \frac{g^2 d(N^2)/dz\rho^{*3}}{6\rho_0^2 N^6}$$
$$\varepsilon_p = \frac{\kappa g^2}{\rho_0 N^2}(\nabla\rho^*)^2 + \frac{g^2 d(N^2)/dz\rho^*}{\rho_0^2 N^4}\frac{\partial\rho^*}{\partial z}$$

Reorganizing the terms by putting the conversion on the left hand side and all the other terms on the right hand side:

$$C = C_l + C_{nl} = \frac{\partial}{\partial t}(E_p + E_k) + M + M_{adv} + \varepsilon_{bc} + P \tag{5.2}$$

The total energy conversion $(C_l + C_{nl})$ from the barotropic tide is balanced by
(1) internal wave flux that is radiated away (M).
(2) advective flux (M_{adv}).
(3) direct, non-turbulent viscous dissipation of the wave, ε_{bc}.
(4) energy transfer to turbulence via production (P).
(5) transient term given by $\frac{\partial}{\partial t}(E_p + E_k)$.

The fraction of energy that is dissipated at the local generation site given by $q = 1 - M/C$ is a quantity of interest among the oceanographic community. Accurate quantification of local dissipation is necessary to represent internal wave mixing in the ocean models. The quantity M is another important quantity which represents the wave energy radiated away from the generation site that is available for mixing at remote locations.

5.4 Acknowledgements

Contents of this chapter are in the process of preparation for publication in *Ocean Modeling*. V. K. Chalamalla, E. Santilli, A. Scotti & S. Sarkar (2015), SOMAR-LES, a coupled ocean-turbulence model, and its application to Kaena Ridge, (in preparation for Ocean Modeling).

Chapter 6

Summary and Future Work

In the first phase (Chalamalla *et al.*, 2013) of the thesis research, the dynamics of plane internal waves reflected from critical and subcritical slopes is examined as a function of incoming wave Froude number for different slope angles. Existing climate and ocean models do not currently include parametrizations for energy dissipated during the scattering of internal waves with sloping topographies. Motivated by the fact that the nonlinear processes during internal wave reflection are not very well understood, we identify the mechanism of transition to turbulence and quantify the phasing of subsequent turbulence. To do so, we consider an idealized problem of plane wave reflection at a linear slope with the choice of laboratory scale dimensions to enable direct numerical simulation (DNS) that resolves the smallest, viscous scales of the flow.

The wave amplitude is found to affect the functional dependence of the flow on slope angle. When the value of Fr is small, the critical case is laminar and very weak turbulence is found for a near-critical reflection with off-criticality 5°. At high Fr, there is turbulence at all the slope angles considered here. It is found that, during the initial transient when the amplitude of the density variation in the internal wave increases, regions of convective instability ($N^2 < 0$) as well as shear instability ($Ri_g < 0.25$) are formed. The mechanism of transition to turbulence in the case of critical reflection (slope angle matches with internal waves characteristic angle) is wave breaking by convective instabilities during the flow reversal from downslope to upslope, similar to the mechanism found in Gayen & Sarkar (2011a)

for boundary-intensified oscillating, baroclinic flow. One distinct peak in turbulent kinetic energy (TKE) is found every wave cycle with the turbulent buoyancy flux acting as the main contributor to the turbulence field. In the case of near but not exactly critical reflection, two distinct peaks are found every wave cycle with both shear production and turbulent buoyancy flux contributing to the TKE field. The important qualitative difference between critical and off-critical reflection is that the turbulent patch is always close to the slope during critical reflection whereas detached turbulent patches are found in the case of off-critical reflection.

The results in the various cases are collected to quantify the parametric dependence of TKE and turbulent dissipation rate (averaged over time and over distance above bottom) on slope angle and Froude number. Interestingly, it is found that reflection at near-critical angles can lead to more intense turbulence than critical slope reflection for waves with small amplitude, that is, small Fr. The reason for this low Fr behavior is that, although the velocity intensification is smaller when the slope is off-critical, the convectively unstable region, not being restrained by the boundary, can be larger and thereby lead to stronger turbulence than the exactly critical case. At higher Fr, the values of TKE and turbulent dissipation rate exhibit a monotone decrease with increasing off-criticality. If turbulent statistics, when appropriately normalized by wave characteristics, saturate with increasing Fr, parameterizations of wave dissipation for use in ocean models will be facilitated. More work is necessary to establish if the results found in the present simulations hold under more realistic oceanic conditions such as large length scales and non-uniform, rough topography.

As a followup problem, we examined the formation of subharmonics in the reflection problem. As elaborated below, this study (Chalamalla & Sarkar, 2015*b*) identifies off-critical internal wave reflection as a mechanism for nonlinear cascade of energy from internal waves to waves of smaller vertical scale through parametric subharmonic instability. Two dimensional numerical simulations of an internal wave beam with a propagation angle α (with the horizontal)incident on a slope with angle β (with the horizontal) are performed and the incoming wave amplitude, slope angle and beam width are varied. We demonstrate that a stable propagating internal wave beam with small amplitude, upon reflection, leads to a *reflected* beam that can become unstable to PSI, and provide the first quantification of this process. Supercritical, critical and subcritical reflection with reflected wave angle larger, equal, and smaller, respectively, relative to the slope angle are considered. The off-criticality values $(\alpha-\beta)$ that we considered in this study are not very large, so the velocity of the reflected wave increases and the wave length reduces in all the simulated cases leading to intensification of the reflected-wave Froude number, $Fr_r = uk_x/\Omega$. PSI of the internal wave beam is found if Fr_r is sufficiently large. In all cases exhibiting PSI, the subharmonic energy increases exponentially until it saturates to a nearly constant value.

Subharmonic growth rates in the exponential-growth stage have been computed and compared against the theory of Karimi & Akylas (2014), based on asymptotically small beam amplitude and short subharmonic instability wave, for a freely propagating internal wave beam. For a given configuration (internal wave angle 18° and beam width $1.5\lambda_x$), PSI of the reflected wave is found in the simulations when $Fr_r \geq 0.3$. For $0.3 \leq Fr_r < 0.5$, the theoretical estimates of growth rate are close to the simulation values. On the other hand, for $Fr_r > 0.5$, the subharmonic growth rates obtained from the simulation data remains more or less constant, whereas the theoretical growth rates continue to increase linearly with Fr_r. The reason is that, in the simulations with high Fr_r, energy transfer to smaller scales becomes increasingly important and viscosity effectively dissipates energy at these scales.

Beam width and internal wave angle (wave steepness) are two other parameters which are found to impact the subharmonic growth rates. A parametric study of varying the incoming internal wave angle is not performed. However, for a given internal wave angle, doubling the beam width is found to increase the growth rate by a significant factor, consistent with the theoretical predictions. Off-criticality $(\alpha - \beta)$ has a non-monotone effect on PSI. Decreasing the off-criticality to zero suppresses PSI. In the critical reflection $(\alpha = \beta)$ the reflected wave grazes the sloping bottom which restricts the formation of subharmonic modes. On the other hand, increasing the off-criticality $(\alpha - \beta)$ is found to weaken the reflected wave and thus suppress PSI of the reflected wave. In all the simulated cases which exhibit PSI, instability of the reflected wave is initiated near its generation region at the slope because the reflected wave is strongest near its origin. As the reflected wave becomes unstable near the generation region and loses energy to subharmonic modes, it becomes weaker as it travels away from the generation region. Therefore, although at a later time the reflected wave undergoes subharmonic instability away from its generation region, the instability is not as strong as it is near the reflection zone.

In the second phase (Chalamalla & Sarkar, 2015*a*), mixing and turbulent dissipation during near-bottom convective overturns driven by internal tides is investigated in an oscillatory, baroclinic boundary flow. During downslope flow, light fluid from above replaces heavier fluid resulting in the formation of an unstable density gradient detached from the viscous boundary layer. The available potential energy (APE) continues to increase until the large overturn breaks up into multiple small overturns via three-dimensional convective instability during flow reversal from down to upslope. The overturn height in this large convective overturn event (LCOE) scales with the thickness l_b of the boundary flow. In the case with a small $l_b = 6$ m that is amenable to DNS, the tallest overturn has a height of 3 m with the corresponding Thorpe length scale close to 2 m. For the case with $l_b = 60$ m computed with LES, the tallest overturn has a height of 35 m with the corresponding Thorpe scale of 20 m. There is substantial energy transfer from available potential energy (APE) to the turbulent kinetic energy (TKE) through the fluctuating buoyancy flux, shear production of turbulence is very small during the breaking of large overturn.

Thorpe scales are maximum during the initial stages of the convective instability. At a later time, when three dimensional turbulence and dissipation increases, the Ozmidov sale increases. In brief, when L_T decreases, L_O increases. The simulations show that Ozmidov, L_O, and Thorpe length scales, L_T, are different functions of the tidal phase and L_T cannot serve as a proxy for L_O during convective instability. Our result is consistent with Smyth & Moum (2000) who, in the case of shear-driven stratified turbulence, found that $R_{OT} = L_O/L_T$ varies from $\mathcal{O}(0.1)$ during the initial large-overturn stage to $\mathcal{O}(1)$ during the later stage of well-developed broadband turbulence. The present case of convectively driven turbulence shows one to two orders of magnitude increase in R_{OT} during the course of LCOE in both DNS and LES cases.

Turbulent dissipation rate estimated from Thorpe scales using individual density profiles (virtual mooring) is compared with the actual dissipation rate computed from the simulation data. It is found that Thorpe length scales overestimate the dissipation by more than an order of magnitude during the initial stages of the overturning event and underestimates the dissipation, again by more than an order of magnitude, during the later stages. It is not possible to obtain a reliable estimate of turbulent dissipation rate at a given time by measuring overturns at that time. However, their cycle-averaged values are comparable. This is manifested in the form of the *cycle-averaged* dissipation coefficient C_ϕ (usually taken to be 0.8), being $\mathcal{O}(1)$ in both DNS and LES cases. This $\mathcal{O}(1)$ value of cycle-averaged C_ϕ is explained based on available potential energy of the large convective overturns cascading to turbulence and molecular dissipation over a cycle. Thus, it may be possible to average the turbulent dissipation obtained by Thorpe analysis of an ensemble of density profiles during an *entire* wave period to approximate the cycle-averaged dissipation rate. Similarly, Thorpe analysis over the *entire* lifetime of a LCOE could give the average dissipation associated with the LCOE.

The instantaneous mixing efficiency η, during the convective mixing event has its peak value close to 0.7 in DNS and 0.6 in LES. The cycle-averaged mixing efficiency of 0.3-0.4 is also substantially larger than the commonly assumed value of 0.2. Assuming a value of 0.2 in the calculation of diffusivity could substantially underestimate the value during convective breaking events which are very common at the internal tide generation sites such as Hawaiian Ridge and Luzon Strait. High mixing efficiencies close to 0.5 have been reported (Dalziel *et al.*, 2008; Lawrie & Dalziel, 2011; Gayen & Sarkar, 2013) in situations where turbulence is driven by convective instability. A recent experimental study (Wykes & Dalziel, 2014) reported that mixing efficiency can be as high as 0.75 when the unstable density region is confined within a stable stratification from above and below. Thus, it is important that the mechanism leading to turbulence (e.g. shear instability or convective instability) needs to be established before choosing a value for η to infer mixing rates. The volume averaged diffusivity varies by two orders of magnitude between DNS and LES cases, following an inertial scaling of turbulent diffusivity: $K_\rho \propto U_b l_b$.

It is important to note that the method of overturn detection followed in this study is different from the conventional way of overturn detection methods followed by physical oceanographers. We determine overturn boundaries in the modified method by the boundaries of inversions in the density profile. The Thorpe length scale is found to be much smaller from our modified method when compared to the standard approach used by oceanographers. Thus, the conventional Thorpe scale dissipation is expected to be much higher than the Thorpe scale dissipation obtained from our modified method. The differences between the traditional approach and the modified approach (followed in this study) are being explored in another study by Masoud Jalali (Jalali *et al.*, 2015), where the Thorpe scale dissipation obtained from both conventional and modified approach are compared with the model dissipation during internal tide generation at the west ridge of Luzon Strait. Jalali *et al.* (2015) find that the modified approach shows agreement with the LES model dissipation (which we consider as benchmark dissipation) when the turbulence is from the breaking of large density overturns; on the other hand, the standard Thorpe scale approach shows better agreement with the benchmark dissipation during shear driven turbulence.

In the final phase of this study, a novel multiscale modeling technique is developed where the large scale Stratified Ocean Model with Adaptive Refinement (SOMAR) is coupled with a large eddy simulation (LES) model to accurately represent the effect of small scale turbulence on the large scale flow evolution. Both SOMAR and LES are time advanced together with LES advancing with a smaller time step. The eddy viscosity and diffusivity are passed back to SOMAR from LES at every time step of SOMAR. This technique is applied to study flow at Kaena ridge in Hawaii, a super-critical internal tide generation site. Numerical simulations are performed with SOMAR, coupled SOMAR-LES, high-resolution LES (scaled down geometry). Comparisons are made between the coupled SOMAR-LES and uncoupled SOMAR simulations, along with well resolved LES simulations. Some results are reported in this study, with a more detailed analysis of baroclinic energy budget terms to be reported in the journal publication.

Appendix A

SOMAR Algorithm

Stratified Ocean Model with Adaptive Refinement (SOMAR) is a modeling framework developed by Dr. Ed Santilli and Prof. Alberto Scotti at the University of North Carolina, Chapel Hill. This model has the flexibility to dynamically refine the grid locally to obtain more accurate solution in the regions dominated by nonlinear features. This tool is especially useful in modeling oceanic flows where the turbulence is inhomogeneous in both space and time. It also has the option of static refinement where fine spaced grid maintains its shape and location over the course of the simulation. Static refinement is useful when the active regions of the flow remains localized over a period of time.

SOMAR is mainly based mainly on Chombo AMR framework (Colella *et al.*, 2011), however some modifications has been done such as adding efficient Poisson solving techniques (Santilli & Scotti, 2011) and addition of non-stiff external forcing terms such as tidal and sponge forcing. SOMAR solves Navier Stokes equations under Boussinesq approximation in a generalized coordinate system. It uses a combination of finite difference and finite volume schemes to discretize the differential operators in the Navier Stokes equations. Second order central finite differencing is used to discretize the viscous terms and fourth order upwinding scheme is used for advective advective update. The geometric quantities (metric tensor, etc) are derived using finite volume methods so that 1) the advection update is freestream preserving and 2) the discrete Hodge-Helmholtz theorem applies (ie, the discrete solenoidal and irrotational vector fields are exactly orthogonal).

Time stepping algorithm:

1. Single-level updates: This step involves time advancement of any level from t to $t + \Delta t$ through five stages. 1.1) Obtain a first-order, time-centered estimate of the advecting velocity via the PPM method and a projection.
   1.2) Update the buoyancy from t to $t^\star$ using the PPM method for the nonlinear terms and a Crank-Nicolson update for the diffusive terms. Background stratification effects are not yet considered.
   1.3) Using the newly advected scalar information, obtain a second-order, time-centered estimate of the advecting velocity via the PPM method. We avoid a new projection by using the pressure from step 1.1.
   1.4) Update the velocity from t to $t^\star$ using the PPM method for the nonlinear terms and a Crank-Nicolson update for the viscous terms. Background stratification effects are not yet considered.
   1.5) Project the new velocity field using a modified projection scheme that also semi-implicitly adds in background stratification effects. This brings the buoyancy and velocity fields from $t^\star$ to $t + \Delta t$.

2. Synchronization: Each level gets updated using a single-level timestepping algorithm. When two or more levels arrive at the same time, they need to be "synchronized," which is a collection of many operations:
   2.1) First, the fine grid data is averaged down to the coarse level.
   2.2) Refluxing operations are performed to ensure conservation laws are enforced.
   2.3) Projection is performed on all the levels that have been altered in the process.

   Oceanic flows generally encounter high degree of anisotropy where the horizontal length scales are much bigger than the vertical scales. Solving poisson equation under such highly anisotropic conditions can significantly slow down the convergence and it can take up large fraction of the computation time. SOMAR can efficiently handle the anisotropy using a combination of leptic solver with traditional multigrid methods. More details about this technique can be found in (Santilli & Scotti, 2011). Several test cases including the lock-exchange problem, solitary wave propagation and internal tide generation have been previously considered to validate the method. Local refinement of the grid allows the solver to achieve highly accurate results with substantial reduction in computational cost (Santilli & Scotti, 2015).

References

Alford, Matthew H., Gregg, Michael C. & Merrifield, Mark A. 2006 Structure, propagation, and mixing of energetic baroclinic tides in Mamala Bay, Oahu, Hawaii. *J. Phys. Oceanogr.* **36**, 9971018.

Armenio, V. & Sarkar, S. 2002 An investigation of stably stratified turbulent channel flow using large-eddy simulation. *J. Fluid Mech.* **459**, 1–42.

Aucan, J., Merrifield, M. A., Luther, D. S. & Flament, P. 2006 Tidal mixing events on the deep flanks of Kaena Ridge, Hawaii. *J. Phys. Oceanogr.* **36**, 1202–1219.

Barry, M. E., Ivey, G. N., Winters, K. B. & Imberger, J. 2001 Measurements of diapycnal diffusivities in stratified fluids. *J. Fluid Mech.* **442**, 267–291.

Becherer, J. K. & Umlauf, L. 2011 Boundary mixing in lakes: 1. modeling the effect of shearinduced convection. *J. Geophys. Res.* **116** (C10017, doi:10.1029/2011JC007119).

Benielli, D. & Sommeria, J. 1998 Excitation and breaking of internal gravity waves by parametric instability. *J. Fluid Mech.* **374**, 117–144.

Bluteau, C. E., Jones, N. L. & Ivey, G. N. 2011 Dynamics of a tidally-forced stratified shear flow on the continental slope. *J. Geophys. Res.* **116**, C11017,doi:10.1029/2011JC007214.

Bourget, B., Dauxois, T., Joubaud, S. & Odier, P. 2013 Experimental study of parametric subharmonic instability for internal plane waves. *J. Fluid Mech.* **723**, 1–20.

Bourget, B., Scolan, H., Dauxois, T., Le Bars, M., Odier, P. & Joubaud, S. 2014 Finite-size effects in parametric subharmonic instability. *J. Fluid Mech.* **759**, 739–750.

Buijsman, M., Legg, S. & Klymak, J. M. 2012 Double-ridge internal tide interference and its effect on dissipation in Luzon Strait. *J. Phys. Oceanogr.* **42**, 1337–1356.

Cacchione, D. A., Pratson, L. F. & Ogston, A. S. 2002 The shaping of continental slopes by internal tides. *Science* **296**, 724 – 727.

Carter, G. S. & Gregg, M. C. 2006 Persistent near-diurnal internal waves observed above a site of m2 barotropic-to-baroclinic conversion. *J. Phys. Oceanogr.* **36**, 1136–1147.

Carter, G. S., Merrifield, M. A., Becker, J., Katsumata, K., Gregg, M. C., Luther, D. S., Levine, M D., Boyd, T. J. & Firing, Y. L. 2008 Energetics of M_2 barotropic to baroclinic tidal conversion at the Hawaiian Islands. *J. Phys. Oceanogr.* **38** (10), 2205–2223.

Chalamalla, V. K., Gayen, B., Scotti, A. & Sarkar, S. 2013 Turbulence during the reflection of internal gravity waves at critical and near-critical slopes. *J. Fluid Mech.* **729**, 47–68.

Chalamalla, V. K. & Sarkar, S. 2015*a* Mixing, dissipation rate, and their overturn-based estimates in a near-bottom turbulent flow driven by internal tides. *J. Phys. Oceanogr.* **45**, 1969–1987.

Chalamalla, V. K. & Sarkar, S. 2015*b* PSI in the case of internal wave beam reflection at an uniform slope. *J. Fluid Mech., (in press)* .

Clark, H. A. & Sutherland, B. R. 2010 Generation, propagation and breaking of an internal wave beam. *Phys. Fluids* **22**, 076601.

Cole, S. T., Rudnick, D. L., Hodges, B. A. & Martin, J. P. 2009 Observations of tidal internal wave beams at Kauai Channel, Hawaii. *J. Phys. Oceanogr.* **39**, 421–436.

Colella, P., Graves, D. T., Johnson, J. N., Keen, N. D., Ligocki, T. J., Martin, D. F., McCorquodale, P. W., Modiano, D., Schwartz, P. O., Sternberg, T. D. & Straalen, B. V. 2011 Chombo software package for amr applications - design document. *Lawrence Berkeley National Laboratory Report* .

Dalziel, S. B., Patterson, M. D., Caulfield, C. P. & Coomaraswamy, I. A. 2008 Mixing efficiency in high-aspect-ratio Rayleigh-Taylor experiments. *Phys. Fluids* **20**, 065106.

Dauxois, T. & Young, W. R. 1999 Near-critical reflection of internal waves. *J. Fluid Mech.* **390**, 271–295.

DeSilva, I. P. D., Imberger, J. & Ivey, G. N. 1997 Localized mixing due to a breaking internal wave ray at a sloping bed. *J. Fluid Mech.* **350**, 1–27.

Dillon, T. M. 1982 Vertical overturns: A comparison of Thorpe and Ozmidov length scales. *J. Geophys. Res.* **87**, 9601–9613.

Eriksen, Charles C. 1998 Internal wave reflection and mixing at fieberling guyot. *Journal of Geophysical Research* **103**, 2977–2994.

Gayen, B. & Sarkar, S. 2010b Turbulence during the generation of internal tide on a critical slope. *Phys. Rev. Lett.* **104**, 218502.

Gayen, B. & Sarkar, S. 2011*a* Boundary mixing by density overturns in an internal tidal beam. *Geophys. Res. Lett.* **38**, L14608.

Gayen, B. & Sarkar, S. 2011*b* Direct and large-eddy simulations of internal tide generation at a near-critical slope. *J. Fluid Mech.* **681**, 48–79.

Gayen, B. & Sarkar, S. 2011*c* Direct and large-eddy simulations of internal tide generation at a near-critical slope. *J. Fluid Mech.* **681**, 48–79.

Gayen, B. & Sarkar, S. 2011*d* Negative turbulent production during flow reversal in a stratified oscillating boundary layer on a sloping bottom. *Phys. Fluids* **23**, 101703.

Gayen, B. & Sarkar, S. 2011a Direct and large eddy simulations of internal tide generation at a near critical slope. *J. Fluid Mech.* **681**, 48–79.

Gayen, B. & Sarkar, S. 2013 Degradation of an internal wave beam by parametric subharmonic instability in an upper ocean pycnocline. *J. Geophys. Res.* **118**, 4689–4698.

Gayen, B. & Sarkar, S. 2014 Psi to turbulence during internal wave beam refraction through the upper ocean pycnocline. *Geophys. Res. Lett.* **41**, 8953–8960.

Gayen, B., Sarkar, S. & Taylor, J. R. 2010a Large eddy simulation of a stratified boundary layer under an oscillatory current. *J. Fluid Mech.* **643**, 233–266.

Gerkema, T., Staquet, C. & Bouruet-Aubertot, P. 2006 Decay of semi-diurnal internal-tide beams due to subharmonic resonance. *Geophys. Res. Lett.* **33**, L08604.

Germano, M., Piomelli, U., Moin, P. & Cabot, W. H. 1991 A dynamic subgrid-scale eddy viscosity model. *Phys. Fluids* **3(7)**, 1760–1765.

Hasselmann, K. 1967 A criterion for nonlinear wave stability. *J. Fluid Mech.* **30**, 737–739.

Ivey, G. N. & Nokes, R. I. 1989 Vertical mixing due to the breaking of critical internal waves on sloping boundaries. *J. Fluid Mech.* **204**, 479–500.

Ivey, G. N., Winters, K. B. & Koseff, J. R. 2008 Density stratification, turbulence, but how much mixing? *Annu. Rev. Fluid Mech.* **40**, 169–184.

Jalali, M., Chalamalla, V. K. & Sarkar, S. 2015 On the accuracy of overturn-based estimates of turbulent dissipation at rough topography. *J. Phys. Oceanogr.* p. submitted.

Jalali, M., Rapaka, N. R. & Sarkar, S. 2014 Tidal flow over topography: effect of excursion number on wave energetics and turbulence. *J. Fluid Mech.* **750**, 259–283.

Javam, A., Imberger, J. & Armfield, S. W. 1999 Numerical study of internal wave reflection from sloping boundaries. *J. Fluid Mech.* **396**, 183–201.

Javam, A., Imberger, J. & Armfield, S. W. 2000 Numerical study of internal wave-caustic and internal wave-shear interactions in a stratified fluid. *J. Fluid Mech.* **415**, 89–116.

Johnston, T. M. S., Rudnick, D. L., Carter, G. S., Todd, R. E. & Cole, S. T. 2010 Internal tidal beams and mixing near Monterey Bay. *J. Geophys. Res.* **116**, C03017.

Kang, D. 2010 Energetics and dynamics of internal tides in monterey bay using numerical simulations. *Ph.D. dissertation, Stanford University* p. 170.

Kang, D. & Fringer, O. 2012 Energetics of barotropic and baroclinic tides in the monterey bay area. *J. Phys. Oceanogr.* **42**, 272–290.

Karimi, H. H. & Akylas, T. R. 2014 Parametric subharmonic instability of internal waves: locally confined beams versus monochromatic wavetrains. *J. Fluid Mech.* **757**, 381–402.

Klymak, J. M., Legg, S. & Pinkel, R. 2010 A simple parameterization of turbulent tidal mixing near supercritical topography. *J. Phys. Oceanogr.* **In press**.

Klymak, J. M. & Legg, S. M. 2010 A simple mixing scheme for models that resolve breaking internal waves. *Ocean Modelling* **33**, 224–234.

Klymak, J. M., Moum, J. N., Nash, J. D., Kunze, E., Girton, J. B., Carter, G. S., Lee, C. M., Sanford, T. B. & Gregg, M. C. 2006 An estimate of tidal energy lost to turbulence at the hawaiian ridge. *J. Phys. Oceanogr.* **36**, 1148–1164.

Klymak, J. M., Pinkel, R. & Rainville, L. 2008 Direct breaking of the internal tide near topography: Kaena ridge, hawaii. *J. Phys. Oceanogr.* **38**, 380–399.

Koudella, C. R. & Staquet, C. 2006 Instability mechanisms of a two-dimensional progressive internal gravity wave. *J. Fluid Mech.* **548**, 165–196.

Kunze, E. & Toole, J. M. 1997 Tidally driven vorticity, diurnal shear and turbulence atop Fieberling Seamount. *J. Phys. Oceanogr.* **27**, 2663 – 2693.

Lawrie, A. G. W. & Dalziel, S. B. 2011 Taylor mixing in an otherwise stable stratification. *J. Fluid Mech.* **688**, 507–527.

Ledwell, J. R., Montgomery, K. L., Polzin, K. L., St. Laurent, L. C., Schmitt, R. W. & Toole, J. M. 2000 Evidence of enhanced mixing over rough topography in the abyssal ocean. *Nature* **403**, 179–182.

Legg, S. & Adcroft, A. 2003 Internal wave breaking at concave and convex continental slopes. *J. Phys. Oceanogr.* **33**, 2224–2246.

Legg, S. & Huijts, K. M. 2006 Preliminary simulations of internal waves and mixing generated by finite amplitude tidal flow over isolated topography. *Deep-sea Res. II.* **53**, 140–156.

Legg, S. & Klymak, J. 2008 Internal hydraulic jumps and overturning generated by tidal flows over a tall steep ridge. *J. Phys. Oceanogr.* **38**, 1949–1964.

Lele, S. 1992 Compact finite difference schemes with spectral like resolution. *J. Comput. Phys.* **103**, 16–42.

Levine, M. D. & Boyd, T. J. 2006 Tidally forced internal waves and overturns observed on a slope: results from home. *J. Phys. Oceanogr.* **36**, 1184–1201.

Linden, P. F. 1979 Mixing in stratified fluids. *Geophys. Astrophys. Fluid Dyn.* **13**, 3–23.

Lorke, A., Peeters, F. & Wüest, A. 2005 Shear-induced convective mixing in bottom boundary layers on slopes. *Limnol. Oceanogr.* **50**, 1612–1619.

Lorke, A., Umlauf, L. & Mohrholz, V. 2008 Stratification and mixing on sloping boundaries. *Geophys. Res. Lett.* **35** (L14610, doi:10.1029/2008GL034607).

MacKinnon, J. A., Alford, M. H., Sun, O., Pinkel, R., Zhao, Z. & Klymak, J. 2013 Parametric subharmonic instability of the internal tide at 29°N. *J. Phys. Oceanogr.* **43**, 17–28.

MacKinnon, J. A. & Winters, K. B. 2005 Subtropical catastrophe: Significant loss of low-mode tidal energy at 28.9°. *Geophys. Res. Lett.* **32**, L15605.

Martin, Joseph P. & Rudnick, Daniel L. 2006 Inferences and observations of turbulent dissipation and mixing in the upper ocean at the Hawaiian Ridge. *J. Phys. Oceanogr.* **37**, 476494.

Mater, B. D., Schaad, S. M. & Venayagamoorthy, S. K. 2013 Relevance of the Thorpe length scale in stably stratified turbulence. *Phys. Fluids* **25**, 076604.

McEwan, A. D. 1971 Degeneration of resonantly-excited standing internal gravity waves. *J. Fluid Mech.* **50(03)**, 431–448.

Moum, J. N., Caldwell, D. R., Nash, J. D. & Gunderson, G. D. 2002 Observations of boundary mixing over the continental slope. *J. Phys. Oceanogr.* **32**, 2113–2130.

Munk, W. & Wunsch, C. 1998 Abyssal recipes II: energetics of tidal and wind mixing. *Deep-Sea Research Part I-Oceanographic Research Papers* **45**, 1977–2010.

Nash, J. D., Kunze, E., Toole, J. M. & Schmitt, R. W. 2004 Internal tide reflection and turbulent mixing on the continental slope. *J. Phys. Oceanogr.* **34**, 1117–1134.

Osborn, T. R. 1980 Estimates of the local rate of vertical diffusion from dissipation measurements. *J. Phys. Oceanogr.* **10**, 83–89.

Park, Y.-G. & Bryan, K. 2000 Comparison of thermally driven circulation from a depth-coordinate model and an isopycnal-layer model. Part I:scaling-law sensitivity to vertical diffusivity. *J. Phys. Ocean.* **30**, 590–605.

Phillips, O. M. 1970 On flows induced by diffusion in a stably stratified fluid. *Deep-Sea Res.* **17**, 435–443.

Phillips, O. M. 1977 *The Dynamics of the Upper Ocean, 2nd edn.*. Cambridge University Press.

Polzin, K. L., Toole, J. M., Ledwell, J. R. & Schmitt, R. W. 1997*a* Spatial variability of turbulent mixing in the abyssal ocean. *Science* **276**, 93–96.

Polzin, K. L., Toole, J. M., Ledwell, J. R. & Schmitt, R. W. 1997*b* Spatial variability of turbulent mixing in the abyssal ocean. *Science* **276**, 93–96.

Rainville, L. & Pinkel, R. 2006 Propagation of low-mode internal waves through the ocean. *J. Phys. Oceanogr.* **36**, 1220–1236.

Rapaka, N. R., Gayen, B. & Sarkar, S. 2013 Tidal conversion and turbulence at a model ridge: direct and large eddy simulations. *J. Fluid Mech.* **715**, 181–209.

Rodenborn, B. E., Kiefer, D., Zhang, H. P. & Swinney, H. L. 2011 Harmonic generation by reflecting internal waves. *Phys. Fluids* **23**, 026601.

Rudnick, D. L., Boyd, T. J., Brainard, R. E., Carter, G. S., Egbert, G. D., Gregg, M. C., Holloway, P. E., Klymak, J. M., Kunze, E., Lee, C. M., Levine, M. D., Luther, D. S., Martin, J. P., Merrifield, M. A., Moum, J. N., Nash, J. D., , Pinkel, R., Rainville, L. & Sanford, T. B. 2003 From tides to mixing along the howaiian ridge. *Science.* **301**, 355–357.

Saenko, O. A. 2005 The effect of localized mixing on the ocean circulation and time-dependent climate change. *J. Phys. Ocean.* **36**, 140–160.

Santilli, E. & Scotti, A. 2011 An efficient method for solving elliptic equations on highly anisotropic grids. *J. Comp. Phys.* **230(23)**, 8342–8359.

Santilli, E. & Scotti, A. 2015 The stratified ocean model with adaptive refinement (somar). *J. Comp. Phys.* **291**, 60–81.

Scotti, A. 2011 Inviscid critical and near-critical reflection of internal waves in the time domain. *J. Fluid Mech.* **674**, 464–488.

Simmons, Harper L., Jayne, Steven R., Laurent, Louis C. St. & Weaver, Andrew J. 2004 Tidally driven mixing in a numerical model of the ocean general circulation. *Ocean Modelling* **6**, 245–263.

Slinn, D.N. & Riley, J.J. 1998*a* A model for the simulation of turbulent boundary layers in an incompressible stratified flow. *J. Comput. Phys.* **34**, 550–602.

Slinn, D. N. & Riley, J. J. 1998*b* Turbulent dynamics of a critically reflecting internal gravity wave. *Theoret. Comput. Fluid Dyn.* **11**, 281–303.

Smyth, W. D. & Moum, J. N. 2000 Length scales of turbulence in stably stratified mixing layers. *Phys. Fluids* **12**, 1327.

Smyth, W. D., Moum, J. N. & Caldwell, D. R. 2001 The efficiency of mixing in turbulent patches: Inferences from direct simulations and microstructure observations. *J. Phys. Oceanogr.* **31**, 19691992.

St. Laurent, L. C. & Garrett, C. 2002 The role of internal tides in mixing the deep ocean. *J. Phys. Oceanogr.* **32**, 2882–2899.

St. Laurent, L. C., Toole, J. M. & Schmitt, R. W. 2001 Buoyancy forcing by turbulence above rough topography in the abyssal Brazil Basin. *J. Phys. Oceanogr.* **31**, 3476–3495.

Sun, O. & Pinkel, R. 2013 Subharmonic energy transfer from the semidiurnal internal tide to near-diurnal motions over Kaena Ridge, Hawaii. *J. Phys. Oceanogr.* **43**, 766–789.

Tabaei, A., Akylas, T. R. & Lamb, K. 2005 Nonlinear effects in reflecting and colliding internal wave beams. *J. Fluid Mech.* **526**, 217.

Taylor, J. R. & Sarkar, S. 2008 Direct and large eddy simulations of a bottom ekman layer under an external stratification. *Int. J. Heat Fluid Flow* **29**, 721–732.

Thorpe, S. A. 1968 A method of producing a shear flow in a stratified fluid. *J. Fluid Mech.* **32**, 693–704.

Thorpe, S. A. 1977 Turbulence and mixing in a Scottish loch. *Philos. Trans. R. Soc. London Ser. A* **286**, 125–181.

Thorpe, S. A. 1987 On the reflection of a train of finite-amplitude internal waves from a uniform slope. *J. Fluid Mech.* **178**, 279–302.

Thorpe, S. A. 1992 Thermal fronts caused by internal gravity waves reflecting from a slope. *J. Phys. Oceanogr.* **22**, 105–108.

Vallis, G. K. 2000 Large-scale circulation and production of stratification: Effects of wind, geometry, and diffusion. *J. Phys. Ocean.* **30**, 933–954.

Vreman, B., geurts, B. & Kuerten, H. 1997 Large-eddy simulation of the turbulent mixing layer. *J. Fluid Mech.* **339**, 357–390.

Winters, K. B. & Barkan, R. 2013 Available potential energy density for Boussinesq fluid flow. *J. Fluid Mech.* **714**, 476–488.

Winters, K. B. & D'Asaro, E. A. 1996 Diascalar flux and the rate of fluid mixing. *J. Fluid Mech.* **317**, 179–193.

Winters, K. B., Lombard, P. N., Riley, J. J. & D'Asaro, E. A. 1995 Available potential energy and mixing in density-stratified fluids. *J. Fluid Mech.* **289**, 115–128.

W.R., Peltier & Caulfield, C.P. 2003 Mixing efficiency in stratified shear flows. *Ann. Rev. Fluid Mech.* **35**, 135–167.

Wunsch, C. 1968 On the propagation of internal waves up a slope. *Deep-Sea REs.* **25**, 251–258.

Wunsch, C. 1970 On oceanic boundary mixing. *Deep-Sea Res.* **17**, 293–301.

Wunsch, C. & Ferrari, R. 2004 Vertical mixing, energy, and the general circulation of the oceans. *Annual Review of Fluid Mechanics* **36**, 281–314.

Wykes, M. S. D. & Dalziel, S. B. 2014 Efficient mixing in stratified flows: Experimental study of a rayleigh-taylor unstable interface within an otherwise stable stratification. *J. Fluid Mech.* **756**, 1027–1057.

Zang, Y., Street, R. L. & Koseff, J. R. 1993 A dynamic mixed subgrid-scale model and its application to turbulent recirculating flows. *Phys. Fluids A* **5(12)**, 3186–3196.

Zhou, Q. & Diamessis, P. 2013 Reflection of an internal gravity wave beam off a horizontal free-slip surface. *Phys. Fluids* **25**, 036601.